Wigner systems from first principles

Miguel Escobar Azor

To cite this version:

Miguel Escobar Azor. Wigner systems from first principles. Materials Science [cond-mat.mtrl-sci]. Université Paul Sabatier - Toulouse III, 2022. English. NNT : 2022TOU30324 . tel-04187984

HAL Id: tel-04187984
https://theses.hal.science/tel-04187984

Submitted on 25 Aug 2023

Université Fédérale
Toulouse Midi-Pyrénées

THÈSE

En vue de l'obtention du

DOCTORAT DE L'UNIVERSITÉ DE TOULOUSE

Délivré par l'Université Toulouse 3 - Paul Sabatier

Présentée et soutenue par

Miguel ESCOBAR AZOR

Le 13 décembre 2022

Systèmes de Wigner à partir des premiers principes

Ecole doctorale : SDM - SCIENCES DE LA MATIERE - Toulouse

Spécialité : Physique de la Matière

Unité de recherche :
LCPQ - Laboratoire de Chimie et Physique Quantiques

Thèse dirigée par
Arjan BERGER et Stefano EVANGELISTI

Jury

Neil D. DRUMMOND	Senior lecturer	Rapporteur
Lorenzo MASCHIO	Associate professor	Rapporteur
Ivo SOUZA	Research professor	Examinateur
Arjan BERGER	Associate professor	Directeur de thèse
Stefano EVANGELISTI	Full professor	Co-directeur de thèse
Mai DINH	Full professor	Présidente

Acknowledgments

I would like to express my heartfelt gratitude to my family, especially my mother, father, and sister, for their unconditional love and support throughout my academic journey. Their unwavering belief in me has been my greatest source of strength. I am also grateful to Patricia, who has been a friend like family and has always been there for me with her kindness and encouragement.

I am deeply thankful to Arjan an Stefano, whose guidance, expertise, and mentorship have been instrumental in shaping my research. Their insights and constructive criticism have greatly influenced my work, and I am grateful for the opportunities they provided me to grow as a researcher.

I would also like to extend my sincere thanks to my colleagues, who have provided me with a supportive and collaborative work environment. I have learned a lot from them, both professionally and personally.

Finally, I would like to acknowledge the IT and administration teams for their technical support and for ensuring the smooth running of the Lab. Their hard work and dedication have made my research experience a lot easier.

Thank you all for being part of my journey. This thesis would not have been possible without your support and contributions.

Contents

List of Figures

List of Tables

Chapter 1

General introduction

Almost a century ago, Wigner predicted that a system solely consisting of interacting electrons in a neutralizing uniform background would form a crystalline structure at sufficiently low density with the electrons localized at lattice sites [1]. His argument can be understood by considering the dependence of the kinetic and repulsive energies on the Wigner-Seitz radius r_s, which is the radius of a sphere containing, on average, one electron. Or more generally, half the average distance between nearest-neighbor electrons. While the kinetic energy scales as r_s^{-2} the repulsive energy scales as r_s^{-1}. Consequently, in the low-density limit (large r_s), the Hamiltonian is dominated by the repulsive energy leading the electrons to localize in space. When many electrons are present, the electrons will localize at crystallographic sites forming a so-called Wigner crystal. Both one and two-dimensional Wigner crystals have been observed experimentally [2, 3]. Generally speaking, one speaks of Wigner localization whenever electrons localize due to the electron-electron repulsion. For few-electron systems one also speaks of Wigner molecules [4, 5, 6, 7, 8, 9, 10] which have also been observed experimentally [11].

It is important to be able to describe Wigner localization within *ab initio* theory to analyze and perhaps even predict their properties. However, in these low-density regions, the electron correlation is strong, which is a problem for many condensed-matter theories. [12, 13] For example, Kohn-Sham density functional theory (KS-DFT) [14, 15] using currently available functionals fails to describe strong correlation satisfactorily. As an alternative to KS-DFT, the strictly correlated electrons (SCE) DFT has been proposed to deal with the strongly correlated limit. [16, 17] The SCE-DFT can be combined with KS-DFT, and Wigner localization has been observed with this approach [18, 19, 20].

The goal of this thesis is the description of Wigner localization from first-principles calculations. In order to achieve this goal, the first thing we have to do is to confine the electrons within a region in space. There are several ways of doing this: we could confine the electrons to a finite d-dimensional system with a positive background, but border effects would influence the results [9]. One way of avoiding border effects is to confine the electrons to a d-dimensional closed space such as a d-torus. This is what we will do in one dimension by confining 2 electrons to a 1-torus which is equivalent to a ring. However, for $d > 1$, the numerical implementation of the geometry of a d-torus is cumbersome. Therefore, we apply periodic boundary conditions (PBC). More precisely, we define a regular d-dimensional supercell and then modify its topology into a toroidal topology by joining opposite sides of the cell without deformation [21]. This procedure yields a supercell with the topology of a d-Clifford torus. A d-Clifford torus is a flat, closed d-dimensional real Euclidean space embedded in a complex d-dimensional Euclidean space. For example, in this framework, a circle and a line are topologically equivalent.

Since strong electron correlation drives the Wigner localization, the *ab initio* study of this phenomenon requires accurate quantum-chemistry approaches such as full configuration interaction (FCI) or multiconfigurational methods such as complete active space self-consistent field in order to obtain highly accurate energies and wave functions in both the low-correlation and the high-correlation regimes [22, 23, 24, 25]. In chapters 4 and 5 we will use exact diagonalization of the Hamiltonian to obtain numerically exact results because we limit ourselves to 2-electron Wigner molecules.

Finally, in chapter 6, we can no longer use exact diagonalization to solve the numerical problem in the case of many electrons. Therefore high spin restricted open-shell Hartree–Fock methods to study the N-electron Wigner fragments.

The manuscript is organized as follows. In chapters 2 and 3 we give the theoretical details of our approach. In particular, we will describe the periodic boundary conditions and the basis set. In chapters 4-6, we will present the numerical studies we carried out, give more details of the employed methodology and discuss the obtained results. Finally, in chapter 7, we draw the conclusions from our work. Throughout this manuscript we use Hartree atomic units $\hbar = e = m_e = a_0 = 1$.

Chapter 2

Clifford Periodic Boundary Conditions

Contents

In this chapter, we will introduce periodic boundary conditions to simulate Coulombic systems and describe the Clifford boundary conditions, the boundary conditions we will work with in the present manuscript.

2.1 Periodic Boundary Conditions

Condensed systems, such as solids (ordered or amorphous) or liquids, as well as lower-dimensional systems, such as surfaces or wires, are macroscopic objects made up of numerous atoms which can be modeled by infinite systems. Furthermore, several physical quantities of the bulk are unaffected by the presence of a boundary. In other words, they are unaffected by truncation of the sample [26].

Although periodic systems are idealizations of real systems (the periodicity is broken at the boundaries or by defects), the system's periodicity is a crucial tool for modeling real systems. We can describe an ordered system in which the location of, say, atoms in a crystalline solid is repeated in space on a regular basis. This is accomplished by identifying the smallest component of a system that exhibits a repeating pattern and then, replicate it in all direction of the space. This particular unit is known as a primitive unit cell. A single atom, a collection of atoms, ions, or molecules, are only a few examples of elements that can make up a primitive cell. These elements are known as a basis. The set of translations that forms the full periodic crystal by repeating the basis is known as the Bravais lattice, which is a lattice of points in space. A property inherent to all periodic systems is connected to the translations of the elements of the primitive cell. Any translation can be expressed as an integer times a lattice vector, e.g. , in 3D we have

$$\mathbf{T}(\mathbf{n}) = \mathbf{T}(n_1, n_2, n_3) = n_1\mathbf{a}_1 + n_2\mathbf{a}_2 + n_3\mathbf{a}_3, \tag{2.1}$$

where n_1, n_2, n_3 are integers, $\mathbf{a}_i$, $i = 1, 2, 3$ are the primitive translation vectors, which span the lattice. In one dimension, the translations $T(n) = na$ are simply multiples of the a, which is the length of the unit cell where n can be any integer. For two and three dimensions, there are several choices of the unit cell, as shown in table 2.1. For convenience, we will only discuss regular geometries where all interior angles are equal and right (90°) and all sides have the same lengths. To introduce periodic boundary conditions, let us imagine a system represented on the right side of Fig. 2.1. We can identify its primitive cell (left side of Fig. 2.1) as a square unit cell with dimension $L_x = L_y = L$ made up of 4 different particles (basis), a circle, a rectangle, a cross, and a star. Knowing the initial positions of the basis we can define the

Table 2.1: Lattice vectors for some 2- and 3-dimensional cells where a, b and c are the primitive lattice vectors.

	2-dimensional lattices			3-dimensional lattices			
	Square	Rectangular	Triangular	Cubic	hcp	fcc	bcc
$\mathbf{a}_1$	(1,0)	(1,0)	(1,0)	(1,0,0)	(1,0,0)	$(0,\frac{1}{2},\frac{1}{2})$	$(-\frac{1}{2},\frac{1}{2},\frac{1}{2})$
$\mathbf{a}_2$	(0,1)	(0,b/a)	$(\frac{1}{2},\frac{\sqrt{3}}{2})$	(0,1,0)	$(\frac{1}{2},\frac{\sqrt{3}}{2},0)$	$(\frac{1}{2},0,\frac{1}{2})$	$(\frac{1}{2},-\frac{1}{2},\frac{1}{2})$
$\mathbf{a}_3$	-	-	-	(0,0,1)	$(0,0,\frac{c}{a})$	$(\frac{1}{2},\frac{1}{2},0)$	$(\frac{1}{2},\frac{1}{2},-\frac{1}{2})$

position of those elements in the whole system. For instance, in figure 2.1 the position of $\mathbf{R}_{i'}$ and $\mathbf{R}_{i''}$ will be given by

$$\mathbf{R}_{i'} = \mathbf{R}_i + \mathbf{n}(1,0) = \mathbf{R}_i + 1L_x + 0L_y \tag{2.2}$$

$$\mathbf{R}_{i''} = \mathbf{R}_i + \mathbf{n}(-1,-1) = \mathbf{R}_i - 1L_x - 1L_y. \tag{2.3}$$

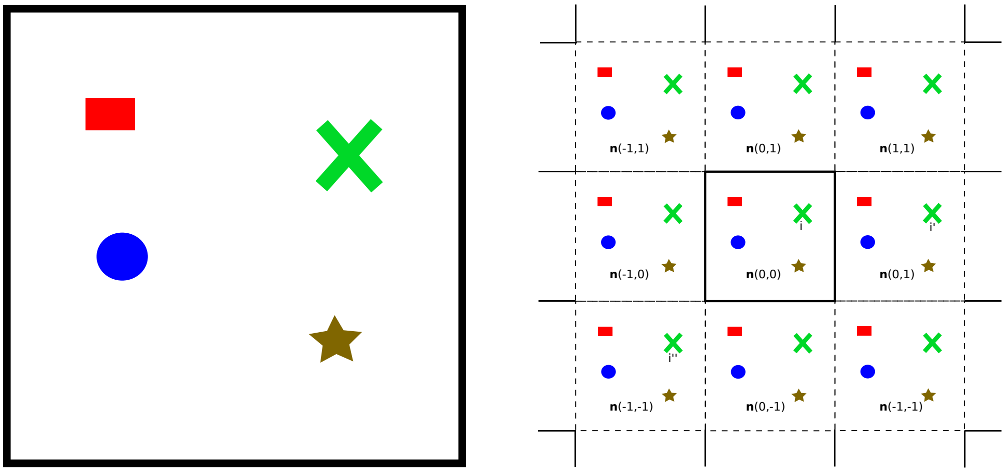

Figure 2.1: Left: Representation of a primitive cell. Right: Representation of a small supercell where the primitive cell is placed at the center.

If the particles interact, we can create a supercell containing multiple primitive cells. The full interacting system can then be modeled by imposing periodic boundary conditions on the supercell. The central supercell is thus surrounded by copies called images or replicas. We note that this introduces an artificial translational symmetry in the system. In practical calculations, the size of the supercell is limited to a few primitive cells, thus introducing the so-called finite-size errors.

2.2 Clifford Boundary Conditions

When studying systems driven by Coulomb interactions, such as Wigner systems, correlated methods are required to describe the wave function accurately. Quantum chemistry methods, more precisely post-HF methods, add electron correlation on top of the uncorrelated Hartree-Fock (HF) solution [27, 28]. To describe Wigner localization using the available post-HF methods, we have formulated boundary conditions where the Coulomb potential is treated explicitly, avoiding the use of replica images.

For many interacting electrons, we need to solve the Schrödinger equation over the entire supercell. Generally speaking, we can write the many-body Hamiltonian as

$$\hat{H} = -\frac{1}{2}\sum_{i=1}^{N}\nabla_i^2 + \sum_{i}^{N}\sum_{j<i}^{N}\frac{1}{|\mathbf{r}_i - \mathbf{r}_i|} \tag{2.4}$$

where N is the number of electrons in the simulation cell.

In this thesis, we will work with connected (closed) flat Euclidean spaces, as shown in Fig 2.2. In order to do so, we will create a regular (all angles are right and lengths of the sides are equal) d-dimensional Euclidean supercell and then modify its topology into a toroidal topology by identifying opposite extremes, sides, or faces depending on the dimensionality of the system. Then, we will "glue" them together without the deformation (bending) of the cell. Therefore, all the angles and lengths are conserved [21]. As a result of the connection process, we have what is known as a Clifford torus (CT) or flat torus. A CT is a flat, finite and borderless d-dimensional space embedded into a $2d$-dimensional Euclidean as shown in the right side of Fig. 2.2 for a $2-$CT. A d-CT has zero Gaussian curvature everywhere meaning that the Laplacian in the kinetic energy operator is the usual one given by $\nabla^2 = \sum_{i=1}^{d} \partial_i^2$. We refer to Ref. [29] for more details on the mathematics of Clifford tori.

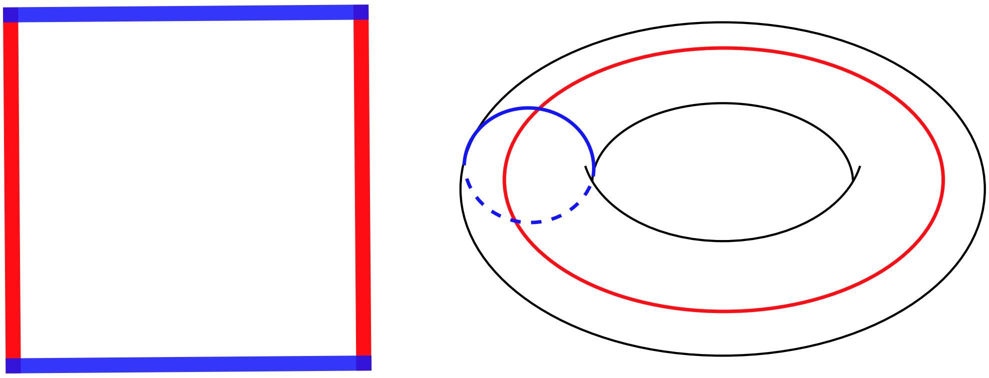

Figure 2.2: Clifford boundary conditions in E^2. Left: Square with the pairing of the facing edges. Right: 2-Torus obtained by gluing opposite edges of the square. The embedded graph (red and blue circles) corresponds to the paired edges of the square.

Due to the nature of the Clifford supercell (CSC), we can define the distance between two points in different ways. From the geometrical point of view, we can define a distance following the first axiom of Euclidean plane geometry "For any two different points, there exists a line containing these two points[30]." This is the geodesic distance defined as the shortest path between two points on the surface of the torus (See Fig. 2.3). The geodesic distance, r_{12}^{geo} can be written as

$$r_{12}^{geo} = \sqrt{\sum_{i=1}^{d} r_{12}^2(i)}, \tag{2.5}$$

where i sums over the number of d dimensions. The definition of $r_{12}(i)$ is taken as

$$r_{12}(i) = \begin{cases} |r_1(i) - r_2(i)| & \text{if } |r_1(i) - r_2(i)| < \frac{L}{2} \\ \\ L - |r_1(i) - r_2(i)| & \text{if } |r_1(i) - r_2(i)| > \frac{L}{2} \end{cases} , \qquad (2.6)$$

or, equivalently, $\min\big(|r_1(i) - r_2(i)|, L - |r_1(i) - r_2(i)|\big)$. In Fig. 2.4, we can observe the evolution of the geodesic distance and the corresponding Coulomb potential between a point fixed at 0 and a second point moving along a periodic line of length L. We observe that, r_{12}^{geo} presents a discontinuity in its derivative when $r_{12}(i) = \frac{L}{2}$ which implies that the Coulomb potential is also discontinuous at that point. Thus, the forces, which are related to the gradient of the Coulomb potential, are also discontinuous at that point. Before, we mentioned the first axiom of Euclidean plane geometry. Hilbert redefined this statement: "For any two different points, there exists a line containing these two points, and this line is unique [31]." At the points where $r_{12}(i) = |r_1(i) - r_2(i)| = L - |r_1(i) - r_2(i)| = \frac{L}{2}$, r_{12}^{geo} is not uniquely defined.

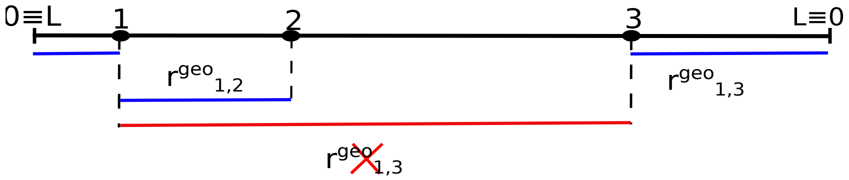

Figure 2.3: Schematic representation of r_{12}^{geo} computed as the shortest path between two points on the surface of a 1-dimensional Clifford torus.

The second distance is related to the topology of the d-Clifford torus. A d-CT is topologically equivalent to a d-torus. Thus we can define a second distance, r_{12}^{euc}, as the length of the shortest possible path between two points in the embedding space of the Clifford torus. As an example, r_{12}^{euc} is represented

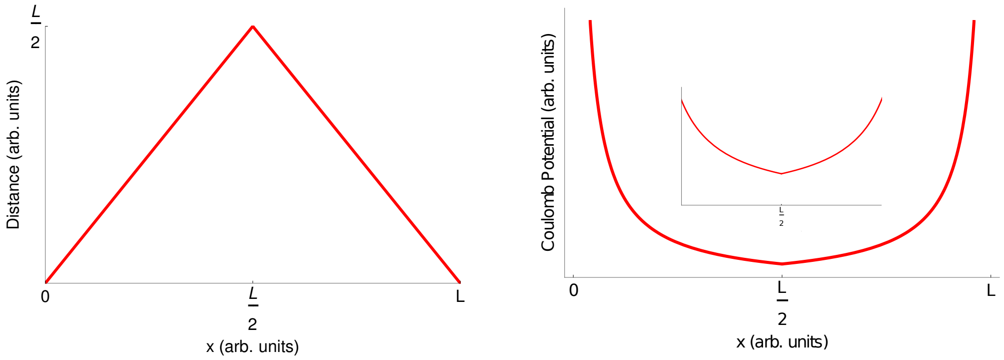

Figure 2.4: Left: The geodesic distances between two points on a 1-CT of length L where one of them is fixed at $x = 0$. Right: Coulomb potential between two charges on a 1-CT of length L where one charge is fixed at $x = 0$computed by the geodesic. Inset: zoom around $\frac{L}{2}$

as a red line in Fig. 2.5 for a 1-CT of length L. We will call θ to the angle between two segments of length $R = \frac{L}{2\pi}$ where R is the radius. Each segment connects the circle's center with its respective position on the circle (1 and 2 in Fig. 2.5). An expression for r_{12}^{euc} can be obtained from trigonometric identities as since

$$\sin\left(\frac{\theta}{2}\right) = \frac{\frac{r_{12}^{euc}}{2}}{R} \tag{2.7}$$

and $\theta = \frac{2\pi r_{12}}{L}$, where r_{12} has been introduced in Eq. (2.6), we obtain.

$$r_{12}^{euc} = \frac{L}{\pi}\sin\left(r_{12}\frac{\pi}{L}\right). \tag{2.8}$$

For higher dimensions, we can proceed similarly. We compute r_{12}^{euc} in each dimension, and then, by Pythagoras' theorem, we obtain the desired quantity (see Fig. 2.6 for an example in 2D). The general expression for r_{12}^{euc} in a regular a $d-$dimensional system where all the angles are right angles is

$$r_{12}^{euc} = \frac{L}{\pi}\sqrt{\sum_{i=1}^{d}\sin^2\left(r_{12}(i)\frac{\pi}{L}\right)}, \tag{2.9}$$

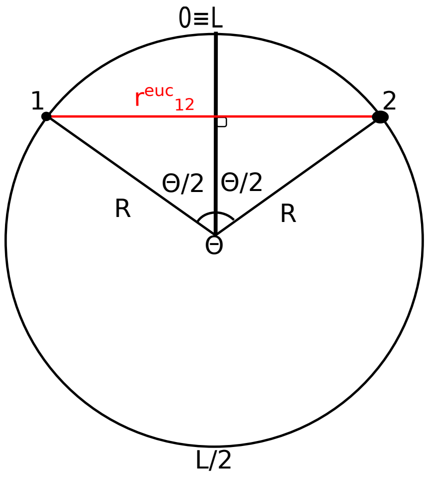

Figure 2.5: Ring obtained by gluing together the edges of the 1-dimensional Clifford supercell. Graphical derivation of the Euclidean distance in a 1−dimensional Clifford torus

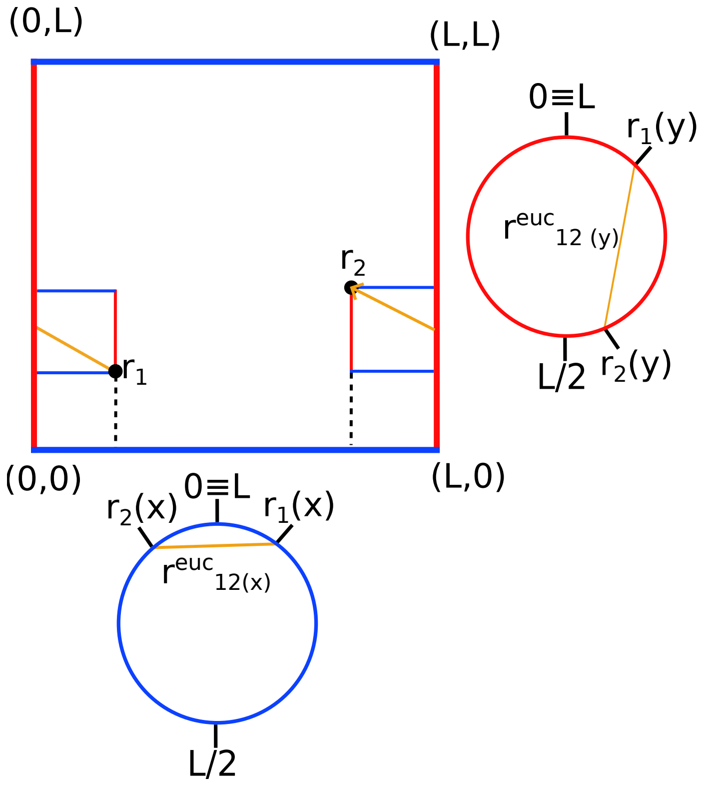

Figure 2.6: Euclidean distance in a 2-Clifford torus. A 2-CT can be seen as the Cartesian product of two circles, one in each dimension.

where $r_{12}(i)$ is defined in Eq. (2.6).

In Fig. 2.7, we can observe the evolution of the euclidean distance between a point fixed at 0 and a second point moving along a periodic line of length L. We observe that r_{12}^{euc} is a continuously differentiable, smooth, and uniquely defined function, making it suitable for describing long-range Coulomb interactions.

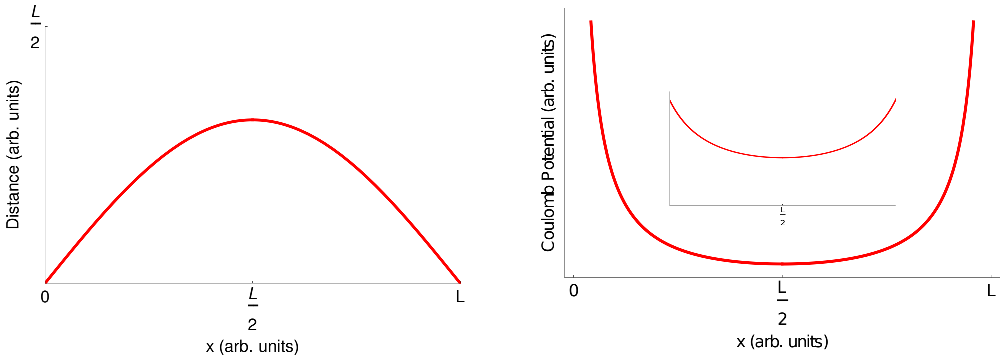

Figure 2.7: Left: The euclidean distances between two points on 1-CT of length L where one of them is fixed at $x = 0$. Right: Coulomb potential between two charges on 1-CT of length L where one charge is fixed at $x = 0$ computed by the euclidean distance.

CHAPTER 3

Basis set.

Contents

This chapter is dedicated to describing the basis set we will use, and it will be divided into the following parts. First, the most commonly used basis sets for quantum chemical calculations, Slater-type orbitals and Gaussian-type orbitals will be introduced. We will then focus on the Gaussian basis set, the most widely used basis in the quantum chemistry community. Second, we will describe the distributed Gaussian basis set and explain its advantage for our calculations. The main difference between the usual Gaussian basis set and the distributed Gaussian is the position of their centers. In the former basis, the Gaussians are centered at atomic positions, while in the latter basis, the centers of the corresponding Gaussian functions are evenly distributed in the system. Then, we will construct a symmetry-adapted basis as a Bloch sum of the distributed Gaussian functions. We will finish this chapter by introducing a newly developed basis function, the toroidal Gaussians orbital.

3.1 Most used basis sets in quantum chemistry.

A molecular orbital is usually expressed as a linear combination of atomic orbitals (AO). These latter functions are, in turn, expanded in a finite set of basis functions [32]. In theory, one could use whatever basis functions depending on the nature of the system in question. Moreover, the accuracy of the numerical eigensolutions can be improved, in principle, by increasing the size of the basis set.

The development of novel bases has been, and is still, an active field in quantum chemistry [33, 34, 35]. The most widespread basis functions for quantum-chemical calculations are the Slater-type and Gaussian-type functions [36, 37]. On the other hand, plane waves and Wannier functions are the predilections of the solid-state community [38].

3.1.1 Slater-Type Functions

The first kind of orbitals we will present are the Slater-type orbitals (STOs), named after the physicist John C. Slater, who introduced them in 1930 [36].

The Slater-type functions, $\chi_{l,m}^{STO}(r,\theta,\varphi;\zeta)$, consist of the product of a radial part $R_l^{STO}(r;\zeta)$, and an angular part, $Y_{lm}(\theta,\varphi)$, that is the real form of spherical harmonics. Here n, l and m are the well-known principal, azimuthal, and magnetic quantum numbers. The radial part is written as

$$R_l^{STO}(r;\zeta) = N r^l e^{-\zeta r} \tag{3.1}$$

where N is the normalization constant, r is the distance between the electron and the center of the STO, and ζ is the orbital exponent that tunes the width of the basis function. The STO possesses an exponential decay at long-range, which describes the exact behaviour of the wave function for 1-electron systems; in addition, it reaches a maximum at $r = 0$, where its derivative is discontinuous, describing the behavior of the exact wave function at the center of the STO (nuclear cusp). A pictorial representation of the radial part described in Eq. (3.1) is given in figure 3.1.

The difficulty of using STOs as a basis arises from the tedious computation of two-electron (Coulomb) integrals which cannot be integrated analytically. Efforts in solving this problem can be found in Refs. [39] and [40]. Slater-type orbitals are used as a basis in the ADF (Amsterdam Density Functional) package [41].

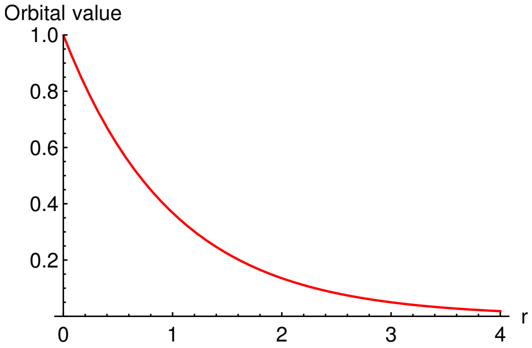

Figure 3.1: The radial 1-s STO with exponent $\xi = 1$: $R_0^{STO}(r;1)$.

3.1.2 Gaussian-type Orbitals.

Gaussian-type orbitals (GTOs) are the most widely used and developed in quantum chemistry. Following the same notation as before, a GTO can be defined as follows

$$\chi_{l,m}^{GTO}(r,\theta,\varphi;\zeta) = R_l^{GTO}(r;\zeta)Y_{lm}(\theta,\varphi) = Nr^l e^{-\zeta r^2} Y_{lm}(\theta,\varphi), \tag{3.2}$$

or, in their Cartesian definition

$$\chi_{l,m}^{GTO}(x,y,z;\zeta) = Nx^i y^j z^k e^{-\zeta r^2} \mid i+j+k=l, \tag{3.3}$$

where z, y, and x are the Cartesian components.

Eqs. 3.2 and 3.3 are equivalent representations for s-type and p-type orbitals. Differences start to show up when considering higher angular momenta. In this case, for a particular azimuthal quantum number l, one obtains more Cartesian functions than spherical ones, as presented in table 3.1.2. In addition, one can construct the complete set of spherical Gaussian functions using a linear combination of the Cartesian ones [42]. Although the use of spherical Gaussian functions seems to be more compact, it can be shown that the use of Cartesian ones facilitates the evaluation of two-electron integrals [27].

Orbital	l	Spherical	Gaussian
s	0	1	1
p	1	3	3
d	2	5	6
f	3	7	10
$\vdots$	$\vdots$	$\vdots$	$\vdots$

Table 3.1: Number of spherical and Cartesian Gaussian functions for the first four values of l.

Unlike a Slater-Type function, a single Gaussian-type function cannot describe the short and long-range behavior of the wave function. A GTO's derivative is zero at the atomic center, meaning it cannot describe the nuclear cusp. In addition, these functions decay faster than the Slater ones, meaning that they do not properly describe the long-range behavior of the wave function. These two important points are depicted in Fig. 3.2.

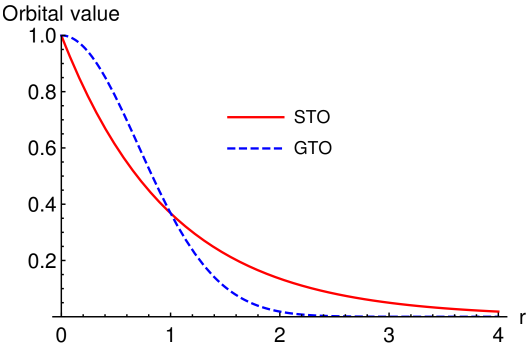

Figure 3.2: Illustrating the difference between the radial distribution of 1-s STO and 1-s GTO functions.

To overcome this problem, which emerges from the different descriptions of the radial part, we can approximate an STO by a linear combination of GTOs

$$R_l^{STO}(r,\zeta) \approx \sum_i^m \omega_i R_l^{GTO}(r,\zeta_i) = \sum_i^m \omega_i r^l e^{-\zeta_i r^2}, \tag{3.4}$$

where i sums over the m Gaussians needed to describe the STO in question, ζ_i are the exponents of Gaussians, and ω_i are the associated weights. As an example, we approximate a 1s Slater-type radial function (with $\zeta = 1$) by three even-tempered Gaussian-type functions with $\boldsymbol{\zeta} = \{10, 1, 0.1\}$. The weights ω_i are then found to be

$$\boldsymbol{\omega} = \{0.2145, 0.5437, 0.1746\}\,. \tag{3.5}$$

In Fig. 3.3, we plot the original STO with its associated approximated function. Although a large number of GTOs is needed to describe a single STO

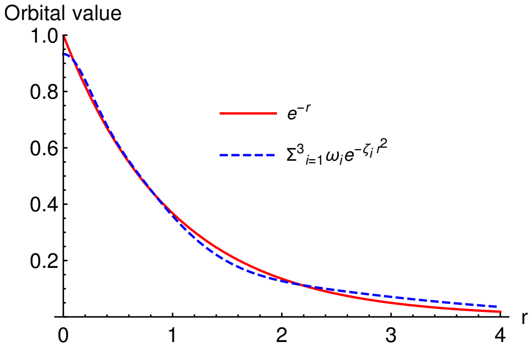

Figure 3.3: Approximating a 1s Slater-type orbital as a linear combination of three Gaussians.

properly, GTOs are the preferred basis functions because of practical numerical reasons. This practicality arises from the Gaussian product rule, which states that the product of two Gaussians is another Gaussian centered somewhere between the two primitive Gaussians [37].

As an illustration, we will focus on the particular case of the product of two 1-s Gaussian orbitals. From now on, we will denote a 1-s Gaussian orbital as g ($\chi^{GTO}_{0,0} = g$). A normalized 1-s Gaussian centered at $\mathbf{R}_\mu$ can be written as

$$g_\mu(\mathbf{r};\alpha) = \left(\frac{2\alpha}{\pi}\right)^{\frac{3}{4}} e^{-\alpha|\mathbf{r}-\mathbf{R}_\mu|^2}, \tag{3.6}$$

where the prefactor is the normalization constant and α is the gaussian exponent. Generally speaking, the product of two GTOs, g_μ and g_ν, with exponents α and β, respectively, will produce a new Gaussian, g_ω centered at some point,

$\mathbf{R}_\omega$, on a line connecting the centers of the two Gaussians

$$\begin{aligned} g_\mu(\mathbf{r};\alpha)g_\nu(\mathbf{r};\beta) =& \left(\frac{2\alpha}{\pi}\right)^{\frac{3}{4}} e^{-\alpha|\mathbf{r}-\mathbf{R}_\mu|^2} \left(\frac{2\beta}{\pi}\right)^{\frac{3}{4}} e^{-\beta|\mathbf{r}-\mathbf{R}_\nu|^2} \\ \equiv& g_\omega(\mathbf{r};\gamma) = K e^{-\gamma|\mathbf{r}-\mathbf{R}_\omega|^2} \end{aligned} \tag{3.7}$$

where

$$\mathbf{R}_\omega = \frac{\alpha\mathbf{R}_\mu + \beta\mathbf{R}_\nu}{\alpha+\beta} \tag{3.8}$$

$$\gamma = \alpha + \beta \tag{3.9}$$

$$K = \left(\frac{2}{\pi}\right)^2 (\alpha\beta)^{\frac{3}{4}} e^{-\frac{\alpha\beta}{\alpha+\beta}(\mathbf{R}_\mu-\mathbf{R}_\nu)^2} \tag{3.10}$$

An excellent review of the development of Gaussian basis sets for molecular calculations can be found in Ref. [43].

3.2 Distributed Gaussian Orbitals

Usually, in quantum chemistry, Gaussian orbitals are centered on atomic positions. However, when describing the deformation of the electron density, the basis set requires augmentation with polarization function, which increases the computational cost considerably. For instance, the computation of long-range properties such as polarizabilities and non-covalent interactions can only be accounted for with polarization functions [44, 45]. However, the use of diffuse functions can yield linear dependencies [46, 47]. The depiction of long-range interactions may be accounted for by using a smaller basis on nuclei and adding additional basis functions at the center of chemical bonds; this technique can result in a quicker convergence to the basis set limit [48]. Another strategy has been proposed to eliminate linear dependencies from diffuse functions in a molecular system. In this method, diffuse functions are represented by a large number of non-diffuse functions distributed across the system [49, 50]. Using such lattices of Gaussian functions is an ancient concept, first presented by Haines and coworkers as the "Gaussian cell model [51]." Wilson and collaborators further explored the Gaussian cell model, they demonstrated that the lattice basis set may be significantly improved by adding AO functions to the nuclei [52, 53, 54].

Due to the nature of the system we want to describe, a homogeneous d-dimensional system consisting solely of electrons confined to a d-dimensional Clifford torus, we want a basis set that can accurately describe the wave function in the whole Clifford supercell. Moreover, since we want to describe the low-density regime whose electrons localize, we need a localized basis. In adition, the basis should allow a simple evaluation of Hamiltonian and overlap matrices while providing accurate results for a given basis set parameter (number of basis functions and orbital exponent).

A basis set that fulfills all the previous requirements is the distributed Gaussians basis set. Therefore, the basis set consists of identical $1s$ Gaussian functions with the same orbital exponent, α. The number of basis functions is equal to $M = m^d$ where m is the number of functions placed on each edge of the Clifford supercell, and d is the system's dimensionality. The M GTOs will be evenly distributed along the Clifford supercell with a constant distance δ between two neighboring centers. A graphical representation of the basis set for a 2-dimensional CSC can be found in Fig. 3.4.

The overlap between two neighboring normalized Gaussians, g_μ and g_ν, on

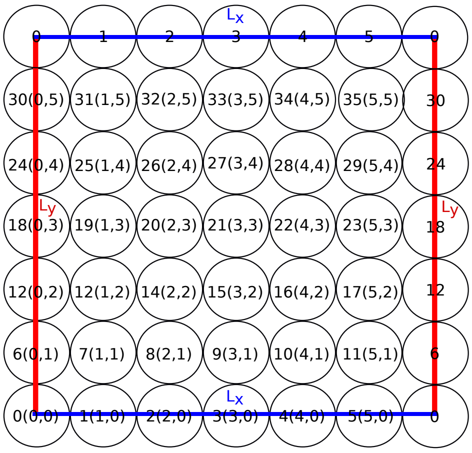

Figure 3.4: Graphical representation of the basis consisting of 36 distributed Gaussian functions in a 2-dimensional regular grid.

the CSC having the same α exponent is given by

$$S_{\mu\nu}(\alpha, r^{geo}_{\mu\nu}) = \langle g_\mu | g_\nu \rangle = e^{\frac{-\alpha r^{geo\,2}_{\mu\nu}}{2}}, \tag{3.11}$$

Where $r^{geo}_{\mu\nu}$ was defined in the Chapter 2 Eq. (2.5). We note that the Gaussian product rule only holds for $r^{geo}_{\mu\nu}$, and not for $r^{euc}_{\mu\nu}$

Equation 3.11 depends only on the product $\alpha(r^{geo}_{\mu,\nu})^2$, which can be simplified by taking into account the fact that our basis functions are evenly distributed. As a consequence, we can define (in one dimension) $r^{geo}_{\mu\nu} = min(|\mu-\nu|, m-|\mu-\nu|)\delta = k\delta$ with μ, ν integers and $k = \mu - \nu$. Thus, we can define a new parameter $\xi = \alpha\delta^2$ and rewrite the overlap as

$$S_k(\xi) = e^{\frac{-\xi k^2}{2}}. \tag{3.12}$$

As it can be seen in Eq. (3.12) the overlap does not depend on α and $r^{geo}_{\mu,\nu}$ anymore but on k and ξ. The introduction of the parameter ξ presents a big advantage since, as far as ξ and M are constant, α will be scaled in such a way that the overlap matrix for different system sizes remains the same. This holds for two and three dimensions.

The derivation of the kinetic and Coulombic integrals can be found in many textbooks [55]. Therefore, we will focus on what is of interest to the present thesis. As we have seen in the previous chapter, we have two different definitions of the distance, $r_{\mu\nu}^{geo}$ and $r_{\mu\nu}^{euc}$. As discussed before, we have to use $r_{\mu\nu}^{geo}$ when dealing with Gaussian products. On the other hand, we have $r_{\mu\nu}^{euc}$, which is suitable to treat Coulombic interactions since it is a smooth and continuously differentiable function.

Taking into account the last two statements, we can write the one- and two-electron integrals within the CSC as

$$T_{\mu,\nu} = \langle g_\mu | -\frac{1}{2}\nabla^2 | g_\nu \rangle = \frac{\alpha}{2}\left(3 - \alpha\ |r_{\mu,\nu}^{geo}|^2\right) e^{-\frac{\alpha}{2}|r_{\mu,\nu}^{geo}|^2} \tag{3.13}$$

$$\langle \mu, \nu | \rho, \sigma \rangle = 2\sqrt{\frac{\alpha}{\pi}} e^{-\frac{\alpha}{2}\left((|r_{\mu,\rho}^{geo}|^2 + (|r_{\nu,\sigma}^{geo}|^2\right)} F_0[\alpha |r_{P,Q}^{euc}|^2], \tag{3.14}$$

where

$$F_0[\alpha|r_{P,Q}^{euc}|^2] = \begin{cases} 1 & \text{if } \alpha|\bar{d}_{P,Q}|^2 \leq 10^{-8} \\ \frac{1}{2}\sqrt{\frac{\pi}{\alpha|\bar{d}_{P,Q}|^2}} erf\left(\sqrt{\alpha|r_{P,Q}^{euc}|^2}\right) & \text{if } \alpha|\bar{r}_{P,Q}^{euc}|^2 > 10^{-8} \end{cases} \tag{3.15}$$

and P and Q are the barycenter points of Gaussians g_μ and g_ρ, and g_ν andg_σ, respectively. In a similar way to the overlap, introducing the ξ parameter presents a big numerical advantage. Once again, if M and ξ remain constant, we can compute the integrals for $L = 1$, store them on disk and then scale them by a factor $\frac{1}{L^2}$ or $\frac{1}{L}$ for the kinetic and Coulomb integrals respectively.

On other words, the integrals have to be calculated only once and then can be applied to systems of any size.

3.2.1 Completeness and Linear Dependence.

The Gaussian functions used as a basis are normalized but non-orthogonal to each other. This gives rise to an overlap matrix, S. Therefore, in general, we have to solve an eigenvalue problem. We can write the general eigenvalue problem as

$$Hx = ESx, \tag{3.16}$$

where H is the matrix representation of the Hamiltonian, S is the overlap matrix, E and x are the eigenvalues and eigenvectors, respectively. The Hamiltonian and overlap matrices are hermitian (usually real and symmetric) matrices. Solving Eq. 3.16, together with the computation of the electronic repulsion integrals, usually constitutes the dominant computational bottleneck due to the M^3 scaling of the diagonalization procedure where M is the size of the matrix. Instead, if we work with an orthogonal basis, S becomes the identity matrix, and we can rewrite Eq. 3.16 as

$$Hx = Ex. \tag{3.17}$$

This last equation is known as the standard eigenvalue problem. It is known that the standard eigenvalue solution is significantly faster to compute than the generalized eigenvalue solution for a large numbers of basis functions [56]. Moreover, depending on the characteristic of the problem to solve (symmetry, real/complex matrix, ...) there are several well-optimized and parallelized subroutines to solve eigenvalue problems, e.g. DSYEV for real and symmetric matrices or GNEP for generalized nonsymmetric eigenproblems, to mention some, from The Linear Algebra Package (LAPACK), library [57]. Thus it is preferred to have an orthogonal basis set.

There are several ways of orthogonalizing the basis set, such as Gram-Schmidt orthogonalization, symmetric (or Löwdin) orthogonalization, or canonical orthogonalization [58, 59, 60]. The symmetric orthogonalization possesses one remarkable feature, the Löwdin vectors bear the same symmetry as the original ones. That is the main reason why we have chosen the symmetric orthogonalization scheme.

However, if there are linear or quasilinear dependencies in the basis set, some of the eigenvalues of S will be close to zero. This which can lead to numerical instabilities of orthogonalization procedure. In the following, we will discuss how we can avoid these quasilinear dependencies.

If we look at Eqs. (3.11) and (3.12), we can identify two limiting cases we need to avoid. First, the overlap will go to zero for large values of ξ, and we cannot properly describe the wave function. Second, the overlap between two nearest neighbor Gaussians will become close to one for small values of ξ, yielding quasilinear dependencies. Then, it is important to select a value for ξ, which allows having enough overlap to describe a smooth wave function while, at the same time, avoiding linear or quasilinear dependencies when the overlap is too large. We can address this problem by a numerical tests where we explore the accuracy of the basis set by reproducing the exact energy of a system for various values of ξ [61].

We note that the comparison with exact results cannot be made if we do not remove the transverse kinetic energy. The transverse kinetic energy comes from the fact that we are using 3D $1s$-GTOs. The 1- and 2- dimensional systems we will discuss in the following chapters are, in reality, quasi-one- and quasi-two-dimensional. This means that the energy of a quasi-one-dimensional system has a contribution coming from the two transverse components. On the other hand, a quasi-two-dimensional system has a contribution coming from one transverse component. In the framework of distributed Gaussians, the use of a common exponent allows for the factorization of the transverse components and its subsequent removal from the quasi-one- and quasi-two-dimensional total energies to obtain their 1- and 2- dimensional energies. A 1-s Gaussian function in its Cartesian representation can be decomposed as

$$g(x, y, z) = g(x)g(y)g(z), \tag{3.18}$$

where g_x, g_y, and g_z components are given by

$$g(x) = \left(\frac{2\alpha}{\pi}\right)^{\frac{1}{4}} e^{-\alpha x^2} \tag{3.19}$$

$$g(y) = \left(\frac{2\alpha}{\pi}\right)^{\frac{1}{4}} e^{-\alpha y^2} \tag{3.20}$$

$$g(z) = \left(\frac{2\alpha}{\pi}\right)^{\frac{1}{4}} e^{-\alpha z^2}. \tag{3.21}$$

If we compute the kinetic energy in each dimension, we will have that the transverse energy per electron in each dimension is

$$\langle g(x)|\hat{T}_x|g(x)\rangle = \langle g(y)|\hat{T}_y|g(y)\rangle = \langle g(z)|\hat{T}_z|g(z)\rangle = \frac{\alpha}{2} \tag{3.22}$$

Thus, the transverse kinetic energy that needs to be subtracted in order to be able to compare the calculated energies to the exact to one- and two-dimensional energies is

$$E_{transverse} = N\frac{(3-d)\alpha}{2} \tag{3.23}$$

where N is the number of electrons, and d is the dimension of the system. As it can be seen from (3.23), the transverse energy for a 3-dimensional system will be 0, as it should.

3.3 Symmetry-adapted orbitals.

Due to the periodicity of the Clifford supercell, the system is translationally invariant. Therefore, the translation operator, $\hat{T}_R$, commutes with the Hamiltonian, $\hat{H}$, and the eigenstates of $\hat{H}$ can be chosen to be equal to the eigenstates of $\hat{T}_R$. It is hence convenient to construct symmetry-adapted orbitals (SAOs) from a linear combination of GTOs that satisfy the translational invariance [62]. The (unnormalized) SAO are defined as

$$\phi_{\mathbf{k}}(\mathbf{r}) = \frac{1}{m^{d/2}}\sum_{\boldsymbol{\mu}} e^{i\frac{2\pi}{m}\mathbf{k}\cdot\boldsymbol{\mu}} g_{\boldsymbol{\mu}}(\mathbf{r}-\mathbf{R}_{\boldsymbol{\mu}}), \tag{3.24}$$

where $\mathbf{k} = (k_1, \cdots, k_d)^T$ with $k_i = 0, \cdots, m-1$. We refer the reader to Appendix A for a proof of the fact that $\hat{T}_R\phi_{\mathbf{k}}(\mathbf{r}) = \phi_{\mathbf{k}}(\mathbf{r})$.

The one- and two-electron integrals in the symmetry-adapted basis are given by, respectively,

$$T_{\mathbf{k},\mathbf{k}'} = \delta_{\mathbf{k},\mathbf{k}'}\mathcal{S}_{\mathbf{k}}^{-1}\sum_{\boldsymbol{\nu}}\cos\left[\frac{2\pi}{m}(\mathbf{k}\cdot\boldsymbol{\nu})\right]T_{\mathbf{0},\boldsymbol{\nu}}, \tag{3.25}$$

$$\begin{aligned}\langle \mathbf{k},\mathbf{k}'|\mathbf{k}'',\mathbf{k}'''\rangle &= \frac{1}{m^d}\delta_{\mathbf{k}+\mathbf{k}'-\mathbf{k}''-\mathbf{k}'''}[\mathcal{S}_{\mathbf{k}}\mathcal{S}_{\mathbf{k}'}\mathcal{S}_{\mathbf{k}''}\mathcal{S}_{\mathbf{k}'''}]^{-1/2}\\ &\times\sum_{\boldsymbol{\nu\rho\sigma}}\cos\left[\frac{2\pi}{m}(\mathbf{k}'\cdot\boldsymbol{\nu}-\mathbf{k}''\cdot\boldsymbol{\rho}-\mathbf{k}'''\cdot\boldsymbol{\sigma})\right]\langle\mathbf{0},\boldsymbol{\nu}|\boldsymbol{\rho},\boldsymbol{\sigma}\rangle,\end{aligned} \tag{3.26}$$

in which $\mathcal{S}_{\mathbf{k}} = \langle \phi_{\mathbf{k}} | \phi_{\mathbf{k}} \rangle$. The one- and two-electron integrals, $T_{\boldsymbol{\mu},\boldsymbol{\nu}}$ and $\langle \boldsymbol{\mu}, \boldsymbol{\nu} | \boldsymbol{\rho}, \boldsymbol{\sigma} \rangle$, are expressed in the distributed Gaussian basis are given by [55]

$$T_{\boldsymbol{\mu},\boldsymbol{\nu}} = -\frac{1}{2} \int g_{\boldsymbol{\mu}}(\mathbf{r}_1 - \mathbf{R}_{\boldsymbol{\mu}}) \nabla_1^2 g_{\boldsymbol{\nu}}(\mathbf{r}_1 - \mathbf{R}_{\boldsymbol{\nu}}) d\mathbf{r}_1, \tag{3.27}$$

$$\begin{aligned} \langle \boldsymbol{\mu}, \boldsymbol{\nu} | \boldsymbol{\rho}, \boldsymbol{\sigma} \rangle = & \iint g_{\boldsymbol{\mu}}(\mathbf{r}_1 - \mathbf{R}_{\boldsymbol{\mu}}) g_{\boldsymbol{\nu}}(\mathbf{r}_2 - \mathbf{R}_{\boldsymbol{\nu}}) \times \\ & \frac{1}{r_{12}^{euc}} g_{\boldsymbol{\rho}}(\mathbf{r}_1 - \mathbf{R}_{\boldsymbol{\rho}}) g_{\boldsymbol{\sigma}}(\mathbf{r}_2 - \mathbf{R}_{\boldsymbol{\sigma}}) d\mathbf{r}_1 d\mathbf{r}_2. \end{aligned} \tag{3.28}$$

The derivation of the one- and two-electron integrals in the symmetry adapted basis can be found in the Appendix A.

3.3.1 Integral transformation

It is known that the evaluation of the molecular integrals, together with the diagonalization procedure, is one of the main bottlenecks in electronic structure calculations. The computation of the AO integrals and their transformation onto the symmetry-adapted basis set must be done efficiently. The one-electron integrals are in a limited number, and they do not present a particular problem. Moreover, its evaluation in the SAO, Eq. (3.25), depends only on one orbital index because of the system symmetry, so the implementation is straightforward. On the other hand, the situation is different for the two-electron integrals.

We can use two complementary strategies to compute Eq. (3.26) efficiently. First we transform the expression $\cos(\mathbf{k}' \cdot \boldsymbol{\nu} - \mathbf{k}'' \cdot \boldsymbol{\rho} - \mathbf{k}''' \cdot \boldsymbol{\sigma})$ by taking advantage of the identity

$$\begin{aligned} \cos(\alpha + \beta + \gamma) = & \cos(\alpha)\cos(\beta)\cos(\gamma) - \sin(\alpha)\sin(\beta)\cos(\gamma) - \sin(\alpha)\cos(\beta)\sin(\gamma) - \\ & \cos(\alpha)\sin(\beta)\sin(\gamma). \end{aligned} \tag{3.29}$$

The expression for the two-electron integrals can be rewritten as

$$\begin{aligned}\langle \mathbf{k}, \mathbf{k}''|\mathbf{k}''', \mathbf{k}''''\rangle = \delta(\mathbf{k}+\mathbf{k}''-\mathbf{k}'''-\mathbf{k}'''')\frac{1}{M}\sum_{\boldsymbol{\nu\rho\sigma}=\mathbf{0}}^{\mathbf{M-1}}\Big[&\cos(\mathbf{k}''\cdot\boldsymbol{\nu})\cos(\mathbf{k}'''\cdot\boldsymbol{\rho})\cos(\mathbf{k}''''\cdot\boldsymbol{\sigma})+\\ &+\sin(\mathbf{k}''\cdot\boldsymbol{\nu})\sin(\mathbf{k}'''\cdot\boldsymbol{\rho})\cos(\mathbf{k}''''\cdot\boldsymbol{\sigma})+\sin(\mathbf{k}''\cdot\boldsymbol{\nu})\cos(\mathbf{k}'''\cdot\boldsymbol{\rho})\sin(\mathbf{k}''''\cdot\boldsymbol{\sigma})-\\ &-\cos(\mathbf{k}''\cdot\boldsymbol{\nu})\sin(\mathbf{k}'''\cdot\boldsymbol{\rho})\sin(\mathbf{k}''''\cdot\boldsymbol{\sigma})\Big]\langle \mathbf{0},\boldsymbol{\nu}|\boldsymbol{\rho},\boldsymbol{\sigma}\rangle.\end{aligned} \tag{3.30}$$

We now have four terms, each of which scales as $3M^4$, yielding a huge computational advantage. For instance, if we consider the first term on the right-hand side of Eq.(3.30) involving three cosine functions,

$$\begin{aligned}\langle \mathbf{k}, \mathbf{k}''|\mathbf{k}''', \mathbf{k}''''\rangle_{ccc} = \delta(\mathbf{k}+\mathbf{k}''-\mathbf{k}'''-\mathbf{k}'''')\frac{1}{M}\sum_{\boldsymbol{\nu\rho\sigma}=\mathbf{0}}^{\mathbf{M-1}}\cos(\mathbf{k}''\cdot\boldsymbol{\nu})\cos(\mathbf{k}'''\cdot\boldsymbol{\rho})\times\\ \cos(\mathbf{k}''''\cdot\boldsymbol{\sigma})\langle \mathbf{0},\boldsymbol{\nu}|\boldsymbol{\rho},\boldsymbol{\sigma}\rangle\end{aligned} \tag{3.31}$$

we can compute it through the following three steps:

$$\langle \boldsymbol{\nu}|\boldsymbol{\rho}, \mathbf{k}''''\rangle_{ccc} = \sum_{\boldsymbol{\sigma}}\cos(\boldsymbol{\sigma}\cdot\mathbf{k}'''')\langle \mathbf{0},\boldsymbol{\nu}|\boldsymbol{\rho},\boldsymbol{\sigma}\rangle \tag{3.32}$$

Then

$$\langle \boldsymbol{\nu}|\mathbf{k}''', \mathbf{k}''''\rangle_{ccc} = \sum_{\boldsymbol{\rho}}\cos(\boldsymbol{\rho}\cdot\mathbf{k}''')\langle \boldsymbol{\nu}|\boldsymbol{\rho},\mathbf{k}''''\rangle_{ccc} \tag{3.33}$$

and, as the last step,

$$\langle \mathbf{k}'''+\mathbf{k}''''-\mathbf{k}''|\mathbf{k}''', \mathbf{k}''''\rangle_{ccc} = \frac{1}{M}\sum_{\boldsymbol{\nu}}\cos(\boldsymbol{\nu}\cdot\mathbf{k}'')\langle \boldsymbol{\nu}|\mathbf{k}''',\mathbf{k}''''\rangle_{ccc} \tag{3.34}$$

where the index $k'''+k''''-k''$ fulfils the Kronecker-δ constraint. Similarly, we can compute the other three terms of Eq. (3.30).

As a final result, Eq. (3.30) scales as $12M^4$, while the memory requirements are of the order of $2M^3$ real numbers.
Second, we can take advantage of the fact that $\langle \mathbf{0}, \boldsymbol{\nu} | \boldsymbol{\rho}, \boldsymbol{\sigma} \rangle$ is sparse. This means that the centers of Gaussians g_ρ and g_σ must be close to the center of Gaussians $g_{\mathbf{0}}$ and g_ν, respectively. Otherwise, its contribution to $\langle \mathbf{k}, \mathbf{k}\text{”} | \mathbf{k}''', \mathbf{k}'''' \rangle$ will be vanishingly small. Let us make the term "close" more precise: we assume that the distance between the two centers must be smaller than an integer threshold λ times δ, the nearest-neighbour distance. Then Eq. (3.26) becomes then.

$$\begin{aligned} \langle \mathbf{k}, \mathbf{k}' | \mathbf{k}'', \mathbf{k}''' \rangle = & \frac{1}{m^d} \delta_{\mathbf{k}+\mathbf{k}'-\mathbf{k}''-\mathbf{k}'''} \sum_{\nu} \sum_{|\rho| \leq \lambda} \sum_{|\sigma - \nu| \leq \lambda} \\ & \cos \left[\frac{2\pi}{m} \left(\mathbf{k}' \cdot \boldsymbol{\nu} - \mathbf{k}'' \cdot \boldsymbol{\rho} - \mathbf{k}'' \cdot \boldsymbol{\sigma} \right) \right] \langle \mathbf{0}, \boldsymbol{\nu} | \boldsymbol{\rho}, \boldsymbol{\sigma} \rangle. \end{aligned} \tag{3.35}$$

We note that the first strategy is exact while the second one is an approximation. Moreover, they can be applied simultaneously.

3.4 A step forward: Toroidal Gaussians

We note that, strictly speaking, a Gaussian function is defined everywhere in space, while, in principle, the functions we use to describe the electrons in the CSC must be periodic smooth functions confined to the torus. A Gaussian function is not a function with a compact support, is not a continuous and differentiable function defined everywhere on the torus (see the top left side of Fig. 3.5). However, if the width of the Gaussian is much smaller than the size of the torus, then, for any practical purpose, this function can be considered as a function having a compact support on the torus (see the bottom side of

Fig. 3.5). Therefore, by combining various Gaussians centered on a regular grid on the torus, we can build periodic smooth wave functions on this manifold.

Nevertheless, a Gaussian basis function confined to the CSC would have numerical advantages. Therefore, we have recently formulated a new basis function using toroidal Gaussians. The motivation for the present development comes from the work done by Loos and Gill, where they introduced spherical Gaussian orbitals to describe the behavior of electrons on a 2D or 3D sphere [63] . Following the same philosophy as in the reference mentioned above, on a Clifford torus, continuous and differentiable Gaussian orbitals can be defined by using the definition of the Euclidean distance given in Chapter 2. In one dimension, one can write a toroidal Gaussian on a 1-Torus of length L with orbital exponent α, centered at x_μ as

$$g_\mu^T(x;\alpha,L) = N_{\alpha,L} e^{-\frac{\alpha L^2}{\pi^2}\sin^2\left(\frac{\pi(x-x_\mu)}{L}\right)}, \tag{3.36}$$

where $N_{\alpha,L}$ is the normalization constant. Using trigonometric identities we can rewrite Eq. (3.36) into its equivalent cosine form as

$$g_\mu^T(x;\alpha,L) = N_{\alpha,L} e^{-\frac{\alpha L^2}{2\pi^2}\left[1-\cos\left(\frac{2\pi(x-x_\mu)}{L}\right)\right]}, \tag{3.37}$$

In order to keep the characteristic fast and simple integral evaluation of the GTOs, we want that our toroidal Gaussians satisfy the Gaussian product rule. This means that the product of two g^T has to be another toroidal Gaussian.

It can be proved that.

$$\begin{aligned} g_\mu^T(x;\alpha,L)g_\nu^T(x;\beta,L) =& e^{-\frac{L^2}{2\pi^2}\left(\alpha+\beta-\sqrt{\alpha^2+\beta^2+2\alpha\beta\cos\left(\frac{2\pi(x_\mu-x_\nu)}{L}\right)}\right)}\times \\ & e^{-\frac{L^2}{2\pi^2}\sqrt{\alpha^2+\beta^2+2\alpha\beta\cos\left(\frac{2\pi(x_\nu-x_\nu)}{L}\right)}\left(1-\cos\left(\frac{2\pi(x-x_\gamma)}{L}\right)\right)} \qquad (3.38) \\ =& g_\mu^T(x;\gamma,L) \qquad (3.39) \end{aligned}$$

where the exponent and center of the new g_γ^T are

$$\gamma = \sqrt{\alpha^2+\beta^2+2\alpha\beta\cos\left(\frac{2\pi(x_\mu-x_\nu)}{L}\right)} \qquad (3.40)$$

$$x_\gamma = \arctan\frac{\alpha\sin\frac{2\pi x_\mu}{L}+\beta\sin\frac{2\pi x_\nu}{L}}{\alpha\cos\frac{2\pi x_\mu}{L}+\beta\cos\frac{2\pi x_\nu}{L}} \qquad (3.41)$$

From Eq. (3.39) we can compute the overlap $\mathcal{S}_{\mu\nu}$ integrals and its norm, $\|g_\mu^T\|$ as

$$\mathcal{S}_{\mu\nu}(\alpha,\beta,L) = \frac{I_0\left(L^2\sqrt{\alpha^2+\beta^2+2\alpha\beta\cos\frac{2\pi(x_\mu-x_\nu)}{L}}\right)}{\sqrt{I_0(2\alpha L^2)I_0(2\beta L^2)}} \qquad (3.42)$$

$$\|g_\mu^T(x;\alpha,L)\| = \sqrt{I_0(2\alpha L^2)} \qquad (3.43)$$

where $I_n(z)$ is the modified Bessel function of the first kind.

Let us now analyze the shape of a g^T and compare it with a standard 1-s Gaussian. For that purpose, we have collected in Fig. 3.5 a comparison between the shapes of several g^Ts (in red) and 1-s Gaussian functions (in blue) for different values of α. The space coordinate (x) is defined in the interval $[-\pi,\pi]$, and the two Gaussians are centered at $x=0$. Generally speaking, for small values of L_x and r, the behavior of the six curves follows a similar trend. It is because in the interval $[-0.5,0.5]$, $\frac{L_x^2}{\pi^2}\sin^2\left(\frac{\pi(x-x_0)}{L_x}\right)\approx(x-x_0)^2$.

The biggest difference shows up at long-range. For small values of α, the tail of g^T decays smoothly, while the Gaussian function with the same exponent has a faster decay. An important feature of g^T is that it is periodic and differentiable at the borders of the CSC while the usual Gaussians are not (see Fig. 3.5). For large values of α, the two curves completely overlap. We also note that the two functions have 0 first derivative at the origin. It can also be proved that $\lim_{L\to\infty} \frac{L^2}{2\pi}\left[1-\cos\left(\frac{2\pi(x-x_\mu)}{L}\right)\right] = x - x_\mu$ and $g^T \equiv g$.

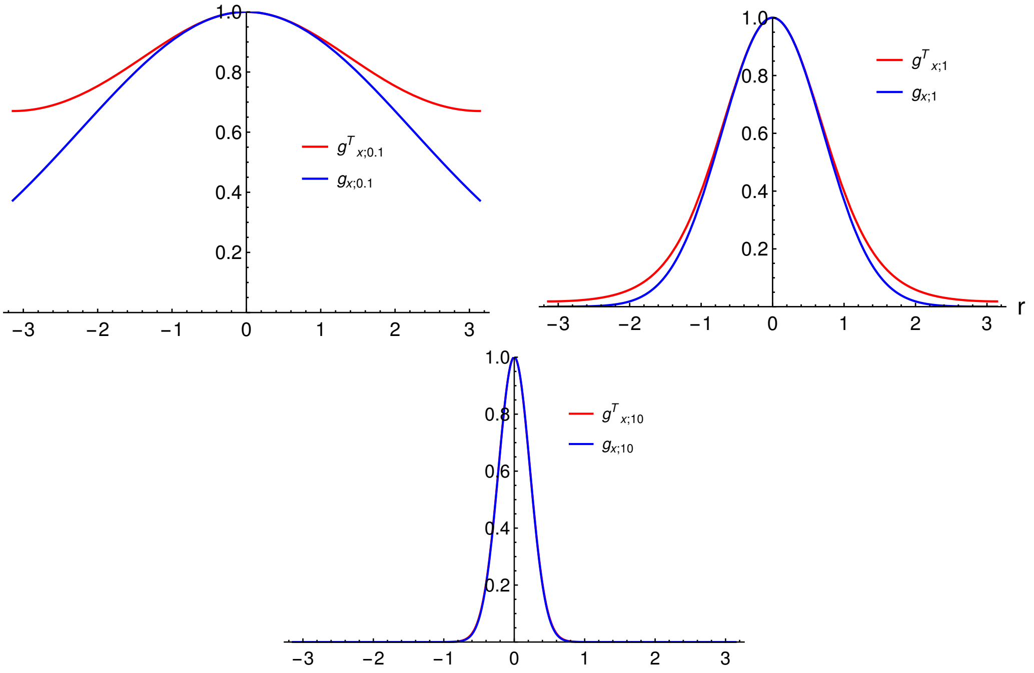

Figure 3.5: Difference between the radial distribution of toroidal Gaussians and usual Gaussians. Top left: $g_0^T(x; 0.1, 2\pi)$ vs $g_0^T(x; 0.1)$. Top right: $g_0^T(x; 1, 2\pi)$ vs $g_0^T(x; 1)$. Bottom: $g_0^T(x; 10, 2\pi)$ vs $g_0^T(x; 10)$.

We notice that for $\alpha = \beta$, the exponent γ vanishes if the two orbitals are centered in two opposite positions of the torus. In fact, if $x_\mu - x_\nu = \frac{L}{2}$, the cosine in Eq. (3.40) is equal to -1 and $\gamma = \sqrt{2\alpha^2 - 2\alpha^2)} = 0$.

We expect that we would need less toroidal Gaussians than standard Gaussians to arrive at a wave function of similar accuracy. However, the application of the toroidal Gaussians to practical calculations on Wigner systems is still work in progress. Therefore, in the remainder of the manuscript we will use standard Gaussians.

Chapter 4

Wigner localization: 2 electrons on a ring

Contents

4.1 Motivation

In a previous work, Evangelisti, Berger and coworkers, studied Wigner localization in a quasi-one-dimensional system in which the electrons were confined to a line segment with a positive background by placing three-dimensional Gaussians along the line [9, 61]. They observed Wigner localization at low densities. Although the localization they observed was clearly due to the electronic repulsion, quantitatively the results were influenced by border effects. Moreover, they used a multi-purpose software for the numerical calculations due to which they were limited to system sizes smaller than 100 Bohr. Due to these restrictions they were not able to fully appreciate the delta-peak nature of the Wigner localization in the many-body wave function.

Before using Clifford boundary conditions we first study a simpler system, namely 2 electrons on a ring. Thus, removing any border effects. We expand the wave function in terms of three-dimensional Gaussians evenly distributed along the perimeter of the ring [64, 65, 66, 67]. For this purpose, we wrote a computer code that is specifically dedicated to treat low densities which allows us to reach ring perimeters as large as 10^6 Bohr ($\approx 0.05\ mm$). We note that confining the electrons to a ring also removes the need to add a positive background [65]. As described in the following, with this approach we are able to see the delta-peak nature of the localization in the many-body wave function.

Here we limit our study to two electrons since it is sufficient to observe the Wigner localization while at the same time it allows us to obtain numerically exact results by exact diagonalization of the Hamiltonian. We will analyze several possible indicators of localization. In particular, we will study the

2-body reduced density matrix, the localization tensor and the particle-hole entropy.

This work has been published in: Miguel Escobar Azor, Léa Brooke, Stefano Evangelisti, Thierry Leininger, Pierre-François Loos, Nicolas Suaud, Arjan Berger. "A Wigner molecule at extremely low densities: a numerically exact study." SciPost Physics Core 1, no. 1 (2019): 001

4.2 Theory

4.2.1 The Hamiltonian

As mentioned before, we study two electrons that are confined to a ring. Moreover, in the transverse directions, the two electrons are confined by a potential that is implicitly defined by the basis set which consists of M identical 3D s-type Gaussians that are evenly distributed along the ring as explained in Chapter 3. These normalized Gaussian functions were given in Eq. (3.6), which we repeat here for convenience,

$$g_\mu(\mathbf{r};\alpha) = \left(\frac{2\alpha}{\pi}\right)^{\frac{3}{4}} e^{-\alpha|\mathbf{r}-\mathbf{R}_\mu|^2}, \tag{4.1}$$

in which $\mathbf{R}_\mu$ denotes the center of the Gaussian and α its exponent which is directly linked to the width of the Gaussian function ($\sim 1/\sqrt{\alpha}$). Since the Gaussians are 3D also the ring is 3D, or rather, quasi-1D, since the width of the ring is much smaller than its perimeter. We, therefore, have the following Hamiltonian,

$$\hat{H} = -\frac{1}{2}\nabla_1^2 - \frac{1}{2}\nabla_2^2 + \frac{1}{r_{12}}, \tag{4.2}$$

in which the first two terms on the right-hand side are the 3D kinetic energy operators for electron 1 and 2, respectively. The last term is the repulsive 3D Coulomb potential in which $r_{12} = |\mathbf{r}_1 - \mathbf{r}_2|$ is the distance between the two electrons, i.e., the electrons interact through the ring. This is equivalent to the euclidean distance defined in Eq. (2.9).

We represent the Hamiltonian in Eq. (4.2) in the basis of the evenly distributed gaussians which we then diagonalize to find the exact wave functions and eigenenergies. From the exact wave functions we can then obtain several exact observables of interest. We will mainly focus on the ground state of two electrons on the ring which is a spin singlet.

We have verified our approach and its implementation by comparing to analytical results which are available for one electron confined to a strictly 1D ring. They are given by

$$E_n^{\text{exact}}(R) = \frac{n^2}{2R^2}, \tag{4.3}$$

where n is an integer and R is the radius of the ring. When the width of the gaussians ($\sim 1/\sqrt{\alpha}$) is much smaller than R, the energy spectrum of the system tends to the energies in Eq. (4.3). We note, however, that some caution must be used when evaluating distances in the system, even in the limit $1/\sqrt{\alpha} \to 0$. In particular, when computing overlaps and kinetic energies, it is only when each distance is measured along an arc of the ring that in the limit $1/\sqrt{\alpha} \to 0$ the energies tend to those given in Eq. (4.3). We note that this is equivalent to the geodesic distance introduced in the chapter 2.

Since the density, by definition, has the same symmetry as the Hamiltonian it will have rotational symmetry. Therefore, the one-body density will be a constant as a function of the position on the ring, and unable to characterize the Wigner localization. However, for 2 electrons, the Wigner localization can be studied using the two-body density matrix, which shows the correlation between the positions of two electrons.

We note that the present scenario defines a floating Wigner crystal. Another scenario corresponds to a pinned Wigner crystal where the spatial symmetry of the wave function is broken by a small external perturbation or impurity [68]. In this case, the Wigner crystallization can be observed via the 1-body density. We will not consider such situations in this chapter.

4.2.2 The 2-body reduced density matrix

The N-body reduced density matrix (N-RDM) gives the conditional probability of the presence of N electrons in space. The 2-body reduced density matrix $\Gamma^{(2)}$ is defined as

$$\Gamma^{(2)}(x_1, x_2; y_1, y_2) = \frac{(N-1)N}{2} \int dx_3 \cdots dx_N \\ \times \Psi^*(y_1, y_2, x_3, \cdots, x_N)\Psi(x_1, x_2, \cdots, x_N), \quad (4.4)$$

in which Ψ is an N-body normalised wave function. In particular, its diagonal elements $\Gamma(x_1, x_2) = \Gamma^{(2)}(x_1, x_2; x_1, x_2)$ give the probability of having an electron at x_1 and a second electron located at x_2. For two electrons it is given by

$$\Gamma(x_1, x_2) = |\Psi(x_1, x_2)|^2. \quad (4.5)$$

In the present 1D context, the 2-RDM plays a crucial role in measuring the locality of the electrons. Indeed, because of the rotational invariance of the wave function the 1-RDM is a constant, regardless of the nature of the wave function, since all points in space are equivalent. It is the 2-RDM, on the other hand, that is able to indicate if the electrons are strongly correlated

(Wigner localization), or weakly correlated (Fermi gas).

The situation is rather different, on the other hand, for 2D and 3D generalizations of electrons on a ring (1-torus), i.e., electrons on a 2-torus and a 3-torus.[1] Just as the diagonal of the 1-RDM is a constant for a ring due to symmetry, the diagonal of the 2-RDM is a constant for the 2-torus. This implies that the 2-RDM is unable to give a complete characterization of a regular crystalline structure on the 2-torus. Similarly, the 3-RDM is a constant for the 3-torus, and is unable to characterize the crystallisation of the electrons. Higher-order density matrices would be in principle needed for this purpose, e.g. the 3-RDM for 2-tori, and the 4-RDM for 3-tori, etc. However, the evaluation of higher-order density matrices are computationally extremely demanding, and their calculation would become unfeasible even for very small systems. In such a situation, other indicators, like the electron entropy, and in particular the localization tensor, would be much more practical.

4.2.3 The localization tensor

The localization tensor distinguishes between metallic and insulating behavior. It was developed by Resta and co-workers [69, 70, 71, 72] (see also Ref. [73]) and is based on an idea of Kohn [74] to describe the insulating state from the knowledge of the ground-state wave function (see also Ref. [75]). The localization tensor has been applied to study the metallic behavior of clusters, [76, 77, 78, 79, 80, 81, 82, 83, 84], chemical bonding [85] and electron transport [86]. It has recently also been used to investigate Wigner localization. [9]

The localization tensor $\boldsymbol{\lambda}$ is defined as the total position spread tensor $\boldsymbol{\Lambda}$

---

[1] Here we mean a regular torus, not a Clifford torus.

normalized with respect to the number of electrons N, i.e.,

$$\boldsymbol{\lambda} = \frac{\boldsymbol{\Lambda}}{N}. \tag{4.6}$$

The total position spread tensor is defined as the second moment cumulant of the total position operator,

$$\boldsymbol{\Lambda} = \langle \Psi | \hat{\mathbf{R}}^2 | \Psi \rangle - \langle \Psi | \hat{\mathbf{R}} | \Psi \rangle^2, \tag{4.7}$$

in which the total position operator $\hat{\mathbf{R}}$ is defined by

$$\hat{\mathbf{R}} = \sum_{i=1}^{N} \hat{\mathbf{r}}_i. \tag{4.8}$$

where $\hat{\mathbf{r}}_i = \mathbf{r}_i$ the standard position operator for electron i.

The three diagonal elements of $\boldsymbol{\Lambda}$ are the variances of the wave function in the x, y, and z directions. Therefore, these elements are large when the electrons are delocalized and small when they are localized. This shows that the localization tensor is able to distinguish between a conducting and an insulating behavior. Moreover, in the thermodynamic limit the localization tensor diverges for conductors while it remains finite in the case of insulators. We note that the second term on the right-hand side of Eq. (4.7) ensures gauge invariance with respect to the choice of the origin of the coordinate system.

Due to the symmetry of the ring we have $\lambda_{xx} = \lambda_{yy}$ and $\lambda_{zz} \ll \lambda_{xx}$. In the following we will focus on the trace of $\boldsymbol{\lambda}$, i.e.,

$$\lambda = \mathrm{Tr}\{\boldsymbol{\lambda}\}. \tag{4.9}$$

4.2.4 The particle-hole entropy

The fractionality of the natural occupation numbers, i.e., the eigenvalues associated with the 1-RDM, can be related to the amount of electron correlation in a system [87, 88]. Therefore, the particle-hole entropy has been proposed as a measure of the presence of correlation in a system [89, 88]. In the case of a pure state described by a wavefunction Ψ, the particle-hole entropy is defined as:

$$S = \sum_{j=1}^{M} \Big[\underbrace{-n_j \ln n_j}_{S_{\mathrm{part}}} \underbrace{-(1-n_j)\ln(1-n_j)}_{S_{\mathrm{hole}}} \Big], \tag{4.10}$$

where the sum runs over the M natural spinorbitals of Ψ, and n_j is the occupation number of spinorbital ϕ_j. The natural spinorbitals are the eigenfunctions of the one-body reduced spin-density matrix and the occupations numbers are its eigenvalues. The first and second terms in the summation are the particle and hole contributions, S_{part} and S_{hole}, respectively, to the total entropy. While the entropy of a single determinant is zero, since all the occupation numbers are either 0 or 1, the entropy has its maximum value when all the spinorbitals have equal occupation numbers. Therefore, the particle-hole entropy of a Fermi gas will be small while it will be large in the regime of Wigner localization. In particular, this will be the case for an $S_z = 0$ wave function because of the large number of Slater determinants that contribute to the wave function with similar weight. Indeed, we have an $S_z = 0$ ground-state wave function.

The dependence of the particle-hole entropy on the natural spinorbitals implies a dependence on the basis set. For large densities this dependence is negligible but in the limit of Wigner localization there is a strong dependence on the basis set. This dependence can be made explicit as we will now show.

All the occupation numbers become identical when the length of the perimeter of the ring tends to infinity and the electrons localize. This leads to an upper bound for the entropy in the limit $L \to \infty$. Let us consider N electrons in M spinorbitals. In the limit $L \to \infty$ each spinorbital ϕ_j has occupation number $n_j = N/M$. Therefore, we obtain the following upper bounds for the particle and hole entropies in the limit $L \to \infty$,

$$\lim_{L\to\infty} S_{\text{part}} = -N \ln(N/M), \tag{4.11}$$

$$\lim_{L\to\infty} S_{\text{hole}} = -(M-N) \ln(1-N/M). \tag{4.12}$$

If we subsequently let the number of gaussians, and thereby the number of spinorbitals M, tend to infinity, we see that particle entropy diverges logarithmically as

$$\lim_{L\to\infty} S_{\text{part}} \sim -N \ln(N/M). \tag{4.13}$$

Instead, in this limit, the hole entropy tends to a constant, namely the number of electrons,

$$\lim_{M\to\infty} \lim_{L\to\infty} S_{\text{hole}} = N. \tag{4.14}$$

The total entropy therefore behaves as

$$S = -N \ln(N/M) + N + \mathcal{O}\Big(M^{-1}\Big). \tag{4.15}$$

for large L and M.

4.3 Computational details

As mentioned before, we study a quasi-1D periodic system of electrons by placing a series of identical 3D Gaussian functions [see. Eq. (4.1)] to form a ring. The centers of the Gaussians are equally spaced. As discussed in chapter 3, the overlap between two neighboring Gaussians is proportional to the parameter $\xi = \alpha\delta^2$, where α is the exponent of the Gaussian and δ is the distance along the arc between two neighboring Gaussians [61]. The overlap should be sufficiently large to be able to accurately describe the electronic wave function but not too large to avoid numerical problems due to a quasi-linearly dependent basis functions. We have demonstrated that a value of $\xi \approx 1$ is optimal for quasi-1D systems [61]. In this work we used $\xi = 1$. We have used 128 equidistant gaussians which was sufficient to obtain converged results for rings with lengths up to 10^6 Bohr.

For two electrons the spin wave function can correspond either to a singlet or a triplet. Therefore, it is convenient to generate spin-adapted wave functions. This is particularly important at low density, where the singlet and triplet wave functions tend to become degenerate. In absence of spin adaptation, due to numerical errors, the diagonalization procedure could mix the two quasi-degenerate states, and therefore the computed properties would correspond to wave functions that are not eigenfunctions of $\hat{S}^2$.

4.4 Results

4.4.1 The 2-body reduced density matrix

As mentioned earlier, for a system without translational and/or rotational symmetry, such as a linear system within open-boundary conditions, a symmetry-broken system or a system with an impurity (i.e. pinned electrons), the electron density is sufficient to characterize the Wigner localization. [9] However, as explained in the previous section, in the case of a ring, due to the rotational symmetry of the Hamiltonian, the density is no longer a good observable to identify the Wigner localization. Instead, we can use the 2-body reduced density matrix to characterize this localization since it describes the correlation between the positions of two electrons.

In Fig. 4.1, we report the two-body reduced density matrix $\Gamma^{(2)}(0,x)$ as a function of x for different values of the length of the perimeter L of the ring. It gives the probability amplitude of finding an electron at x while another electron is present at $x=0$.[2]

At large electron density (small L), $\Gamma^{(2)}(0,x)$ is almost constant, since the kinetic energy dominates the electronic repulsion. This is the Fermi-gas regime. Instead, at low electron density (large L), the second electron has the largest amplitude at $x=L/2$, i.e., exactly at the position that is opposite to the position of the first electron. The electronic repulsion is dominant and pushes the two electrons to opposite positions on the ring. By increasing L the two-body reduced density matrix becomes ever more localized. For very large values of L the density matrix becomes close to a delta function. There is the

---

[2] To be precise, the results in Fig. 1 are the 2-RDM expressed in the basis of the orthonormal gaussians, i.e., $\Gamma_{i\alpha j\beta i\alpha j\beta} = \langle\Psi|a^\dagger_{i\alpha}a^\dagger_{j\beta}a_{i\alpha}a_{j\beta}|\Psi\rangle$ in which the first electron is fixed at $i=1$.

formation of a 1D electron "lattice", we observe the Wigner localization. It is difficult to pinpoint exactly for which length the transition from the Fermi to the Wigner regime occurs. Nevertheless, the Wigner localization becomes apparent for lengths of the order of $L = 10$ Bohr.

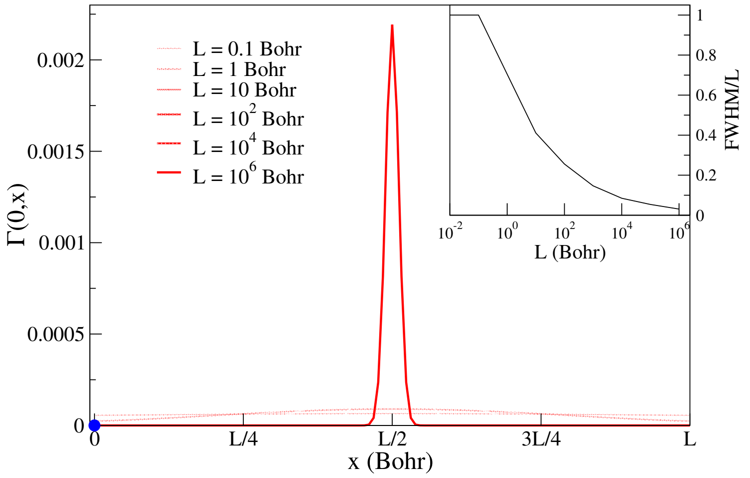

Figure 4.1: The two-body reduced density matrix $\Gamma(0, x)$ for two electrons on a ring for various values of the length L of the perimeter. The position of the first electron is fixed at $x = 0$ (indicated by the blue dot). Inset: Full-width at half maximum (FWHM) of $\Gamma^{(2)}(0, x)$ normalized with respect to L as a function of L. For small L the FWHM is not well-defined and the normalized FWHM is set to 1.

However, as mentioned before, the two-body reduced density is not sufficient to characterize Wigner localization for systems of higher dimensions. Therefore, we will study two other indicators of the Wigner localization, namely the localization tensor and the electron-hole entropy. The advantage of these quantities is that they can also be easily calculated for systems of higher dimensions and with many electrons.

4.4.2 The localization tensor

In order to compare localization tensors for systems of different sizes, we report in Fig. 4.2 the dimensionless quantity λ/L^2 as a function of the length L of the perimeter of the ring. We see that for large density ($L < 0.1$) λ/L^2 is almost constant while its value starts to decrease for $L > 1$ Bohr. This marks the beginning of the transition to a localized state. For very low density, $L \gg 1$, the localization tensor almost vanishes, clearly indicating the Wigner localization. The behavior of the localization tensor is in agreement with the 2-body reduced density matrices reported in Fig. 4.1, i.e, the transition from the Fermi-gas regime to the Wigner regime occurs in the region around $L = 10$ Bohr. Finally, we note that the qualitative behavior of the localization tensor we observe here for the ring is very similar to the behavior that was observed for a linear system within open boundary conditions [9]. Hence, the localization tensor seems to be a robust indicator of the transition to the Wigner regime.

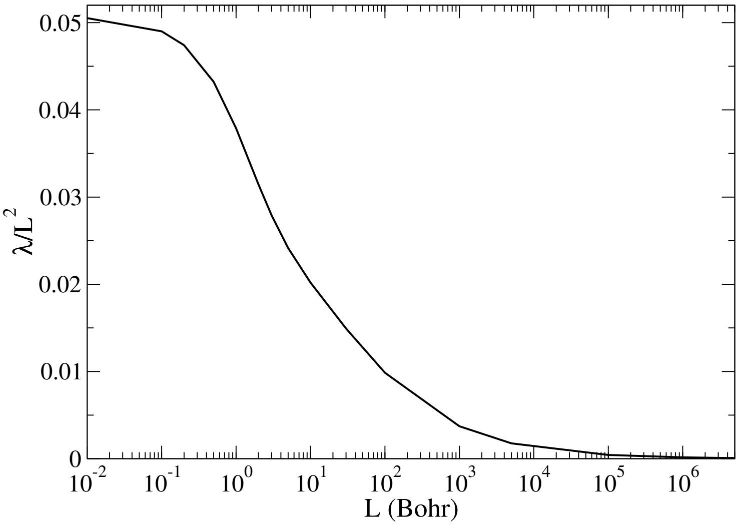

Figure 4.2: The trace of the localization tensor λ/L^2 as a function of the length L of the perimeter of the ring.

4.4.3 The particle-hole entropy

In Fig. 4.3, we report the particle-hole entropy as a function of the length L of the perimeter of the ring. For large average densities ($L \ll 1$) the entropy S is very small since the Fermi gas can be accurately described by a single Slater determinant. The entropy starts to rapidly increase for $L > 1$ Bohr, indicating the transition towards the Wigner regime.

Up to about $L = 10$ Bohr the entropy is qualitatively similar to the behavior of the entropy for a linear system. [9] However, while for the linear system the entropy stabilizes for $L > 10$ Bohr, for the ring it continues to increase linearly. This is due to the particle part of the entropy which grows linearly in the region $10^2 < L < 10^6$ while the hole part saturates in this region.

Although it might appear that the entropy diverges linearly with L, this is not the case. Using Eqs. (4.11) and (4.12) we can determine the asymptotic limits of the entropy and its two contributions (for a given M). They are finite and we reported them in Fig. 4.3. In order to reach the asymptotic limit of the total entropy we have to go beyond $L = 10^6$ Bohr which would require a larger number of gaussians to guarantee stable results. However, a larger number of gaussians yields a larger number of spinorbitals which will raise the asymptotic limit, requiring an even larger number of gaussians to reach it, etc. Due to this vicious circle, the particle-hole entropy is not capable of capturing the localized state. Therefore, the particle-hole entropy seems less convenient than the localization tensor as an indicator of Wigner localization, at least for electrons on a ring..

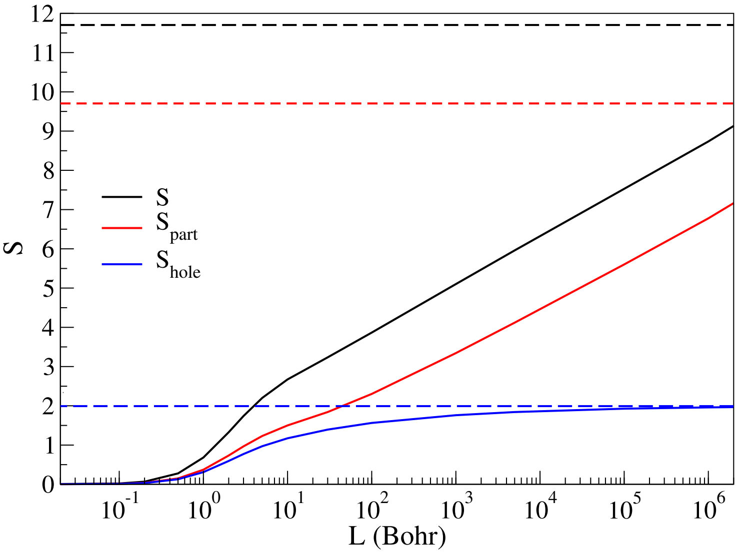

Figure 4.3: The entropy S as a function of the length L of the perimeter of the ring. The dashed lines indicate the asymptotic limits of the entropies when $L \to \infty$.

4.5 Conclusion

We have investigated Wigner localization at extremely low densities using an exact diagonalization of the many-body Hamiltonian for a system of two electrons confined to a ring. Due to the rotational symmetry of the system, Wigner localization cannot be observed in the local density. Therefore, we have studied alternative quantities, namely, the two-body reduced density matrix, the localization tensor and the particle-hole entropy. We have clearly observed the Wigner localization both in the two-body reduced density matrix and in the localization tensor. Instead, in the particle-hole entropy the Wigner localization cannot easily be detected. With respect to the two-body reduced density matrix, the advantage of the localization tensor is that it can also be applied without increased difficulty to systems with more dimensions and more electrons.

This study paves the way for further investigations of Wigner localization such as those presented in the next two chapters in which we will use the Clifford periodic boundary conditions to go beyond 1-dimension and include more than 2 electrons in the system.

CHAPTER 5

Wigner localization: two electrons on a Clifford torus.

Contents

5.1 Motivation

The main goal of this Chapter is to go beyond one dimension and to study Wigner localization from an *ab initio* perspective in two and three dimensions.

This will allow us to better understand this phenomenon and may lead to predictions of the properties of Wigner crystals and Wigner molecules in the future. As in the previous chapter we will use exact diagonalization of the many-body Hamiltonian to ensure that all correlation effects are included. We will focus here on two-electron systems since this is sufficient to demonstrate the concept of Wigner localization.

In this Chapter we generalize our approach to study Wigner localization at low densities in systems of two and three dimensions. As mentioned before, to study the Wigner localization in a d-dimensional system ($d = 1, 2, 3$), we can represent our system in different ways. We could confine the electrons to a finite d-dimensional system with a positive background, but border effects would influence the results [9]. One way of avoiding border effects is to confine the electrons to a d-dimensional closed space such as a d-torus but the numerical implementation of the geometry of a d-torus is cumbersome for $d > 1$. Therefore, instead, we apply Cliffod boundary conditions as explained in chapter 2.

This work has been published in: Miguel Escobar Azor, Estefania Alves, Stefano Evangelisti, and J. Arjan Berger. "Wigner localization in two and three dimensions: An ab initio approach." The Journal of Chemical Physics 155, no. 12 (2021): 124114.

5.2 Theory

We will study a system consisting of 2 interacting electrons confined to a d-dimensional Clifford torus.

The Hamiltonian of the system is

$$\hat{H} = -\frac{1}{2}\nabla_1^2 - \frac{1}{2}\nabla_2^2 + \frac{1}{r_{12}^{euc}}, \tag{5.1}$$

where the first two terms on the right-hand side correspond to the 3D kinetic energy of electron 1 and electron 2, respectively, and the last term is the Coulomb potential in which r_{12}^{euc} is the Euclidean distance between the two electrons. As mentioned before, from a numerical point of view, it is convenient to apply PBC by defining a supercell with the topology of a Clifford torus because its surface is locally flat everywhere. Therefore, the Laplacian, which is a local operator, is given by the usual expression $\nabla^2 = \sum_{i=1}^{d} \partial_i^2$ with i a Cartesian coordinate.

5.2.1 Exact diagonalization

We solve the time-independent Schrödinger equation involving the Hamiltonian in Eq. (8.18) by employing an exact-diagonalization approach. Therefore, we project the Hamiltonian onto the basis of 2-electron Slater determinants and diagonalize the resulting Hamiltonian matrix to obtain the wave functions and eigenenergies. In the remainder of this subsection we discuss how we build the 2-electron Slater determinants from a symmetry-adapted basis set. This allows us to perform the calculations in a numerically efficient manner such that we can accurately describe the Wigner localization by employing a large number of basis functions.

5.2.1.1 The basis set

Since we want to describe a localization effect of the electrons it is convenient to use a localized basis set instead of a delocalized one, e.g., plane waves. As mention before, the localized Gaussian-type orbitals are convenient in practice because of the Gaussian product theorem [37]. These are the main reasons why we choose Gaussian functions as a primitive basis set to study Wigner localization.

As already introduced in Chapter 3, we use m^d three-dimensional s-type GTO's that are evenly distributed on a regular d-dimensional grid with m the number of Gaussians placed along each side of the Clifford supercell. Moreover, we choose all Gaussians to have a common exponent. The normalized three-dimensional s-type Gaussians functions are defined as

$$g_{\boldsymbol{\mu}}(\mathbf{r}-\mathbf{R}_{\boldsymbol{\mu}}) = \left(\frac{2\alpha}{\pi}\right)^{\frac{3}{4}} e^{-\alpha|\mathbf{r}-\mathbf{R}_{\boldsymbol{\mu}}|^2}, \tag{5.2}$$

where α is the exponent of the Gaussian and $\mathbf{R}_{\boldsymbol{\mu}}$ is the center of the Gaussian $\boldsymbol{\mu}$. For convenience the Gaussians are labeled with a vector $\boldsymbol{\mu}$ containing d integers, one for each dimension of the system. We note that we use the three-dimensional Gaussians also in the case of one- and two-dimensional systems. Therefore, the one- and two-dimensional systems studied in this work are in fact quasi-1- and quasi-2-dimensional systems.

Since the electrons are confined to the Clifford torus also the basis functions that form the electronic wave function have to be confined to the Clifford torus. As a consequence, as already discussed in Chapter 3, the Gaussian product rule given in Eq. (3.7) has to be applied using the geodesic distance.Al already mention before, It is clear that the accuracy of the numerical results will depend on the overlap between two nearest-neighbor Gaussians. If the overlap is too small the basis set will not be able to correctly describe the electronic wave function while if it is too large, i.e., close to 1, a quasi-linear dependence of the basis functions might lead to numerical problems. Since all Gaussians have the same exponent α the nearest-neighbor overlap is simply given by $e^{-\xi/2}$ in which $\xi = \alpha\delta^2$ with δ the distance between two nearest-neighbor Gaussians. We have analyzed this issue in much detail in chapter 3. For this study, the parameter ξ has been set to 0.8.

As a consequence of the periodicity of the Clifford supercell, the system is translationally invariant. Therefore, the translation operator, $\hat{T}_R$, commutes with the Hamiltonian, $\hat{H}$, and the eigenstates of $\hat{H}$ can be chosen to be equal to the eigenstates of $\hat{T}_R$. It is hence convenient to construct symmetry-adapted orbitals (SAO) from a linear combination of GTO's that satisfy the translational invariance. [62]. The (unnormalized) SAO are given in Eq. (3.24). We repeat them here for convenience

$$\phi_{\mathbf{k}}(\mathbf{r}) = \frac{1}{m^{d/2}} \sum_{\boldsymbol{\mu}} e^{i\frac{2\pi}{m}\mathbf{k}\cdot\boldsymbol{\mu}} g_{\boldsymbol{\mu}}(\mathbf{r} - \mathbf{R}_{\boldsymbol{\mu}}), \tag{5.3}$$

where $\mathbf{k} = (k_1, \cdots, k_d)^T$ with $k_i = 0, \cdots, m-1$. and all the μ are inside the Clifford super-cell (CSC).

The one- and two-electron integrals in the symmetry-adapted basis are given by, Eqs. (3.25) and (3.26) respectively and repeated here for convenience.

$$T_{\mathbf{k},\mathbf{k}'} = \delta_{\mathbf{k},\mathbf{k}'} \mathcal{S}_{\mathbf{k}}^{-1} \sum_{\boldsymbol{\nu}} \cos\left[\frac{2\pi}{m}(\mathbf{k}\cdot\boldsymbol{\nu})\right] T_{\mathbf{0},\boldsymbol{\nu}}, \tag{5.4}$$

$$\langle \mathbf{k}, \mathbf{k}' | \mathbf{k}'', \mathbf{k}''' \rangle = \frac{1}{m^d} \delta_{\mathbf{k}+\mathbf{k}'-\mathbf{k}''-\mathbf{k}'''} [\mathcal{S}_{\mathbf{k}} \mathcal{S}_{\mathbf{k}'} \mathcal{S}_{\mathbf{k}''} \mathcal{S}_{\mathbf{k}'''}]^{-1/2}$$

$$\times \sum_{\boldsymbol{\nu}\boldsymbol{\rho}\boldsymbol{\sigma}} \cos\left[\frac{2\pi}{m}(\mathbf{k}'\cdot\boldsymbol{\nu} - \mathbf{k}''\cdot\boldsymbol{\rho} - \mathbf{k}'''\cdot\boldsymbol{\sigma})\right] \langle \mathbf{0}, \boldsymbol{\nu} | \boldsymbol{\rho}, \boldsymbol{\sigma} \rangle, \tag{5.5}$$

With the above integrals we can now express the Hamiltonian in the basis of the Slater determinants $\Phi_{\mathbf{k},\mathbf{k}'} = |\phi_{\mathbf{k}}\bar{\phi}_{\mathbf{k}'}\rangle$. Owing to the Slater-Condon rules these matrix elements can be split in three different cases [55].

Case 1: The two Slater determinants in the matrix element of the Hamiltonian are identical

$$\langle\Phi_{\mathbf{k},\mathbf{k}'}|\hat{H}|\Phi_{\mathbf{k},\mathbf{k}'}\rangle = T_{\mathbf{k},\mathbf{k}} + T_{\mathbf{K}-\mathbf{k},\mathbf{K}-\mathbf{k}} + \langle\mathbf{k},\mathbf{K}-\mathbf{k}|\mathbf{k},\mathbf{K}-\mathbf{k}\rangle \tag{5.6}$$

where we defined $\mathbf{K} = \mathbf{k} + \mathbf{k}'$.

Case 2: The two Slater determinants differ by one spinorbital, i.e., $\mathbf{k} \neq \mathbf{k}''$,

$$\langle\Phi_{\mathbf{k},\mathbf{k}'}|\hat{H}|\Phi_{\mathbf{k}'',\mathbf{k}'}\rangle = T_{\mathbf{k},\mathbf{k}''} + \langle\mathbf{k},\mathbf{k}'|\mathbf{k}'',\mathbf{k}'\rangle = 0 \tag{5.7}$$

where in the last step we used Eqs. (3.25) and (3.26). Similarly we have that $\langle\Phi_{\mathbf{k},\mathbf{k}'}|\hat{H}|\Phi_{\mathbf{k},\mathbf{k}''}\rangle = 0$ for $\mathbf{k}' \neq \mathbf{k}''$.

Case 3: The two Slater determinants differ by two spinorbitals, i.e., $\mathbf{k} \neq \mathbf{k}' \neq \mathbf{k}'' \neq \mathbf{k}'''$,

$$\langle\Phi_{\mathbf{k},\mathbf{k}'}|\hat{H}|\Phi_{\mathbf{k}'',\mathbf{k}'''}\rangle = \langle\mathbf{k},\mathbf{k}'|\mathbf{k}'',\mathbf{k}'''\rangle = \langle\mathbf{k},\mathbf{K}-\mathbf{k}|\mathbf{k}'',\mathbf{K}-\mathbf{k}''\rangle \tag{5.8}$$

since $\mathbf{K} = \mathbf{k} + \mathbf{k}' = \mathbf{k}'' + \mathbf{k}'''$ due to the Kronecker delta that appears on the right-hand side of Eq. (3.26).

From the above considerations we observe that two Slater determinants with different $\mathbf{K}$ do not contribute to the same wave function. As a consequence the resulting Hamiltonian matrix is block diagonal with a block for each $\mathbf{K}$. We can therefore distinguish the solutions of the Schrödinger equation by the different values of $\mathbf{K}$ and we can write the wave functions according to

$$\Psi_{\boldsymbol{K}}(\mathbf{r}_1,\mathbf{r}_2) = \frac{1}{\sqrt{2}}\sum_{\boldsymbol{k}} C_{\boldsymbol{k},\boldsymbol{K}-\boldsymbol{k}}\left[\phi_{\boldsymbol{k}}(\mathbf{r}_1)\bar{\phi}_{\boldsymbol{K}-\boldsymbol{k}}(\mathbf{r}_2) - \phi_{\boldsymbol{k}}(\mathbf{r}_2)\bar{\phi}_{\boldsymbol{K}-\boldsymbol{k}}(\mathbf{r}_1)\right] \tag{5.9}$$

where $\phi_{\mathbf{k}}(\mathbf{r}$ and $\bar{\phi}(\mathbf{r}$ are the α and β spin-orbitals respectively. $C_{\mathbf{k},\boldsymbol{K}-\mathbf{k}}$ are coefficients that are obtained from the diagonalization of the Hamiltonian matrix. We note that the factor $2\pi\mathbf{k}/m$ can be interpreted as a quasimomentum that is conserved. Therefore, $2\pi\mathbf{K}/m$ can be interpreted as the total quasimomentum, which is also conserved. The eigenenergies corresponding to the various $\mathbf{K}$ blocks of the Hamiltonian hence only differ in the kinetic energy of the center of mass of the system. In the following we can, therefore, focus exclusively on the block $\mathbf{K} = \mathbf{0}$ without loss of generality and we define $\Psi(\mathbf{r}_1,\mathbf{r}_2) = \Psi_{\mathbf{K}=\mathbf{0}}(\mathbf{r}_1,\mathbf{r}_2)$.

5.2.1.2 Spin adaptation

For a two-electron system, the electronic wavefunction can correspond either to a spin singlet or to a spin triplet. In the limit of vanishing density the singlet and triplet states become degenerate. Therefore, at very low density both states can become quasi-degenerate. This could yield wave functions that are mixtures of the two states due to round-off errors in the numerical calculation. As a consequence the computed wave functions would not be eigenfunctions of $\hat{S}^2$. To avoid such problems, we performed a spin adaptation of the wave function.

In the case of two electrons an antisymmetrized wave function can either have a symmetric spin component (singlets) or an antisymmetric spin component (triplets). Therefore, the symmetric and anti-symmetric combinations ($\mathbf{K} = \mathbf{0}$) are given by, respectively,

$$\Phi^S_{\mathbf{k},-\mathbf{k}} = \frac{1}{\sqrt{2}}\Big[|\phi_{\mathbf{k}}(\mathbf{r_1})\bar{\phi}_{-\mathbf{k}}(\mathbf{r_2})\rangle + |\bar{\phi}_{-\mathbf{k}}(\mathbf{r_1})\phi_{\mathbf{k}}(\mathbf{r_2})\rangle\Big] \tag{5.10}$$

$$\Phi^T_{\mathbf{k},-\mathbf{k}} = \frac{1}{\sqrt{2}}\Big[|\phi_{\mathbf{k}}(\mathbf{r_1})\bar{\phi}_{-\mathbf{k}}(\mathbf{r_2})\rangle - |\bar{\phi}_{-\mathbf{k}}(\mathbf{r_1})\phi_{\mathbf{k}}(\mathbf{r_2})\rangle\Big] \tag{5.11}$$

The singlet and triplet wave functions are orthogonal and can, therefore, be calculated separately, thus completely avoiding any possibility of finding mixed-state solutions.

5.2.2 2-RDM

Since we are considering a floating Wigner system the one-body density is constant in the Clifford supercell and, therefore, not appropriate to characterize the Wigner localization. We note that there also exists pinned Wigner systems in which the wave function has a broken symmetry. [68] For such systems the one-body density is sufficient to show the Wigner localization. Instead, to demonstrate the Wigner localization at low electron density, as already done in Chapter 4, we calculate the diagonal elements of the two-body reduced-density matrix (2-RDM) since for a given position of one electron it expresses the probability of finding the other electron as a function of its position. In general, the 2-RDM is defined as

$$\begin{gathered}\Gamma^{(2)}(\mathbf{r}_1,\mathbf{r}_2;\mathbf{r}'_1,\mathbf{r}'_2) = \frac{(N-1)N}{2}\times \\ \int \Psi^*_N(\mathbf{r'}_1,\mathbf{r'}_2,\mathbf{r}_3,\cdots,\mathbf{r}_N)\Psi_N(\mathbf{r}_1,\cdots,\mathbf{r}_N)d\mathbf{r}_3\cdots d\mathbf{r}_N\end{gathered} \tag{5.12}$$

in which Ψ_N is an N-body wave function.

For two electrons in the Clifford supercell the diagonal elements of the 2-RDM, i.e., $\Gamma(\mathbf{r}_1, \mathbf{r}_2) = \Gamma^{(2)}(\mathbf{r}_1, \mathbf{r}_2; \mathbf{r}_1, \mathbf{r}_2)$, are given by

$$\Gamma(\mathbf{r}_1, \mathbf{r}_2) = |\Psi(\mathbf{r}_1, \mathbf{r}_2)|^2 \tag{5.13}$$

where Ψ is the two-electron wave function defined in Eq. (5.9) (for $\mathbf{K} = \mathbf{0}$). It is useful to express Γ in the Gaussian basis set according to

$$\Gamma_{\boldsymbol{\mu},\boldsymbol{\nu}} = \iint g_{\boldsymbol{\mu}}(\mathbf{r}_1) g_{\boldsymbol{\nu}}(\mathbf{r}_2) \Gamma(\mathbf{r}_1, \mathbf{r}_2) d\mathbf{r}_1 d\mathbf{r}_2, \tag{5.14}$$

since it describes the probability of the presence of an electron inside the Gaussian $g_{\boldsymbol{\nu}}$ when the other electron is inside the Gaussian $g_{\boldsymbol{\mu}}$.

5.2.3 Semi-classical model

To validate our approach we will compare our results to those obtained with a semi-classical model that tends to the exact solution in the limit of vanishing density, i.e., in the strong-interaction limit. In this limit we can Taylor expand the Coulomb potential in the Hamiltonian of Eq. (8.18) around the equilibrium positions $\mathbf{R}_1$ and $\mathbf{R}_2$ of the two localized electrons in a classical Wigner system according to

$$\hat{H} = \underbrace{-\frac{1}{2}\sum_{i=1,2} \nabla^2_{\mathbf{r}_i} + \hat{U}_0 + \hat{U}_2}_{\hat{H}_0} + \hat{U}_3 + \hat{U}_4 + \cdots \tag{5.15}$$

in which

$$\hat{U}_0 = \frac{1}{R_{12}} \tag{5.16}$$

$$\hat{U}_2 = \frac{1}{2}\sum_{ij}\sum_{\alpha\beta} \partial_{i\alpha}\partial_{j\beta}\frac{1}{r_{ij}}\bigg|_{\mathbf{r}_x=\mathbf{R}_x\forall x} \times (r_{i,\alpha} - R_{i,\alpha})(r_{j,\beta} - R_{j,\beta}), \tag{5.17}$$

where the greek letters α and β denote Cartesian components. Therefore, the Hamiltonian $\hat{H}_0$ contains both the classical Coulomb interaction and a harmonic correction due to the zero-point motion while $\hat{U}_n$ $(n > 3)$ are anharmonic corrections that contain n-th order derivatives of the Coulomb potential. We note that the first-order term in the Taylor expansion, $\hat{U}_1$, vanishes because with the electrons at their equilibrium positions the energy is at a minimum.

The energy $\hat{U}_0$ is the classical energy of two electrons located at their equilibrium positions. In the strong interaction limit the two electrons will be as far apart as possible in the d-dimensional Clifford supercell. Therefore R_{12} attains its maximum value of $L\sqrt{d}/\pi$ and U_0 becomes

$$\hat{U}_0 = \frac{\pi}{L\sqrt{d}}. \tag{5.18}$$

The remainder of $\hat{H}_0$ represents the zero-point correction to the classical energy U_0 in the harmonic approximation. Using a normal-mode transformation one can show that it is equivalent to the Hamiltonian of a quantum harmonic oscillator with the following harmonic frequency [90]

$$\omega = \sqrt{\frac{2\pi^3}{(dL^2)^{\frac{3}{2}}}}. \tag{5.19}$$

Therefore the eigenenergies $E_{\mathbf{n}}$ of $\hat{H}_0$ correspond to

$$E_{\mathbf{n}} = \frac{\pi}{L\sqrt{d}} + \sqrt{\frac{2\pi^3}{(dL^2)^{3/2}}} \sum_{i=1}^{d} \left(n_i + \frac{1}{2}\right), \tag{5.20}$$

in which $\mathbf{n}$ is a vector containing d non-negative integers n_i. The smallest eigenenergy $E_{\mathbf{0}}$ of $\hat{H}_0$ can thus be written as

$$E_{\mathbf{0}} = \frac{\pi}{L\sqrt{d}} + \frac{d}{2}\sqrt{\frac{2\pi^3}{(dL^2)^{3/2}}}. \tag{5.21}$$

The anharmonic corrections to the energy can be calculated using perturbation theory. It can be shown that the zero-order correction to the energy due to $\hat{H}_3$, vanishes. Therefore, the lowest-order correction to the energy consists of U_3^1, i.e., the first-order correction to the energy due to $\hat{U}_3$ and U_4^0, i.e., the zero-order correction to the energy due to $\hat{U}_4$. They are both proportional to L^{-2}. Furthermore, in the case of 2 electrons, one can show that U_3^1 vanishes. Therefore, the lowest-order anharmonic correction for two electrons is entirely due to U_4^0. For the ground state this correction is given by

$$U_4^0 = \langle \Psi_0 | \hat{U}_4 | \Psi_0 \rangle = \frac{(6-d)\pi^2}{16L^2}, \tag{5.22}$$

where the ground-state wave function Ψ_0 is a product of d ground-state wave functions of the quantum harmonic oscillator with the frequency given in Eq. (5.19). The total ground-state energy E_{gs} can thus be written as

$$E_{gs} = \frac{1}{\sqrt{d}}\left(\frac{\pi}{L}\right) + \frac{d^{1/4}}{\sqrt{2}}\left(\frac{\pi}{L}\right)^{3/2} + \frac{(6-d)}{16}\left(\frac{\pi}{L}\right)^2 + \mathcal{O}(L^{-5/2}). \tag{5.23}$$

Finally, we note that in the 1D case the general expression for U_4^0 including the corrections of the energies of the excited states is given by

$$U_4^0(n) = \frac{1}{16}\left(\frac{5}{2} + 10\left(n + \frac{1}{2}\right)^2\right)\left(\frac{\pi^2}{L^2}\right), \tag{5.24}$$

where n is a non-negative integer.

5.3 Computational Details

As mentioned before, we use a Gaussian basis set in which the (normalized) Gaussians are equally spaced on a regular grid. If we do not impose any approximations the calculations remain numerically feasible up to about 1000 GTO's. This means that in 2D and 3D the number of Gaussians placed along each edge are about 30 and 10, respectively. With 1000 GTO's we can accurately describe systems of the following sizes $L = 10^6$ bohr in 1D, $L = 10^4$ bohr in 2D and $L = 10^3$ bohr in 3D, with L the length of an edge of the CSC. Indeed, for larger values of L the average width of the electron distribution becomes of the same order of magnitude or even smaller than the width of the Gaussians, and our description breaks down.

If we want to describe larger system sizes, we must increase the number of Gaussians. As already mention in Chapter 3, in order to do this, we can apply a controlled approximation that is related to the fact that many of the two electron integrals given in Eq. (3.26) are so small that they can be neglected without changing the results. In fact, only those two-electron integrals for which the Gaussian center $\boldsymbol{\rho}$ is close to the center $\mathbf{0}$ *and* the Gaussian center $\boldsymbol{\sigma}$ is close to the center $\boldsymbol{\nu}$ will have non-negligible contributions to the final results. Therefore, in practice, we will only include the two-electron integrals for which $-\lambda \leq \rho_i \leq \lambda$ *and* $-\lambda \leq \sigma_i - \nu_i \leq \lambda$ for all $i = x, y, z$. After numerical investigations, we have chosen $\lambda = 6$ since it leads to relative errors in the energies of 10^{-8} Hartree. This approach allows us to extend the number of basis functions in 2D and 3D to 10000 and 8000 GTO's, respectively, allowing us to describe systems of length $L = 10^6$ bohr in 2D and $L = 10^4$ bohr in 3D. We note that an alternative approach to increase the accuracy could be to extrapolate the results obtained for finite basis sets to the complete basis set limit. [91].

Finally, as mentioned before, due to the 3D nature of the Gaussian orbitals, the one- and two-dimensional systems are in fact quasi-1- and quasi-2-dimensional systems. Therefore, in order to compare our results with those obtained for the pure 1D and 2D systems of the semi-classical model, we have to subtract the contribution to the energy due to the transverse component(s) of the 3D Gaussians. For a 1D and 2D systems, the transverse energy per electron is equal to α and $\frac{\alpha}{2}$ respectively, where α is the exponent of the Gaussian (see Eqs. (3.19)-(3.21)). [92]

5.4 Results

In this section we present the results of our approach. First, we will validate the implementation of our method by comparing its results to those obtained within the semi-classical model. Then we will report the 2-RDM and show that with our approach we can capture the Wigner localization.

5.4.1 Validation

Let us first analyze the energy spectrum of 1D system of various sizes. In Fig. 5.1 we collected the 10 lowest energies for 1D systems of several sizes obtained from our *ab initio* calculations and from the semi-classical model. As expected, there are important differences between the energy spectra obtained with both methods when L is small, since for small L (high density) the semi-classical model, which is based on an asymptotic expansion around $L \to \infty$, is not appropriate. Instead, for large L the agreement between the energy spectra obtained with the model and with the *ab initio* calculations is excellent. When the system size gets larger, the difference between the numerical results and those obtained with the model gets smaller since contributions beyond the first anharmonic corrections fall off at least as $L^{-5/2}$.

Finally, we see from Fig. 5.1 that for a given value of L the difference between the *ab initio* and model energies increases with the level of the excited state n. This is in agreement with the expressions given in Eqs. (5.20) and (5.24) which suggest that a term of order $L^{-p/2}$ is proportional to n^{p-2} with $p \geq 2$ an integer. In other words, the higher the excited state becomes, the more important the higher-order anharmonic corrections that are not included in the model become.

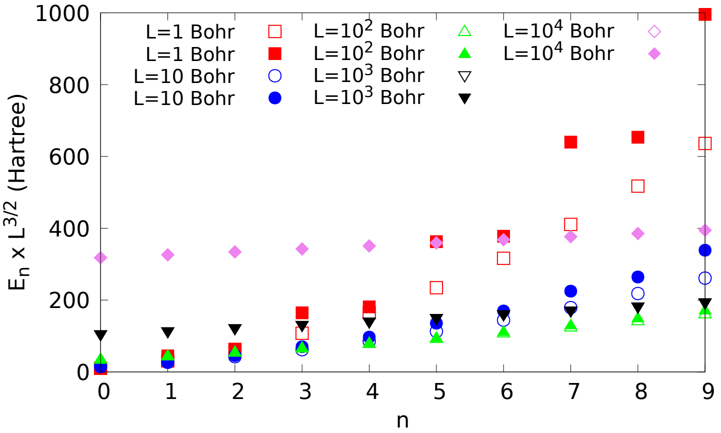

Figure 5.1: Scaled energies ($E_n \times L^{3/2}$) of the 10 first energy levels ($0 \geq n \geq 9$) for 1-dimensional CSC of various sizes. Open symbols: semi-classical model for the the low-density regime; filled symbols: exact diagonalization of the Hamiltonian. When the open symbols are not visible it means that the results obtained with the model and the exact diagonalization completely overlap.

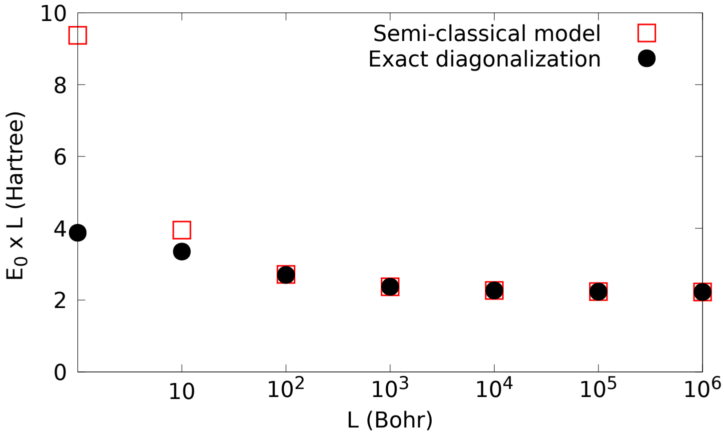

Figure 5.2: Scaled ground-state energies ($E_0 \times L$) for 2-dimensional CSC of various sizes. Open symbols: semi-classical model for the the low-density regime; filled symbols: exact diagonalization of the Hamiltonian.

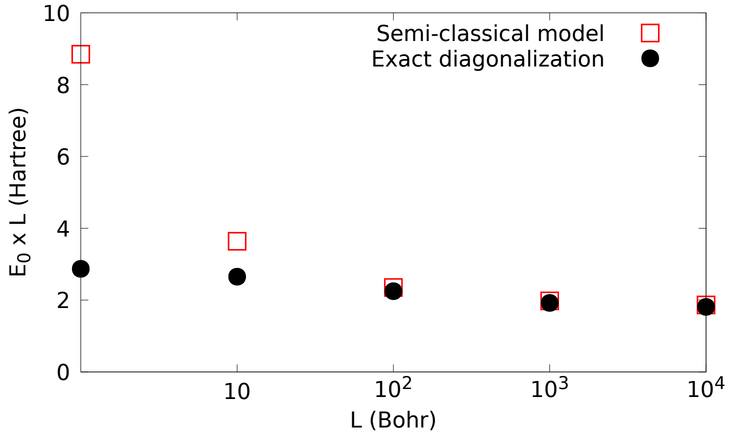

Figure 5.3: Scaled ground-state energies ($E_0 \times L$) for 3-dimensional CSC of various sizes.Open symbols: exact diagonalization of the Hamiltonian; filled symbols: semi-classical model for the the low-density regime.

In 2D and 3D, only the ground-state energy obtained with our *ab initio* approach can be unambiguously identified with that of the semi-classical model but not the excited states because there are many excited states that are degenerate in the model but not in the *ab initio* calculations. Therefore, in the following we will focus our comparison on the ground state only. In Figs. 5.2 and 5.3 we collected the ground-state energies of systems of various sizes for 2- and 3- dimensional systems, respectively. We observe a similar trend as for the 1D case, i.e., important differences between the model and the numerical calculations for small L and an increasingly good agreement between the two methods for larger L. We can conclude that our *ab initio* approach can accurately describe the energies in the low-density regime in 1D, 2D and 3D.

Finally, in table 5.1 we compare our results for the 2D Clifford torus to those obtained in which the ground-state energies of two electrons are confined on a sphere (2-S) of radius R [93]. In the limit $R \to \infty$ the electrons will localize on opposite sides of the sphere and the ground-state energy will tend to $1/(2R)$. Since for the 2D Clifford torus the ground-state energy tends to $\pi/(\sqrt{2}L)$ in the limit $R \to \infty$ we expect that when $L = \sqrt{2}\pi R$ the ground-state energies of the two systems tend to the same value. We have verified numerically that this is indeed the case. We note that the conditions $L = \sqrt{2}\pi R$ implies that the sphere and the Clifford torus have different densities.

R (Bohr)	$E_{2\text{-}S}$ (a.u.) [93]	L (Bohr)	$E_{2\text{-}CT}$ (a.u.)	Relative error (%)
0.0001	9999.772600490	0.000444288	9156.286537170	-9.21
0.001	999.772706409	0.004442882	901.649971604	-10.88
0.01	99.773761078	0.044428829	89.901469264	-10.98
0.1	9.783873673	0.444288293	8.869745989	-10.31
1	0.852781065	4.442882938	0.808037643	-5.54
10	0.064525123	44.42882938	0.065422728	1.37
100	0.005487412	444.2882938	0.00550957	0.40
1000	0.000515686	4442.882938	0.000515936	0.05

Table 5.1: Comparison of the ground-state energies of Spherium (2-Sphere) and the 2D Clifford torus (2-CT) for various system sizes.

5.4.2 Wigner localization

As explained in section 5.2 the Wigner localization can be characterized by $\Gamma_{\mu,\nu}$ which is the (diagonal of) the 2-RDM expressed in the basis of the Gaussian orbitals because it describes the probability of finding an electron contained in Gaussian g_μ when another electron is confined to Gaussian g_ν. In Fig. 5.4 we report the ground-state $\Gamma_{0,\nu}$ as a function of ν for a one-dimensional CSC, i.e. one electron is kept fixed in the gaussian located at the origin. We see that in the high-density region (small L) $\Gamma_{0,\nu}$ is slowly varying. This is because in this regime the kinetic contribution to the energy dominates the electronic repulsion. Therefore the electrons are delocalized and behave as in a free-electron gas. Instead, in the low-density regime (large L), where the electronic repulsion dominates the kinetic energy, $\Gamma_{0,\nu}$ is peaked being non-negligible only in a small region of space. This clearly indicates the Wigner localization of the electrons. Not surprisingly, the position having the highest probability to find the second electron is at $L/2$ which equals the largest possible distance between two electrons in 1D.

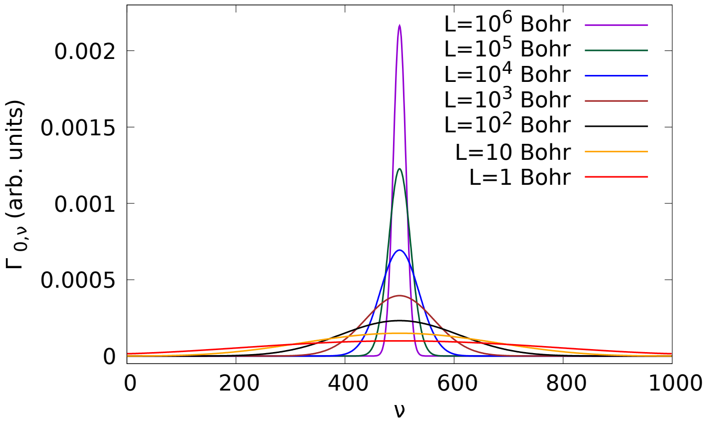

Figure 5.4: $\Gamma_{0,\nu}$ as a function of ν for two electrons on a 1D Clifford torus for various values of the system length L. The position of one electron is fixed around the center of the Gaussian located at the origin ($\nu = 0$). Notice that the first ($\nu = 0$) and the last ($\nu = 1000$) points coincide.

In Figs. 5.5-5.8 we report $\Gamma_{\mathbf{0},\boldsymbol{\nu}}$ of a square 2-dimensional CSC for $L = 1$, $L = 10^2$, $L = 10^4$, and $L = 10^6$ bohr, respectively. As was the case in 1D, for small values of L the 2D system behaves as a Fermi gas since $\Gamma_{\mathbf{0},\boldsymbol{\nu}}$ is almost constant. Instead, when the system size increases, we can clearly observe the electron localization from the peaked structure of $\Gamma_{\mathbf{0},\boldsymbol{\nu}}$. In 2D the position having the highest probability to find the second electron is in the middle of the square CSC, thus maximizing the distance between the two electrons.

In Figs. 5.9-5.11 we report $\Gamma_{\mathbf{0},\boldsymbol{\nu}}$ of a cubic 3-dimensional CSC for $L = 1$, $L = 10^2$, and $L = 10^4$ bohr, respectively. We note that $\Gamma_{\mathbf{0},\boldsymbol{\nu}}$ is represented by a color gradient, from blue (small) to red (large). We ask the reader to pay attention to the fact that there are significant differences in the scale for

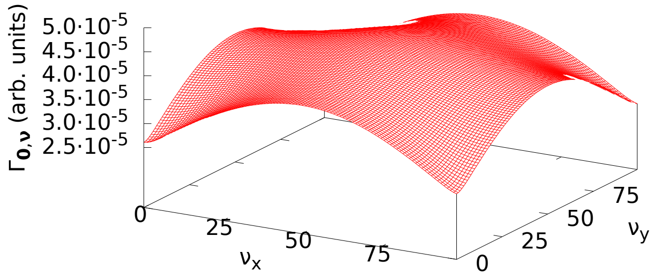

Figure 5.5: $\Gamma_{\mathbf{0},\boldsymbol{\nu}}$ as a function of $\boldsymbol{\nu}$ for two electrons in a square 2-dimensional Clifford supercell with an edge of length $L = 1$ bohr. The position of one electron is fixed at the origin $\boldsymbol{\nu} = \mathbf{0}$.

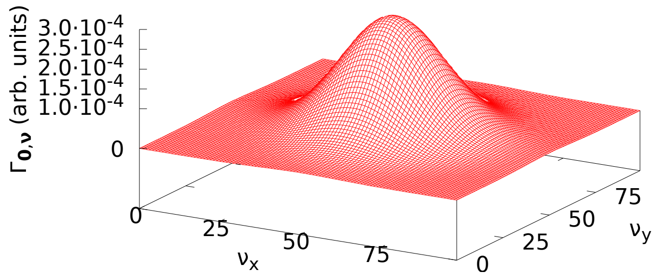

Figure 5.6: $\Gamma_{\mathbf{0},\boldsymbol{\nu}}$ as a function of $\boldsymbol{\nu}$ for two electrons in a square 2-dimensional Clifford supercell with an edge of length $L = 100$ bohr. The position of one electron is fixed at the origin $\boldsymbol{\nu} = \mathbf{0}$.

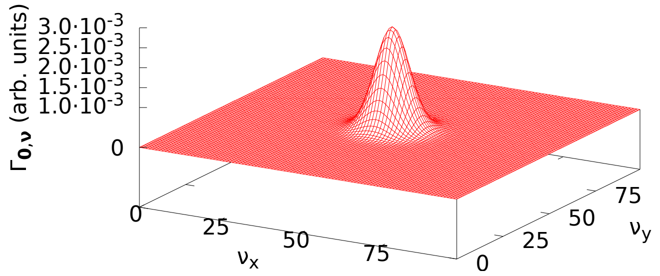

Figure 5.7: $\Gamma_{\mathbf{0},\boldsymbol{\nu}}$ as a function of $\boldsymbol{\nu}$ for two electrons in a square 2-dimensional Clifford supercell with an edge of length $L = 10^4$ bohr. The position of one electron is fixed at the origin $\boldsymbol{\nu} = \mathbf{0}$.

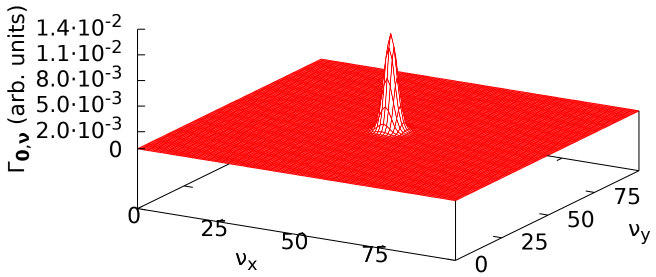

Figure 5.8: $\Gamma_{\mathbf{0},\boldsymbol{\nu}}$ as a function of $\boldsymbol{\nu}$ for two electrons in a square 2-dimensional Clifford supercell with an edge of length $L = 10^6$ bohr. The position of one electron is fixed at the origin $\boldsymbol{\nu} = \mathbf{0}$.

the various figures. Taking this into account we see once more that for small L we have an almost constant $\Gamma_{\mathbf{0},\boldsymbol{\nu}}$ while for large L we observe that $\Gamma_{\mathbf{0},\boldsymbol{\nu}}$ is localized in the middle of the cubic CSC, which is the furthest point from the other electron located at the origin.

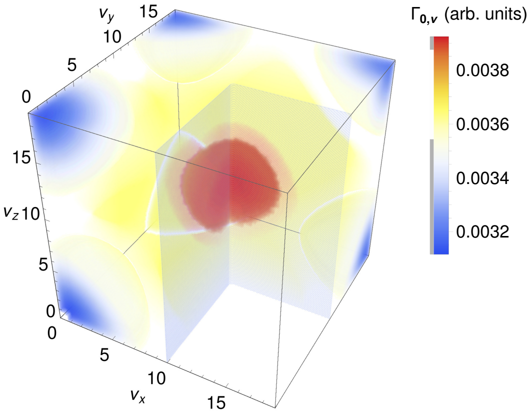

Figure 5.9: $\Gamma_{\mathbf{0},\boldsymbol{\nu}}$ as a function of $\boldsymbol{\nu}$ for two electrons in a cubic 3-dimensional Clifford supercell with an edge of length $L = 1$ bohr. The position of one electron is fixed at the origin $\boldsymbol{\nu} = \mathbf{0}$.

In order to compare the localization in the different dimensions we compare $\Gamma_{0,\nu}$ corresponding to the one-dimensional CSC with the diagonal elements of $\Gamma_{\mathbf{0},\boldsymbol{\nu}}$ for the two- and three-dimensial CSCs. In Fig. 5.12 we report this comparison for $L = 10$ bohr. We observe that the amount of localization is inversely proportional to the number of dimensions of the system, i.e., the

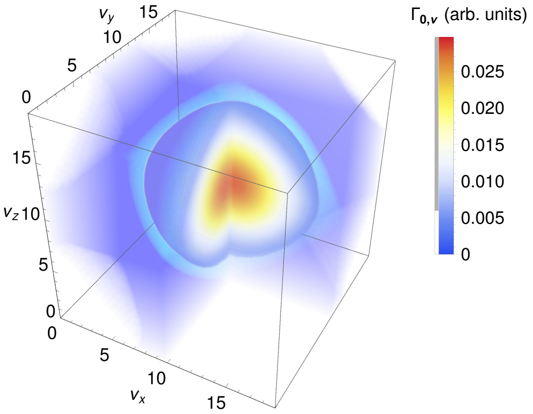

Figure 5.10: $\Gamma_{\mathbf{0},\boldsymbol{\nu}}$ as a function of $\boldsymbol{\nu}$ for two electrons in a cubic 3-dimensional Clifford supercell with an edge of length $L = 100$ bohr. The position of one electron is fixed at the origin $\boldsymbol{\nu} = \mathbf{0}$.

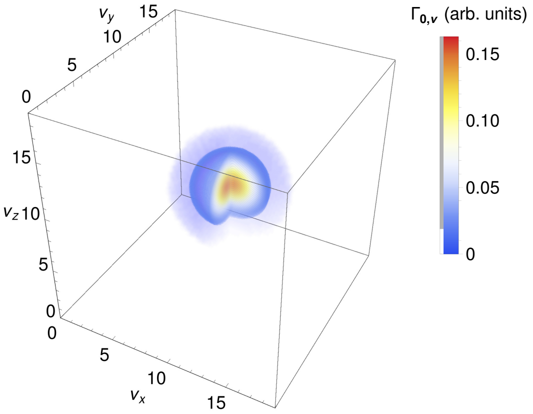

Figure 5.11: $\Gamma_{\mathbf{0},\boldsymbol{\nu}}$ as a function of $\boldsymbol{\nu}$ for two electrons in a cubic 3-dimensional Clifford supercell with an edge of length $L = 10000$ bohr. The position of one electron is fixed at the origin $\boldsymbol{\nu} = \mathbf{0}$.

localization is largest in 1D and smallest in 3D. The reason is that, for fixed L, in higher dimensions the electrons have more space available to avoid each other. We note that this result is consistent with those obtained for the transition of a Fermi liquid to a Wigner crystal in different dimensions. This Wigner-Seitz radius at which this transition occurs is proportional to the number of dimensions [94, 95, 96, 68, 97].

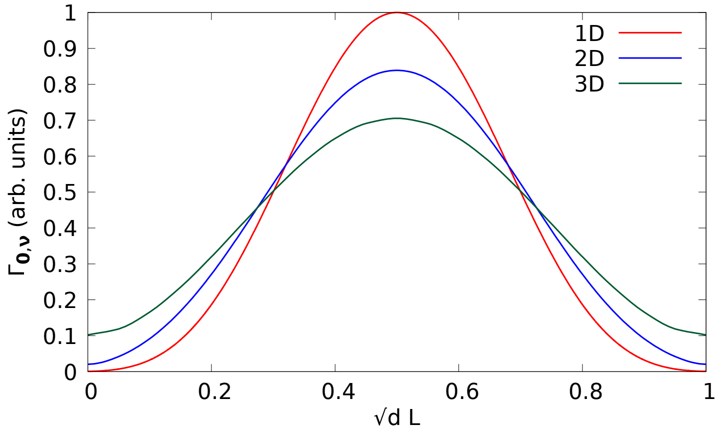

Figure 5.12: The diagonal of $\Gamma_{\mathbf{0},\nu}$ as a function of $\sqrt{d}L$ for systems of different dimensions with $L = 10$ Bohr. The curves have been normalized such that the surface area underneath all three curves are equal.

5.4.3 Natural amplitudes and occupation numbers

Although the one-body reduced density matrix (1-RDM) cannot be used to explicitly visualize the Wigner localization an implicit link can still be made. The eigenvalues of the 1-RDM are the natural occupation numbers and they can be related to the amount of electron correlation in the system [87, 98]. When all occupation numbers are either 0 or 1 the system can be considered uncorrelated and when all the occupation numbers have the same fractional value equal to the number of electrons divided by the number of spinorbitals the system can be considered maximally correlated [10]. In the case of two electrons the natural occupation numbers $n_{\mathbf{k}}$ are equal to $C^2_{\mathbf{k},-\mathbf{k}}$, i.e., the square of the coefficients ($\mathbf{K} = \mathbf{0}$) in Eq. (5.9) [99]. In Fig. 5.13 we report the natural occupation numbers n_k for the 1D Clifford torus as a function of k. As expected, we observe that for small L (weak correlation) two natural spinorbitals, both having an identical spatial part, have an occupation close to 1 and all the other orbitals have an occupation close to 0, while for large L (strong correlation) there are no natural orbitals with an occupation close to 1 and several orbitals with a small but finite occupation number.

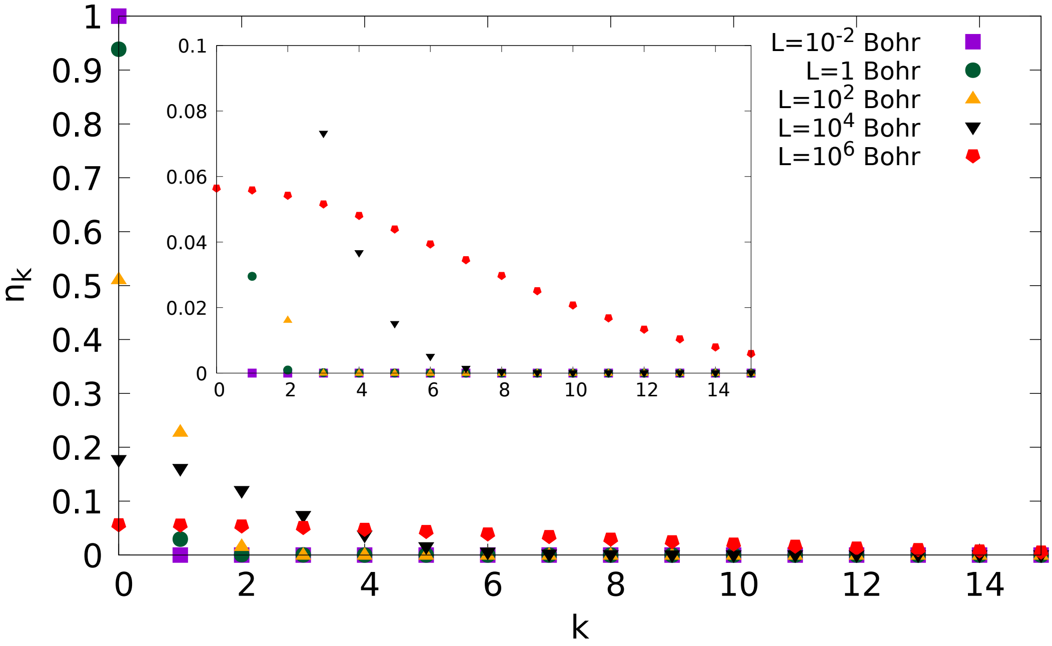

Figure 5.13: The natural occupation numbers n_k as a function of k for 1D Clifford tori of various sizes. We note that the occupation numbers of two spinorbitals having the same spatial part overlap.

It is also interesting to investigate the behavior of the natural amplitudes λ_k, which in our two-electron systems are equal to the coefficients $C_{\mathbf{k},-\mathbf{k}}$. We report these amplitudes as a function of k for the 1D Clifford torus in Fig. 5.14. We notice that for small L (weak correlation) there is a single positive natural amplitude (at $k = 0$), while for large L (strong correlation) the positive and negative amplitudes alternate. Similar trends have previously been observed for the two-electron harmonium atom, which is a model system consisting of two electrons that are confined by a harmonic potential. For large harmonic frequencies (weak correlation) the harmonium atom has one positive natural amplitude while for small frequencies (strong correlation) there is an alternation of the positive and negative amplitudes [100]. We defer the investigation of interesting related properties, such as the existence of solitonic natural orbitals and a possible power-law dependence of the decay of the occupation numbers as a function of k to future studies [101, 102].

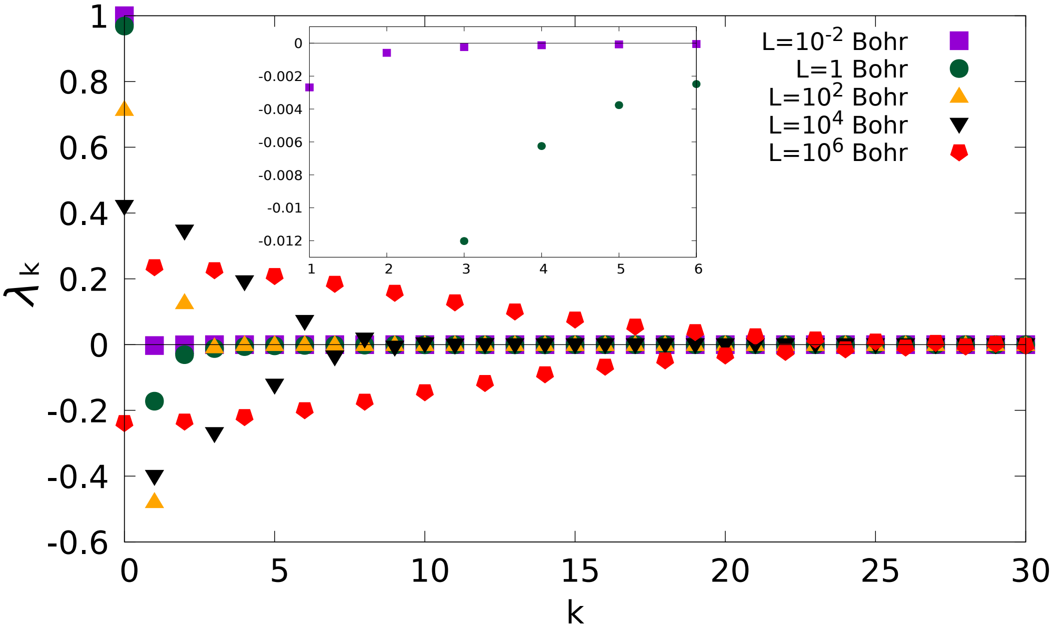

Figure 5.14: The natural amplitudes λ_k as a function of k for 1D Clifford tori of various sizes. We note that the amplitudes of two spinorbitals having the same spatial part overlap.

5.5 Conclusions

We have presented an accurate and numerically efficient approach to study Wigner localization in systems of various dimensions (1D, 2D, 3D). Its main features are: 1) the application of Clifford periodic boundary conditions with a renormalized distance to describe the Coulomb potential and 2) the use of gaussian basis functions that are placed on a regular grid inside a Clifford supercell. We have validated our method by comparing its results to those obtained within a semi-classical model that becomes exact in the limit of vanishing density. Finally, using the two-body reduced density matrix, we have demonstrated that our approach can accurately capture the Wigner localization.

Our approach paves the way for several interesting future developments: 1) the generalization of our approach to more than 2 electrons in order to study many-electron Wigner systems and, eventually, Wigner crystals. 2) the implementation of our approach in Hartree-Fock (HF) theory and post-HF *ab initio* approaches. 3) the inclusion of ions in our approach which will allow the study of the solid state.

In the next chapter we will pursue the further development and study of Wigner systems with more than 2 electrons.

Chapter 6

The emergence of a Wigner crystal in two dimensions

Contents

6.1 Motivation

Most predictions to determine the lattice structure of Wigner crystals, both using classical point charges and electrons, were based on the comparison of the energies for a few known crystals structures [90, 103, 104, 104, 105]. For example, in two dimensions it can be shown that the hexagonal lattice has a lower energy than the square lattice [90, 103]. However, this leaves open the possibility that there might be another, less trivial, lattice structure that has a lower energy than the hexagonal lattice. In this work we make an important step towards the prediction of the lattice structure of Wigner crystals without making any assumptions about the lattice structure. Although the number of electrons in this work is too small to speak of a Wigner crystals we will show that there is a clear emergence of the hexagonal crystal structure in two dimensions.

In the previous chapter we have presented an approach to describe Wigner localisation. It is based on Clifford periodic boundary conditions with a renormalized distance in the Coulomb potential and a regular grid of Gaussian basis functions. We showed that with our approach we can accurately capture the Wigner localisation of two electrons in one, two, and three dimensions.

In this chapter, we will present an extension of our approach to an arbitrary number of electrons in one and two dimensions. Since the calculations in our previous chapters were limited to two electrons we could solve the Schrödinger equation using exact diagonalization. For many electrons, exact diagonalization becomes numerically intractable we have to use an approach that is both accurate but also numerically efficient. As we will demonstrate in the following, we found that restricted open-shell Hartree-Fock (ROHF) is sufficient to accurately capture the localisation of the electrons. Finally, since the few-electron Wigner systems here can be seen as fragments of Wigner crystals, therefore, we will refer to them as Wigner fragments.

To be submitted

6.2 Theory

We follow a similar approximation as in chapter 5 i.e. we consider an electron gas of N electrons confined to a one- or two-dimensional Clifford torus. It is also convenient that the Clifford torus is a finite system because it allows us to use all the standard quantum-chemistry tools that are usually applied to molecules. The only modification that is required is the introduction of a modified distance in the Coulomb potential as discussed in chapter 3. Finally, the fact that the system is closed means that the system has translational symmetry which can be exploited to reduce the numerical cost of the calculations.

A Clifford torus containing only electrons would have full translational invariance. Therefore, at low density, this would lead to a floating Wigner fragments, i.e., a system in which the electrons will be localised but without having any preferred positions in space [68]. As a consequence, the one-body density will be constant in the Clifford torus and it is difficult to observe the electron localisation although it can be done with reduced density matrices [10]. Instead, in this chapter we will study pinned Wigner fragments by introducing a tiny perturbation that will lead the electrons to collapse to precise positions in space. The localisation of the electrons in the pinned Wigner fragment can then be easily observed thanks to the one-body density. As a perturbation we will use a small fractional positive charge q. Therefore, the Hamiltonian of the Wigner fragments we will study is given by

$$\hat{H} = -\frac{1}{2}\sum_{i=1}^{N}\nabla_i^2 - \sum_{i=1}^{N}\frac{q}{r_{iq}^{euc}} + \sum_{i=1}^{N}\sum_{j>i}^{N}\frac{1}{r_{\mu\nu}^{euc}} \tag{6.1}$$

Where the first term on the right-hand side is the operator for the kinetic energy of the electrons, the second term is the Coulomb attraction between the electrons and the small positive charge q, and the last term is the Coulomb repulsion between the electrons. The Coulomb potentials are defined in terms of the Euclidean distance $r_{\mu\nu}^{euc}$ which is the distance between electrons μ and ν

in the embedding space of the Clifford torus as defined in Eq. (2.9). Instead, whenever the Gaussian product rule is applied, we we have to use the geodesic distance defined in Eq. (2.5). For simplicity we have chosen all the edges of the CSC to be of equal length although some preliminary results on rectangular CSC will be presented at the end of the chapter. As discussed in more detail in chapter 2, the advantage of using the Euclidean distance in the Coulomb potential instead of the geodesic distance is because the derivative of the geodesic distance with respect to the position has a discontinuity. Instead, the first and higher order derivatives of the Euclidean distance are continuous everywhere.

We will use a Gaussian basis set to perform our numerical calculations. A Gaussian basis set is convenient because: 1) we are studying electron localisation and a localised basis is therefore suited to describe this phenomenon; 2) Gaussian basis sets are implemented in most quantum-chemistry computer codes because of their numerical simplicity when calculating integrals involving several basis set functions. However, since we are interested in describing a system containing only electrons there are no natural positions in which to center the Gaussian functions. In order to ensure that the wave function is well-described everywhere we use a regular grid of Gaussian functions in the CSC. The normalized Gaussian functions are given by Eq. (3.6). We repeat the equation here for convenience

$$g_\mu(\mathbf{r}-\mathbf{R}_\mu) = \left(\frac{2\alpha}{\pi}\right)^{\frac{3}{4}} e^{-\alpha|\mathbf{r}-\mathbf{R}_\mu|^2} \tag{6.2}$$

where α is the exponent of the gaussian and $\mathbf{R}_\mu$ is the center of gaussian g_μ.

Since at vanishing average density the kinetic energy contribution will become negligible with respect to the Coulomb repulsion, we expect that in this limit the positions at which the electrons localize will be equivalent to the positions for which classical point charges obtain their minimal energy. Therefore, we will compare our results for the equilibrium positions of the electrons obtained at a small but finite average density to those obtained for a CSC with classical point charges. To determine these positions we will minimize the energy of these classical Wigner fragments using the Newton-Raphson method [106]. The total energy of a CSC containing N point charges is given by

$$\begin{aligned} U(r_1, r_2, \ldots, r_N) =& \sum_{i>j}^{N} \frac{1}{r_{ij}^{euc}} = \\ =& \frac{\pi}{L \sum_{i>j}^{N} \sqrt{\sum_{x=1}^{d} \sin^2\left(r_{ij}(x)\frac{\pi}{L}\right)}} \end{aligned} \tag{6.3}$$

In order to be sure we obtain a global minimum, we repeat the Newton-Raphson procedure many times starting from different initial geometries. The set of initial geometries contains both random initial positions as well as positions that are close to the equilibrium positions obtained in the quantum calculations. By comparing the energies obtained from the various minimisations we obtain a lowest energy which we will consider to be the global minimum.

6.3 Computational details

We use a fractional charge of $q = 0.01$ a.u. located in the origin of the coordinate system to obtain a pinned Wigner fragment. The size of the CSC is chosen to be proportional to the number of electrons and the number of dimensions of the system. We use 200 Bohr per electron and per dimension. In the case of one-dimensional Wigner fragments the number of Gaussian basis functions is also proportional to the number of electrons of the system. We use 10 Gaussians per electron. In the case of two dimensional Wigner fragments we fix the number of Gaussians to 400, i.e., 20 Gaussians per dimension. For a fixed number of Gaussian functions the quality of the basis set is defined by α and the nearest-neighbor distance δ. These two parameters can be combined as $\xi = \alpha\delta^2$. In this chapter, as in the previous one, we set $\xi = 0.8$. This ensures a sufficiently large overlap between nearest-neighbour Gaussians, and therefore, a smooth wave function while avoiding numerical instabilities due to quasi-linear dependencies of the basis functions. More details on the basis set can be found in chapter 3 and Ref. [92].

All calculations were performed with a modified version of the Dalton software package [107]. In particular, the overlap, one- and two-electron integrals were modified to make them compatible with the Clifford periodic boundary conditions.

6.4 Results

At low density we expect that the spin configuration of the Wigner fragment will have little effect on the electron localisation. Therefore, we will focus on the high-spin state, i.e., the spin state for which S_z has its maximum value, because, thanks to the Pauli principle, a single Slater determinant will be sufficient to describe the system [108]. This will then allow us to use the numerical efficient restricted open-shell Hartree-Fock (ROHF) approach to accurately describe this system.

Although our main interest in this work are two-dimensional Wigner fragments we will first study one-dimensional systems because it will allow us to compare the ROHF results to those obtained using full configuration interaction (FCI) which yields the exact result for the given basis set. As an example we report in Fig. 6.1 the one-body density in a one-dimensional CSC for 5 electrons. The density profile obtained within FCI clearly shows 5 distinct peaks demonstrating the Wigner localisation. Also in Fig. 6.1 we report the density of the same system but calculated within ROHF. We observe that these results are very similar to those obtained within FCI. Although ROHF slighly overlocalises the electrons, the FCI and ROHF density profiles are equivalent. We have obtained similar results for other 1D Wigner fragments [9]. Therefore, in the following we will study 2D Wigner fragments in their high-spin states within ROHF.

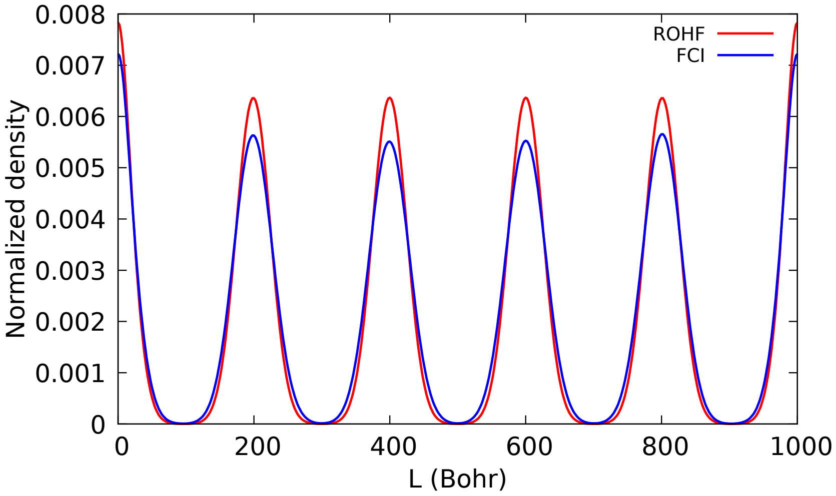

Figure 6.1: The density of five electrons in a one-dimensional CSC. Blue: FCI; red: ROHF.

In the left panel of Fig. 6.2 we show the electron density of a Wigner fragment with three electrons. We observe that the electrons localise on the diagonal of the CSC. The three-electron 2D system thus behaves as a 1D system with length $L = \sqrt{L_x^2 + L_y^2}$. We note that the obtained solution is degenerate with another one in which the electrons localise on the other diagonal of the CSC. In the following, for the sake of simplicity, we will avoid discussing the degenerate solutions we have obtained since the density profiles of all degenerate solutions are equivalent. In the right panel of Fig. 6.2 we show the positions of three classical point charges corresponding to the minimal energy of these charges in the CSC. As expected we observe that positions of the classical point charges correspond to the positions of the electrons. We have done similar calculations for 2D Wigner fragments up to 10 electrons.

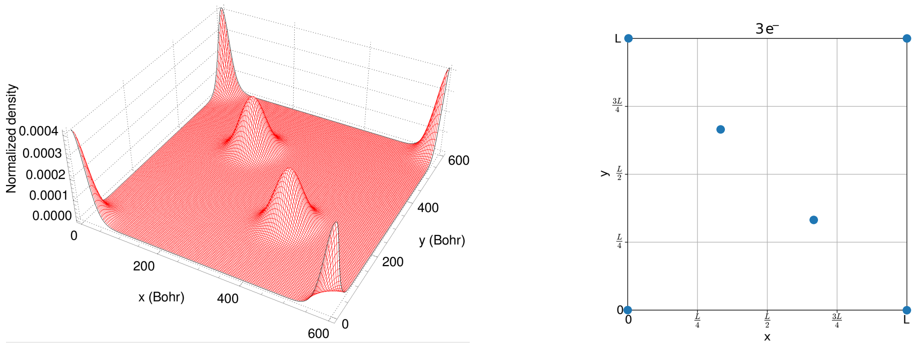

Figure 6.2: Left panel: The ROHF density for three electrons confined to a 2D CSC. Right panel: the classical equilibrium positions for three point charges confined to a 2D CSC.

In the left panel of Fig. 6.3 we report the density for 5 electrons confined to the CSC. We observe that the electrons localise on two parallel lines, with each line joining a vertex with the center of an edge of the CSC. Again the positions of the electrons correspond to those of point charges at their minimum-energy configuration as can be seen in the right panel of Fig. 6.3.

The most interesting localisation pattern occurs for a Wigner fragment with 8 electrons as can be verified in the right panel of Fig. 6.4. We see that the electrons localize in a distorted hexagonal lattice. This result is again confirmed by the positions of the point charges corresponding to their minimal total energy. As mentioned before, the hexagonal lattice is the lattice structure of the 2D Wigner crystal that has the lowest energy when compared with other standard lattices and, in particular, the square lattice. In our case we do not find a perfect hexagonal lattice because we have fixed the lengths of the two edges of the CSC to be equal. If instead, we would choose the ratio of the two edges to be equal to $\sqrt{3}/2$ we expect to find a perfect hexagonal lattice.

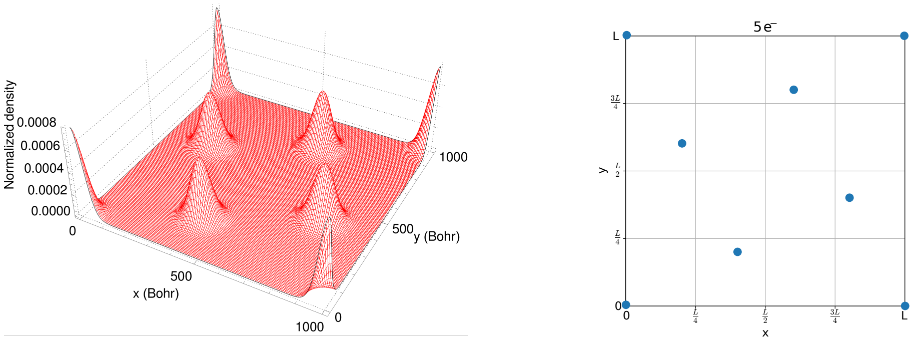

Figure 6.3: Left panel: The ROHF density for five electrons confined to a 2D CSC. Right panel: the classical equilibrium positions for five point charges confined to a 2D CSC.

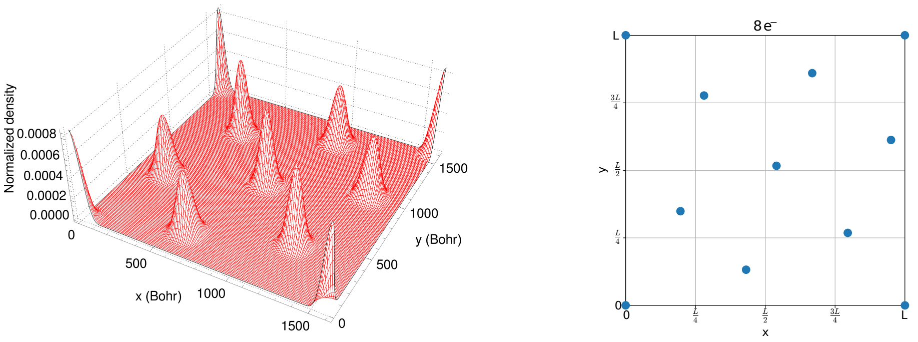

Figure 6.4: Left panel: The ROHF density for eight electrons confined to a 2D CSC. Right panel: the classical equilibrium positions for eight point charges confined to a 2D CSC.

Following this last hypothesis we have performed a calculation with 12 electrons confined to a rectangular CSC with a $\sqrt{3}/2 : 1$ ratio of the two edges which is compatible with a hexagonal structure. We used a basis set consisting of 22 Gaussians in the x direction and 19 in the y directions. The one-density for this Wigner fragment can be found in Fig. 6.5. We observe that the electrons form a slightly stretched hexagonal lattice which seems to indicate the emergence of the hexagonal lattice structure in a uniform two-dimensional electron gas at low density. Work is in progress to increase the number of electrons in the calculations in order to try to find a perfect hexagonal lattice.

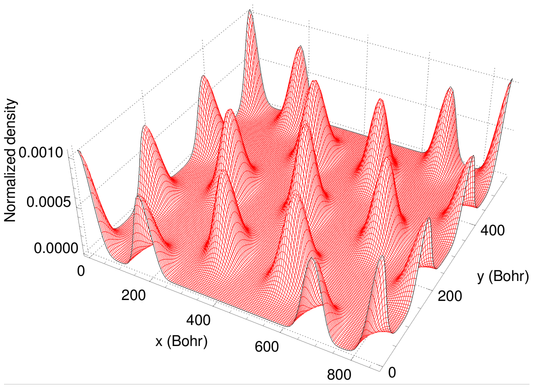

Figure 6.5: The ROHF density for twelve electrons confined to a rectangular CSC.

We note that for rectangular lattices, the expression of $r_{\mu\nu}^{euc}$ given in Eq. (2.9) is not valid since L_x is different to L_y. Thus, a generalization of Eq. (2.9) is given by

$$r_{\mu\nu}^{euc} = \sum_{i=1}^{d} \sqrt{\frac{L_i^2}{\pi^2} \sin^2\left(\frac{\pi r_{\mu\nu}(i)}{L_i}\right)}, \tag{6.4}$$

where i sums over the Cartesian components, L_i is length of the system in the i direction and $r_{\mu\nu}(i)$ is defined in Eq. 2.6.

6.5 Conclusions

In this last chapter, we have proposed an efficient and accurate approach to study Wigner fragments. It is based on the creation of a supercell that has the topology of a Clifford torus together with introduction of a renormalized distance in the Coulomb potential. Moreover, we have shown that the numerically efficient restricted open-shell Hartree-Fock approach is sufficiently accurate to describe the electron localisation in these Wigner fragments thanks to the fact that we can study the high-spin state of these systems. With our approach we clearly see the emergence of the hexagonal lattice structure in 2D Clifford supercells. This result was obtained without making assumptions about the possible lattice structures except for the ratio of the lengths of the two edges. Finally, we have compared our results obtained for electrons at low density to those obtained in a classical model of point charges. We have demonstrate that the positions at which the electrons localize are the same as the positions at which the point charges attain their lowest energy. This equivalence between quantum and classical results could be used to perform calculations on Wigner fragments with much larger number of electrons. It could also be interesting to study the three-dimensional Wigner fragment using the tools presented in this work.

Chapter 7

General conclusions and outlook

This dissertation presented a new approach for treating strongly correlated electrons. The approach consists on two main ideas. First, in Chapter 2, we introduced the use of Clifford boundary conditions. The general strategy of the proposed boundary conditions consists of transforming a large fragment (a supercell) of a periodic system into a Clifford torus, and then redefining the distance between two points by taking the Euclidean distance between these points in the embedding space of the torus. Second, in chapter 3, we described the distributed Gaussian basis set which consists of placing $1s$ orbitals evenly spaced with a common orbital exponent. In chapters 4-6 we presented the results. More precisely, in chapter 4, we will studied two electrons confined to a ring. We saw that at high density, the wave function of the system is similar to the one of a free-electron system. However, by lowering the density, there is a complete change of the wave function structure. The electrons change from a state where they are essentially delocalized, and well described by a single Slater determinant, to a state where they are localized at fixed positions in space. We obtained a deeper insight in the nature of electron localization by studying the localization tensor and the electron entropy. Indeed, by lowering the electron density, we observe a sudden growth of the entropy and a corresponding drop of the position spread in the density regime where the electrons localize. The drop of the position spread indicates a reduced mobility of the electrons with respect to the Fermi-gas solution. This behavior is a signature of Wigner localization. The increase of the electronic entropy also indicates that the low-density state is much more correlated than the Fermi-gas state, which tends to a single determinant (zero correlation) in the limit of very high densities. In chapter 5 we presented an accurate and numerically efficient approach to study Wigner localization in systems of various dimensions (1D, 2D, 3D). Its main features are: 1) the application of Clifford periodic boundary conditions with a renormalized distance to describe the Coulomb potential and 2) the use of Gaussian basis functions that are placed on a regular grid inside a Clifford supercell. We have validated our method by comparing its results to those obtained within a semi-classical model that becomes exact in the limit of vanishing density. Finally, using the two-body reduced density matrix, we have demonstrated that our approach can accurately capture the Wigner localization. Finally, in chapter 6 we have generalized the approach to a homogeneous electron gas with more than 2 electrons at very low densities in 1- and 2-dimensions. We studied several pinned Wigner fragments and clearly observed Wigner localization from the one-body density. We also observed the natural emergence of the hexagonal packing as the most stable configuration. Moreover, we have validated our method by comparing the equilibrium position of the electrons with those obtained by a minimization procedure of the classical energy of a Wigner fragment.

Our approach paves the way for several interesting future developments: (1) The study of 3-dimensional Wigner fragments to verify if the bcc structure emerges as has been predicted. (2) Combine our Clifford approach with Quantum Monte Carlo methods to study Wigner crystals. (3) The extension of the approach to the treatment of solids. (4) The development of a more accurate classical approach by using analytical gradients and the implementation of conjugate gradients for minimizing the energy will allow us to treat, classically, a larger number of electrons.

CHAPTER 8

Résumé en Français

L'objectif de cette thèse est l'étude des systèmes de Wigner. Il y a près d'un siècle, Wigner a prédit qu'un système constitué uniquement d'électrons en interaction dans un fond uniforme neutralisant formerait une structure cristalline à une densité suffisamment faible, les électrons étant localisés sur les sites du réseau [1]. Son argument peut être compris en considérant la dépendance des énergies cinétique et répulsive par rapport au rayon de Wigner-Seitz r_s, qui est le rayon d'une sphère contenant, en moyenne, un électron. Ou plus généralement, la moitié de la distance moyenne entre les électrons les plus proches. Alors que l'énergie cinétique s'échelonne comme r_s^{-2}, l'énergie répulsive s'échelonne comme r_s^{-1}. Par conséquent, dans la limite de faible densité (grand r_s), le hamiltonien est dominé par l'énergie répulsive, ce qui conduit les électrons à se localiser dans l'espace. Lorsque de nombreux électrons sont présents, les électrons se localisent sur des sites cristallographiques, formant ce que l'on appelle un cristal de Wigner. Des cristaux de Wigner unidimensionnels et bidimensionnels ont été observés expérimentalement [2, 3]. De manière générale, on parle de localisation de Wigner lorsque les électrons se localisent en raison de la répulsion électron-électron. Pour les systèmes à quelques électrons, on parle également de molécules de Wigner [4, 5, 6, 7, 8, 9, 10] qui ont également été observées expérimentalement [11].

Le confinement des électrons présente un intérêt technologique de longue date. Il y a plusieurs façons de procéder: nous pourrions confiner les électrons dans un système d-dimensionnel fini avec un fond positif, mais les effets de frontière influenceraient les résultats [9]. Une façon d'éviter les effets de frontière est de confiner les électrons dans un espace fermé de d-dimension tel qu'un d-torus. C'est ce que nous allons C'est ce que nous ferons en une dimension en confinant 2 électrons dans un 1-tore qui qui est équivalent à un anneau. Cependant, pour $d > 1$, la mise en œuvre numérique de la géométrie d'un d-tore est encombrante. Par conséquent, pour $d > 1$, nous appliquons des conditions limites périodiques (PBC). Plus précisément, nous définissons une supercellule régulière de d-dimensions et modifions ensuite sa topologie en une topologie toroïdale en joignant les côtés opposés de la cellule sans déformation [21]. Cette procédure permet d'obtenir une supercellule ayant la topologie d'un tore de d-Clifford. Un tore de Clifford d est un espace euclidien réel fermé, plat, de dimension d, intégré dans un espace euclidien complexe de dimension d. Par exemple, dans ce cadre, un cercle et une ligne sont topologiquement équivalents.

Étant donné que la forte corrélation électronique est à l'origine de la localisation de Wigner, l'étude *ab initio* de ce phénomène nécessite des approches de chimie quantique précises telles que l'interaction de configuration complète (FCI) ou des méthodes multi-configurationnelles telles que le champ autoconsistant de l'espace actif complet afin d'obtenir des énergies et des fonctions d'onde très précises dans les régimes de faible et de forte corrélation [22, 23, 24, 25]. Lors de l'étude de systèmes pilotés par des interactions coulombiennes, comme les systèmes de Wigner, des méthodes corrélées sont nécessaires pour décrire la fonction d'onde avec précision. Les méthodes de la chimie quantique, plus précisément les méthodes post-HF, ajoutent la corrélation des électrons à la solution non corrélée de Hartree-Fock (HF) : [27, 28]. Pour décrire la localisation de Wigner à l'aide des méthodes post-HF disponibles, nous avons formulé des conditions aux limites où le potentiel de Coulomb est traité explicitement, évitant ainsi l'utilisation d'images de réplique.

Pour de nombreux électrons en interaction, nous devons résoudre l'équation de Schrödinger sur l'ensemble de la supercellule. De manière générale, nous pouvons écrire l'hamiltonien à corps multiples comme suit

$$\hat{H} = -\frac{1}{2}\sum_{i=1}^{N}\nabla_i^2 + \sum_{i}^{N}\sum_{j<i}^{N}\frac{1}{|\mathbf{r}_i - \mathbf{r}_i|} \tag{8.1}$$

où N est le nombre d'électrons dans la cellule de simulation.

Dans cette thèse, nous travaillerons avec des espaces euclidiens plats connectés (fermés), comme le montre la Fig 8.1. Pour ce faire, nous créerons une supercellule euclidienne régulière (tous les angles sont droits et les longueurs des côtés sont égales) de d-dimensions, puis nous modifierons sa topologie en une topologie toroïdale en identifiant des extrémités, des côtés ou des faces opposés selon la dimensionnalité du système. Ensuite, nous allons les "coller" ensemble sans déformation (flexion) de la cellule. Par conséquent, tous les angles et les longueurs sont conservés [21]. À la suite du processus de connexion, nous avons ce que l'on appelle un tore de Clifford (CT) ou un tore plat. Un CT est un espace plat, fini et sans frontière de d-dimensions intégré dans un plan Euclidien complexe de d-dimensions comme le montre la partie droite de la Fig. 8.1 pour un $2-$CT. Un d-CT a une courbure gaussienne nulle partout, ce qui signifie que le Laplacien dans l'opérateur d'énergie cinétique est le Laplacien habituel donné par $\nabla^2 = \sum_{i=1}^{d} \partial_i^2$. En raison de la nature de

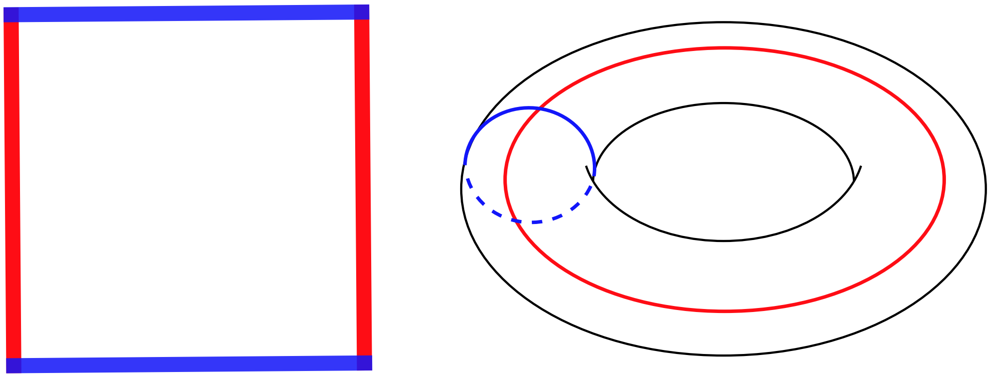

Figure 8.1: Conditions limites de Clifford dans E^2. Gauche : Carré avec l'appariement des bords opposés. Droite : 2-Torus obtenu par collage des bords opposés du carré. Le graphe encastré (cercles rouges et bleus) correspond aux bords appariés du carré.

la supercellule de Clifford (CSC), nous pouvons définir la distance entre deux points de différentes manières. D'un point de vue géométrique, nous pouvons définir la distance géodésique définie comme le plus court chemin entre deux points de la surface du tore (Voir Fig. 8.2). La distance géodésique, r_{12}^{geo} peut s'écrire comme suit

$$r_{12}^{geo} = \sqrt{\sum_{i=1}^{d} r_{12}^2(i)}, \tag{8.2}$$

où i est la somme du nombre de dimensions d. La définition de $r_{12}(i)$ est prise comme suit

$$r_{12}(i) = \begin{cases} |r_1(i) - r_2(i)| & \text{if } |r_1(i) - r_2(i)| < \frac{L}{2} \\ \\ L - |r_1(i) - r_2(i)| & \text{if } |r_1(i) - r_2(i)| > \frac{L}{2} \end{cases}. \tag{8.3}$$

Dans la Fig. 8.3, nous pouvons observer l'évolution de la distance géodésique

Figure 8.2: Représentation schématique de r_{12}^{geo} calculée comme le plus court chemin entre deux points de la surface d'un tore de Clifford à 1 de dimension.

et du potentiel de Coulomb correspondant entre un point fixé à 0 et un second point se déplaçant le long d'une ligne périodique de longueur L. On observe que, r_{12}^{geo} présente une discontinuité dans sa dérivée lorsque $r_{12}(i) = \frac{L}{2}$ ce qui implique que le potentiel de Coulomb est également discontinu en ce point. Ainsi, les forces, qui sont liées au gradient du potentiel de Coulomb, sont également discontinues en ce point. La deuxième distance est liée à la topologie du tore de Clifford d. Un d-CT est topologiquement équivalent à un d-tore.

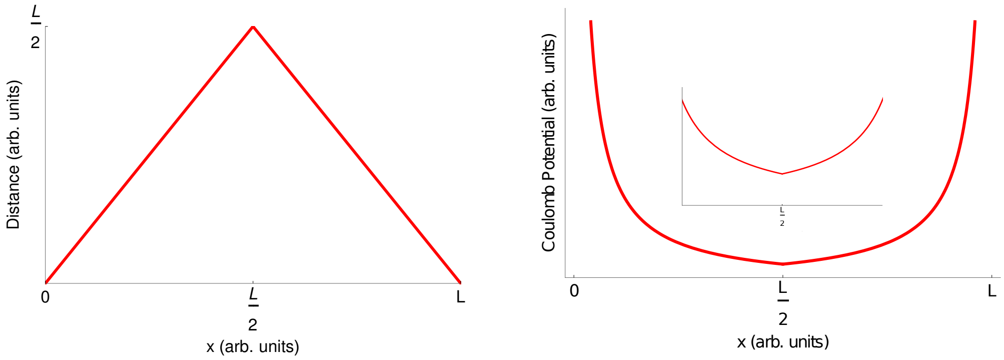

Figure 8.3: Gauche : Les distances géodésiques entre deux points sur un 1-CT de longueur L où l'un d'eux est fixé à $x = 0$. A droite : Potentiel de Coulomb entre deux charges sur un 1-CT de longueur L où une charge est fixée à $x = 0$ calculé par la géodésique. Encadré : zoom autour de $\frac{L}{2}$

Ainsi, nous pouvons définir une deuxième distance, r_{12}^{euc}, comme la longueur du plus court chemin possible entre deux points dans l'espace d'intégration du tore de Clifford. A titre d'exemple, r_{12}^{euc} est représenté par une ligne rouge sur la Fig. 8.4 pour un 1-CT de longueur L. Nous appellerons θ l'angle entre deux segments de longueur $R = \frac{L}{2\pi}$ où R est le rayon. Chaque segment relie le centre du cercle à sa position respective sur le cercle (1 et 2 sur la Fig. 8.4). Une expression pour r_{12}^{euc} peut être obtenue à partir des identités trigonométriques comme suit

$$\sin\left(\frac{\theta}{2}\right) = \frac{\frac{r_{12}^{euc}}{2}}{R} \tag{8.4}$$

et $\theta = \frac{2\pi r_{12}}{L}$, où r_{12} a été introduit dans l'équation (8.3), on obtient.

$$r_{12}^{euc} = \frac{L}{\pi}\sin^2\left(r_{12}\frac{\pi}{L}\right). \tag{8.5}$$

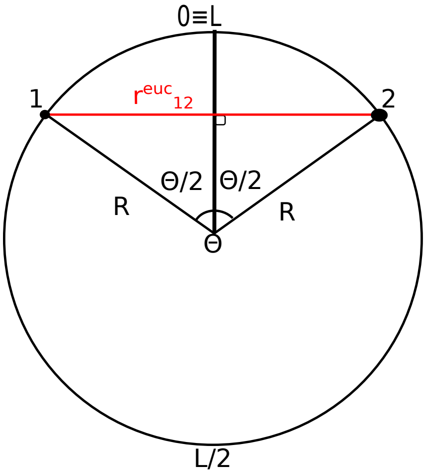

Figure 8.4: Anneau obtenu en collant ensemble les bords de la supercellule de Clifford à 1 de dimension. Dérivation graphique de la distance euclidienne dans un tore de Clifford de dimension 1

.

Pour les dimensions supérieures, nous pouvons procéder de manière similaire. Nous calculons r_{12}^{euc} dans chaque dimension, puis, par le théorème de Pythagore, nous obtenons la quantité désirée (voir Fig. 8.5 pour un exemple en 2D). L'expression générale de r_{12}^{euc} dans un système régulier à $d-$dimension où tous les angles sont des angles droits est la suivante

$$r_{12}^{euc} = \frac{L}{\pi}\sqrt{\sum_{i=1}^{d}\sin^2\left(r_{12}(i)\frac{\pi}{L}\right)}, \tag{8.6}$$

où $r_{12}(i)$ est défini dans l'équation (8.3). Dans la Fig. 8.6, nous pouvons observer l'évolution de la distance euclidienne entre un point fixé à 0 et un second point se déplaçant le long d'une ligne périodique de longueur L. Nous observons que r_{12}^{euc} est une fonction continuellement dérivable, lisse et définie de manière unique, ce qui la rend appropriée pour décrire les interactions coulombiennes à longue portée.

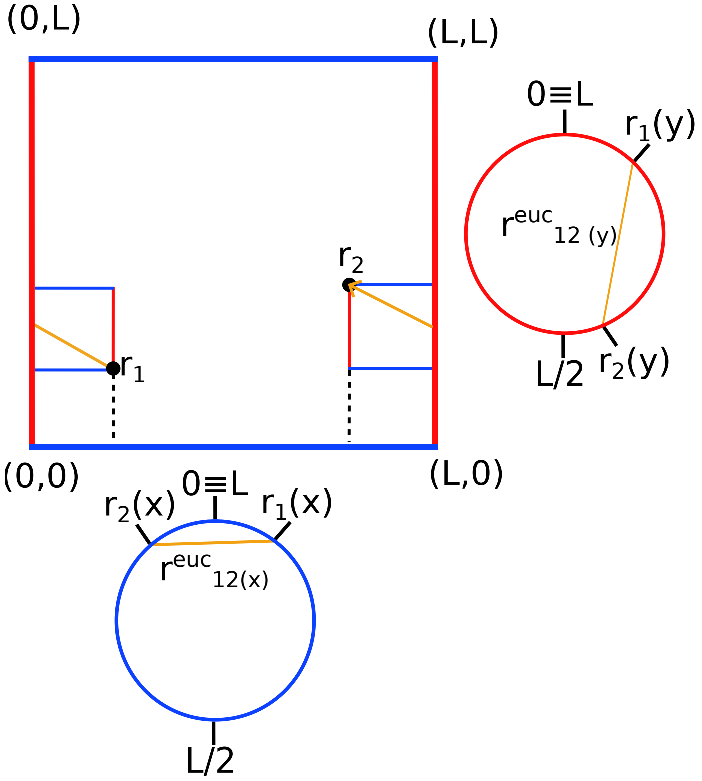

Figure 8.5: Distance euclidienne dans un tore de 2-Clifford. Un 2-CT peut être vu comme le produit cartésien de deux cercles, un dans chaque dimension.

En raison de la nature du système que nous voulons décrire, un système homogène de dimension d constitué uniquement d'électrons confinés dans un

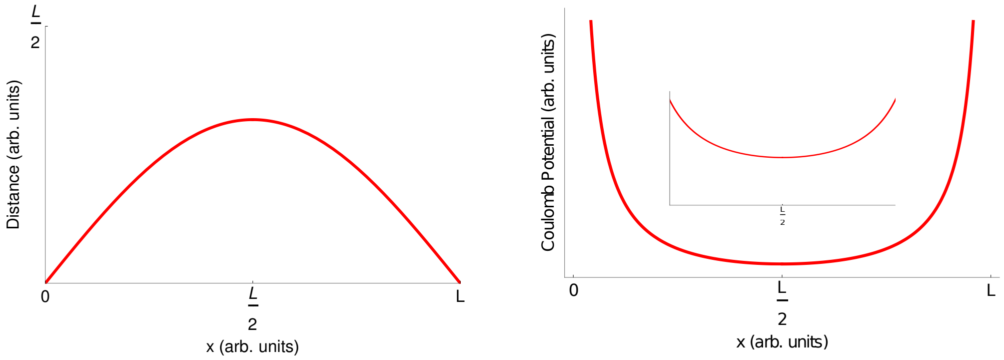

Figure 8.6: Gauche : Les distances euclidiennes entre deux points sur 1-CT de longueur L où l'un d'eux est fixé à $x = 0$. A droite : Potentiel de Coulomb entre deux charges sur 1-CT de longueur L où l'une des charges est fixée à $x = 0$, calculé par la distance euclidienne

.

tore de Clifford de dimension d, nous voulons un ensemble de base qui peut décrire avec précision la fonction d'onde dans la supercellule de Clifford entière. De plus, puisque nous voulons décrire le régime de faible densité dont les électrons se localisent, nous avons besoin d'une base localisée. En outre, la base doit permettre une évaluation simple des matrices hamiltoniennes et de recouvrement tout en fournissant des résultats précis pour un paramètre de base donné (nombre de fonctions de base et exposant orbital).

Un ensemble de base qui répond à toutes les exigences précédentes est l'ensemble de base des gaussiens distribués. Par conséquent, l'ensemble de base est constitué de fonctions gaussiennes $1s$ identiques avec le même exposant orbital, α. Une gaussienne normalisée 1-s centrée sur $\mathbf{R}_\mu$ peut être écrite comme suit

$$g_\mu(\mathbf{r};\alpha) = \left(\frac{2\alpha}{\pi}\right)^{\frac{3}{4}} e^{-\alpha|\mathbf{r}-\mathbf{R}_\mu|^2}, \tag{8.7}$$

Le nombre de fonctions de base est égal à $M = m^d$ où m est le nombre de fonctions placées sur chaque bord de la supercellule de Clifford, et d est la dimensionnalité du système. Les M orbitales tipe gaussiennes (GTO) seront répartis uniformément le long de la supercellule de Clifford avec une distance constante δ entre deux centres voisins. Une représentation graphique de l'ensemble de base pour un CSC à 2 dimensions peut être trouvée dans la Fig. 8.7.

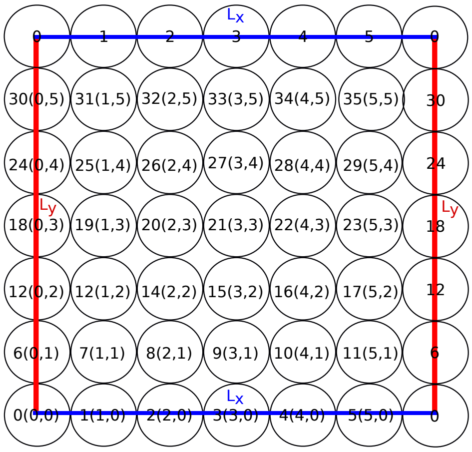

Figure 8.7: Représentation graphique de la base constituée de 36 fonctions gaussiennes distribuées dans une grille régulière bidimensionnelle.

Le chevauchement entre deux gaussiennes normalisées voisines, g_μ et g_ν, sur le CSC ayant le même exposant α est donné par

$$S_{\mu\nu}(\alpha, r^{geo}_{\mu\nu}) = \langle g_\mu | g_\nu \rangle = e^{\frac{-\alpha r^{geo2}_{\mu}}{2}}, \tag{8.8}$$

Où $r^{geo}_{\mu\nu}$ a été défini dans Eq. (8.2). Nous notons que la règle du produit gaussien ne vaut que pour $r^{geo}_{\mu\nu}$, et non pour $r^{euc}_{\mu\nu}$.

L'équation (8.8) ne dépend que du produit $\alpha(r^{geo}_{\mu,\nu})^2$, qui peut être simplifié en prenant en compte le fait que nos fonctions de base sont uniformément distribuées. Par conséquent, nous pouvons définir (en une dimension) $r^{geo}_{\mu\nu} = min(|\mu - \nu|, m - |\mu - \nu|)\delta = k\delta$ avec μ, ν entiers et $k = \mu - \nu$. Ainsi, nous pouvons définir un nouveau paramètre $\xi = \alpha\delta^2$ et réécrire le chevauchement comme suit

$$S_k(\xi) = e^{\frac{-\xi k^2}{2}}. \tag{8.9}$$

Comme on peut le voir dans l'équation (8.9), le recouvrement ne dépend plus de α et de $r^{geo}_{\mu,\nu}$ mais de k et de ξ. L'introduction du paramètre ξ présente un grand avantage puisque, dans la mesure où ξ et M sont constants, α sera mis à l'échelle de telle sorte que la matrice de recouvrement pour différentes tailles de système reste la même. Ceci est valable pour deux et trois dimensions.

La dérivation des intégrales cinétiques et coulombiennes peut être trouvée dans de nombreux manuels [55]. Par conséquent, nous nous concentrerons sur ce qui est intéressant pour la présente thèse. Comme nous l'avons vu précédemment, nous avons deux définitions différentes de la distance, $r^{geo}_{\mu\nu}$ et $r^{euc}_{\mu\nu}$. Comme nous l'avons vu précédemment, nous devons utiliser $r^{geo}_{\mu\nu}$ lorsque nous traitons des produits gaussiens. D'autre part, nous avons $r^{euc}_{\mu\nu}$, qui est approprié pour traiter les interactions coulombiennes puisqu'il s'agit d'une fonction lisse et continuellement différentiable.

En tenant compte des deux dernières affirmations, nous pouvons écrire les intégrales à un et deux électrons dans le CSC comme suit

$$T_{\mu,\nu} = \langle g_\mu| - \frac{1}{2}\nabla^2 |g_\nu\rangle = \frac{\alpha}{2}\left(3 - \alpha \; ; |r^{geo}_{\mu,\nu}|^2\right) e^{-\frac{\alpha}{2}|r^{geo}_{\mu,\nu}|^2} \tag{8.10}$$

$$\langle \mu, \nu|\rho, \sigma\rangle = 2\sqrt{\frac{\alpha}{\pi}} e^{-\frac{\alpha}{2}\left((|r^{geo}_{\mu,\rho}|^2 + (|r^{geo}_{\nu,\sigma}|^2\right)} F_0[\alpha|r^{euc}_{P,Q}|^2], \tag{8.11}$$

où

$$F_0[\alpha|r^{euc}_{P,Q}|^2] = \begin{cases} 1 & \text{if } \alpha|\bar{d}_{P,Q}|^2 \leq 10^{-8} \\ \frac{1}{2}\sqrt{\frac{\pi}{\alpha|\bar{d}_{P,Q}|^2}} erf\left(\sqrt{\alpha|r^{euc}_{P,Q}|^2}\right) & \text{if } \alpha|\bar{r}^{euc}_{P,Q}|^2 > 10^{-8} \end{cases} \tag{8.12}$$

et P et Q sont les points barycentriques des gaussiennes g_μ et g_ρ, et g_ν etg_σ, respectivement. De la même manière que pour le chevauchement, l'introduction du paramètre ξ présente un grand avantage numérique. Une fois encore, si M et ξ restent constants, nous pouvons calculer les intégrales pour $L = 1$, les stocker sur le disque et les mettre à l'échelle par un facteur $\frac{1}{L^2}$ ou $\frac{1}{L}$ pour les intégrales cinétiques et coulombiennes respectivement. En d'autres termes, les intégrales ne doivent être calculées qu'une seule fois et peuvent être appliquées à des systèmes de toute taille.

En raison de la périodicité de la supercellule de Clifford, le système est invariant par translation. Par conséquent, l'opérateur de translation, $\hat{T}_R$, commute avec le hamiltonien, $\hat{H}$, et les états propres de $\hat{H}$ peuvent être choisis pour être égaux aux états propres de $\hat{T}_R$. Il est donc pratique de construire des orbitales adaptées à la symétrie (SAOs) à partir d'une combinaison linéaire de GTOs qui satisfont l'invariance translationnelle [62]. Les SAOs (non normalisées) sont définies comme suit

$$\phi_{\mathbf{k}}(\mathbf{r}) = \frac{1}{m^{d/2}} \sum_{\boldsymbol{\mu}} e^{i\frac{2\pi}{m}\mathbf{k}\cdot\boldsymbol{\mu}} g_{\boldsymbol{\mu}}(\mathbf{r} - \mathbf{R}_{\boldsymbol{\mu}}), \tag{8.13}$$

où $\mathbf{k} = (k_1, \cdots, k_d)^T$ avec $k_i = 0, \cdots, m-1$. Nous renvoyons le lecteur à l'annexe A pour une preuve du fait que $\hat{T}_R\phi_{\mathbf{k}}(\mathbf{r}) = \phi_{\mathbf{k}}(\mathbf{r})$.

Les intégrales à un et deux électrons dans la base adaptée à la symétrie sont données par, respectivement,

$$T_{\mathbf{k},\mathbf{k}'} = \delta_{\mathbf{k},\mathbf{k}'} \mathcal{S}_{\mathbf{k}}^{-1} \sum_{\boldsymbol{\nu}} \cos\left[\frac{2\pi}{m}(\mathbf{k}\cdot\boldsymbol{\nu})\right] T_{\mathbf{0},\boldsymbol{\nu}}, \tag{8.14}$$

$$\begin{aligned} \langle \mathbf{k}, \mathbf{k}' | \mathbf{k}'', \mathbf{k}''' \rangle &= \frac{1}{m^d} \delta_{\mathbf{k}+\mathbf{k}'-\mathbf{k}''-\mathbf{k}'''} [\mathcal{S}_{\mathbf{k}} \mathcal{S}_{\mathbf{k}'} \mathcal{S}_{\mathbf{k}''} \mathcal{S}_{\mathbf{k}'''}]^{-1/2} \\ &\times \sum_{\boldsymbol{\nu}\boldsymbol{\rho}\boldsymbol{\sigma}} \cos\left[\frac{2\pi}{m}(\mathbf{k}'\cdot\boldsymbol{\nu} - \mathbf{k}''\cdot\boldsymbol{\rho} - \mathbf{k}'''\cdot\boldsymbol{\sigma})\right] \langle \mathbf{0}, \boldsymbol{\nu} | \boldsymbol{\rho}, \boldsymbol{\sigma} \rangle, \end{aligned} \tag{8.15}$$

dans lequel $\mathcal{S}_{\mathbf{k}} = \langle \phi_{\mathbf{k}} | \phi_{\mathbf{k}} \rangle$. Les intégrales à un et deux électrons, $T_{\boldsymbol{\mu},\boldsymbol{\nu}}$ et $\langle \boldsymbol{\mu}, \boldsymbol{\nu} | \boldsymbol{\rho}, \boldsymbol{\sigma} \rangle$, sont exprimées dans la base gaussienne distribuée et sont données par [55].

La dérivation des intégrales à un et deux électrons dans la base adaptée à la symétrie se trouve dans l'annexe B.

Avant d'utiliser les conditions aux limites de Clifford, nous étudions d'abord un système plus simple, à savoir 2 électrons sur un anneau. Ainsi, nous éliminons tout effet de frontière. Nous développons la fonction d'onde en termes de gaussiennes tridimensionnelles distribuées uniformément le long du périmètre de l'anneau [64, 65, 66, 67]. Nous notons qu'en confinant les électrons dans un anneau, il n'est plus nécessaire d'ajouter un fond positif [65].

Ici, nous limitons notre étude à deux électrons car cela est suffisant pour observer la localisation de Wigner tout en nous permettant d'obtenir des résultats numériquement exacts par diagonalisation exacte de l'hamiltonien. Nous analyserons plusieurs indicateurs possibles de la localisation. En particulier, nous étudierons la matrice de densité réduite à deux corps, le tenseur de localisation et l'entropie particule-trou.

Puisque les gaussiennes sont 3D, l'anneau est également 3D, ou plutôt, quasi-1D, puisque la largeur de l'anneau est beaucoup plus petite que son périmètre. Nous avons donc l'hamiltonien suivant,

$$\hat{H} = -\frac{1}{2}\nabla_1^2 - \frac{1}{2}\nabla_2^2 + \frac{1}{r_{12}}, \tag{8.16}$$

dans laquelle les deux premiers termes du côté droit sont les opérateurs d'énergie cinétique 3D pour les électrons 1 et 2, respectivement. Le dernier terme est le potentiel de Coulomb 3D répulsif dans lequel $r_{12} = |\mathbf{r}_1 - \mathbf{r}_2|$ est la distance entre les deux électrons, c'est-à-dire que les électrons interagissent à travers l'anneau. Ceci est équivalent à la distance euclidienne définie dans l'Eq. (8.6).

Nous représentons le hamiltonien dans l'équation (8.16) dans la base des gaussiens uniformément distribués que nous diagonalisons ensuite pour trouver les fonctions d'onde exactes et les énergies propres. À partir des fonctions d'onde exactes, nous pouvons alors obtenir plusieurs observables exactes d'intérêt. Nous nous concentrerons principalement sur l'état fondamental de deux électrons sur l'anneau qui est un singlet de spin.

Nous avons vérifié notre approche et sa mise en œuvre en la comparant aux résultats analytiques qui sont disponibles pour un électron confiné dans un anneau strictement 1D. Ils sont donnés par

$$E_n^{\text{exact}}(R) = \frac{n^2}{2R^2}, \tag{8.17}$$

où n est un entier et R est le rayon de l'anneau. Lorsque la largeur des gaussiennes ($\sim 1/\sqrt{\alpha}$) est beaucoup plus petite que R, le spectre d'énergie du système tend vers les énergies de l'équation (8.17).

Puisque la densité, par définition, a la même symétrie que le hamiltonien, elle aura une symétrie rotationnelle. Par conséquent, la densité à un corps sera une constante en fonction de la position sur l'anneau, et sera incapable de caractériser la localisation de Wigner. Cependant, pour 2 électrons, la localisation de Wigner peut être étudiée en utilisant la matrice de densité à deux corps, qui montre la corrélation entre les positions de deux électrons.

Dans le présent contexte, 1D, le 2-RDM joue un rôle crucial dans la mesure de la localité des électrons. En effet, en raison de l'invariance rotationnelle de la fonction d'onde, la 1-RDM est une constante, quelle que soit la nature de la fonction d'onde, puisque tous les points de l'espace sont équivalents. la nature de la fonction d'onde, puisque tous les points de l'espace sont équivalents. Par contre, c'est la 2-RDM qui est capable d'indiquer si les électrons sont fortement corrélés (localisation de Wigner), ou faiblement corrélés (gaz de Fermi).

Le tenseur de localisation permet de distinguer les comportements métalliques et isolants. Il a été développé par Resta et ses collaborateurs [69, 70, 71, 72] (voir aussi Ref. [73]) et est basée sur une idée de Kohn [74] pour décrire l'état isolant à partir de la connaissance de la fonction d'onde de l'état fondamental (voir aussi Ref. [75]).

La fractionnalité des nombres d'occupation naturels, c'est-à-dire les valeurs propres associées au 1-RDM, peut être liée à la quantité de corrélation électronique dans un système [87, 88]. Par conséquent, l'entropie particule-trou a été proposée comme une mesure de la présence de la corrélation dans un système [89, 88].

Dans la Fig. 8.8, nous reportons la matrice de densité réduite à deux corps $\Gamma^{(2)}(0, x)$ en fonction de x pour différentes valeurs de la longueur du périmètre L de l'anneau. Elle donne l'amplitude de la probabilité de trouver un électron à x alors qu'un autre électron est présent à $x = 0$.

À grande densité électronique (petit L), $\Gamma^{(2)}(0, x)$ est presque constant, car l'énergie cinétique domine la répulsion électronique. C'est le régime de Fermi-Gas. Au contraire, à faible densité électronique (grand L), le second électron a la plus grande amplitude à $x = L/2$, c'est-à-dire exactement à la position qui est opposée à celle du premier électron. La répulsion électronique est dominante et pousse les deux électrons à des positions opposées sur l'anneau. En augmentant L, la matrice de densité réduite à deux corps devient de plus en plus localisée. Pour de très grandes valeurs de L, la matrice de densité devient proche d'une fonction delta. Il y a formation d'un "réseau" électronique 1D, on observe la localisation de Wigner. Il est difficile de déterminer exactement pour quelle longueur se produit la transition entre le régime de Fermi et le régime de Wigner. Néanmoins, la localisation de Wigner devient apparente pour des longueurs de l'ordre de $L = 10$ Bohr.

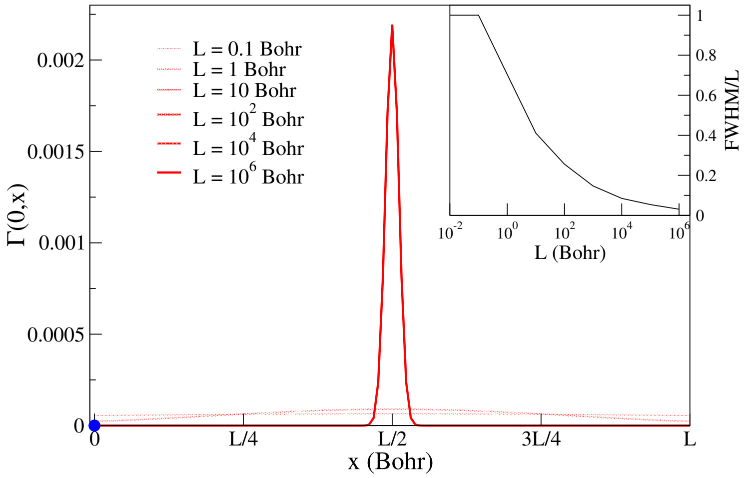

Figure 8.8: La matrice de densité réduite à deux corps $\Gamma(0, x)$ pour deux électrons sur un anneau pour différentes valeurs de la longueur L du périmètre. La position du premier électron est fixée à $x = 0$ (indiquée par le point bleu). Encart : Largeur totale à mi-hauteur (FWHM) de $\Gamma^{(2)}(0, x)$ normalisée par rapport à L en fonction de L. Pour de petits L, la FWHM n'est pas bien définie et la FWHM normalisée est fixée à 1.

Afin de comparer les tenseurs de localisation pour des systèmes de différentes tailles, nous reportons dans la Fig. 8.9 la quantité sans dimension λ/L^2 en fonction de la longueur L du périmètre de l'anneau. Nous voyons que pour une grande densité ($L < 0.1$) λ/L^2 est presque constante tandis que sa valeur commence à diminuer pour $L > 1$ Bohr. Ceci marque le début de la transition vers un état localisé. Pour une densité très faible, $L \gg 1$, le tenseur de localisation disparaît presque, indiquant clairement la localisation de Wigner. Le comportement du tenseur de localisation est en accord avec les matrices de densité réduite à 2 corps rapportées dans la Fig. 8.8, c'est-à-dire que la transition du régime de Fermi-gas au régime de Wigner se produit dans la région autour de $L = 10$ Bohr.

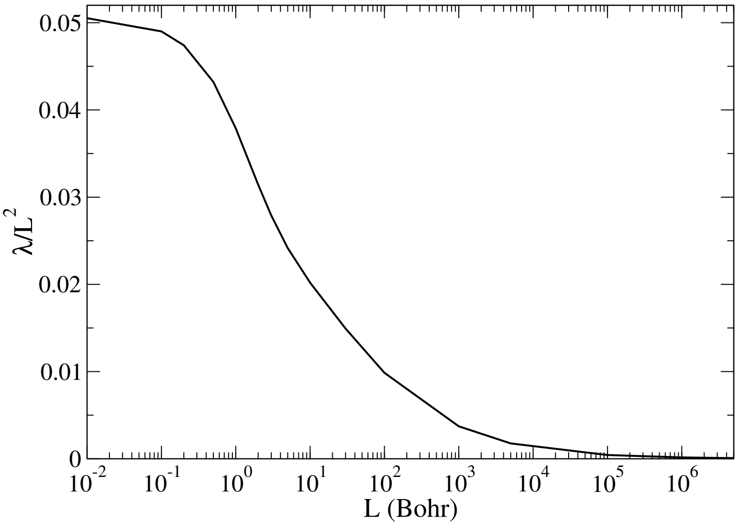

Figure 8.9: La trace du tenseur de localisation λ/L^2 en fonction de la longueur L du périmètre de l'anneau

.

Dans la Fig. 8.10, nous reportons l'entropie particule-trou en fonction de la longueur L du périmètre de l'anneau. Pour les grandes densités moyennes ($L \ll 1$), l'entropie S est très faible puisque le gaz de Fermi peut être décrit avec précision par un seul déterminant de Slater. Cependant, pour les grands systèmes (faible densité électronique), l'entropie est à sa valeur la plus élevée. L'entropie commence à augmenter rapidement pour $L > 1$ Bohr, indiquant la transition vers le régime de Wigner.

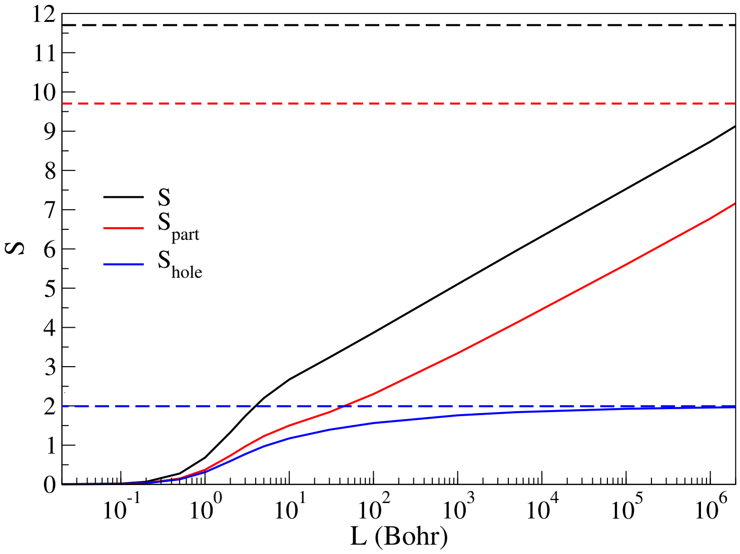

Figure 8.10: L'entropie S en fonction de la longueur L du périmètre de l'anneau. Noir : entropie totale ; Rouge : entropie des particules ; Bleu : entropie des trous. Les lignes en pointillés indiquent les limites asymptotiques des entropies lorsque $L \to \infty$. .

Nous allons maintenant généraliser notre approche pour étudier la localisation de Wigner aux faibles densités dans des systèmes à deux et trois dimensions. Nous allons étudier un système constitué de 2 électrons en interaction électrons en interaction confinés dans un tore de Clifford de dimension d.

Le hamiltonien du système est

$$\hat{H} = -\frac{1}{2}\nabla_1^2 - \frac{1}{2}\nabla_2^2 + \frac{1}{r_{12}^{euc}}, \tag{8.18}$$

Nous résolvons l'équation de Schrödinger indépendante du temps impliquant le hamiltonien dans l'équation (8.18) en employant une approche de diagonalisation exacte. Par conséquent, nous projetons l'hamiltonien sur la base des déterminants de Slater à 2 électrons et diagonalisons la matrice hamiltonienne résultante pour obtenir les fonctions d'onde et les énergies propres.

Puisque nous voulons décrire un effet de localisation des électrons, il est pratique d'utiliser un ensemble de base localisé. De plus, nous travaillerons dans la base adaptée à la symétrie dont nous avons brièvement parlé précédemment.

Nous avons validé notre méthode en comparant ses résultats à ceux obtenus dans un modèle semi-classique qui devient exact dans la limite de la vanité de la densité.

Dans les Figs. 8.11-8.14 nous reportons le $\Gamma_{\mathbf{0},\boldsymbol{\nu}}$. d'un CSC carré bidimensionnel pour $L = 1$, $L = 10^2$, $L = 10^4$, et $L = 10^6$ bohr, respectivement. Comme c'était le cas en 1D, pour de petites valeurs de L le système 2D se comporte comme un gaz de Fermi puisque $\Gamma_{\mathbf{0},\boldsymbol{\nu}}$ est presque constante. Au contraire, lorsque la taille du système augmente, nous pouvons clairement observer la localisation des électrons à partir de la structure en pointe de $\Gamma_{\mathbf{0}}^{\mathbf{0},0}$. En 2D, la position ayant la plus grande probabilité de trouver le deuxième électron se trouve au milieu du CSC carré, ce qui maximise la distance entre les deux électrons.

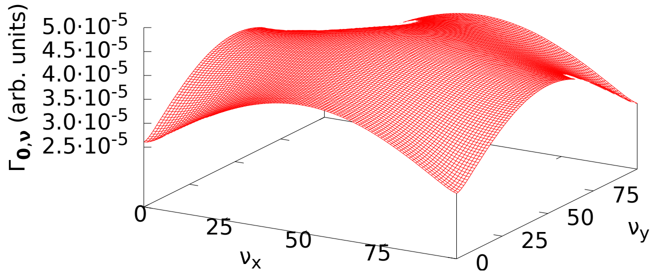

Figure 8.11: $\Gamma_{\mathbf{0},\boldsymbol{\nu}}$ en fonction de $\boldsymbol{\nu}$ pour deux électrons dans une supercellule de Clifford carrée à deux dimensions avec un bord de longueur $L = 1$ bohr. La position d'un électron est fixée à l'origine $\boldsymbol{\nu} = \mathbf{0}$.

Dans les Figs. 8.15-8.17 nous rapportons $\Gamma_{\mathbf{0},\boldsymbol{\nu}}$ d'un CSC cubique tridimen-

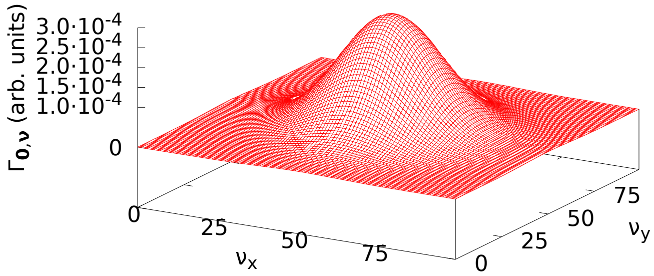

Figure 8.12: $\Gamma_{\mathbf{0},\boldsymbol{\nu}}$ en fonction de $\boldsymbol{\nu}$ pour deux électrons dans une supercellule de Clifford carrée à deux dimensions avec un bord de longueur $L = 100$ bohr. La position d'un électron est fixée à l'origine $\boldsymbol{\nu} = \mathbf{0}$.

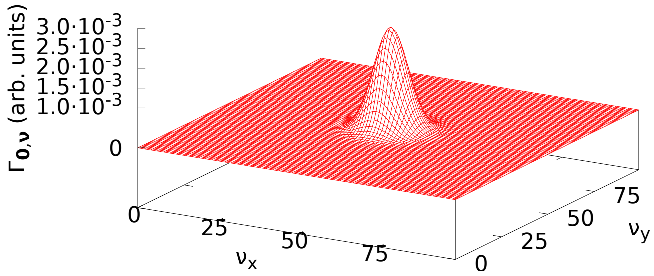

Figure 8.13: $\Gamma_{\mathbf{0},\boldsymbol{\nu}}$ en fonction de $\boldsymbol{\nu}$ pour deux électrons dans une supercellule de Clifford carrée à deux dimensions avec un bord de longueur $L = 10^4$ bohr. La position d'un électron est fixée à l'origine $\boldsymbol{\nu} = \mathbf{0}$.

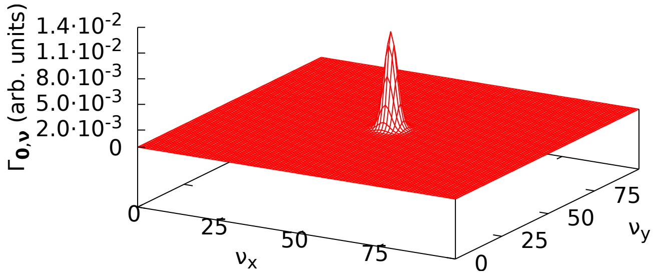

Figure 8.14: $\Gamma_{\mathbf{0},\boldsymbol{\nu}}$ en fonction de $\boldsymbol{\nu}$ pour deux électrons dans une supercellule de Clifford carrée à 2 dimensions avec un bord de longueur $L = 10^6$ bohr. La position d'un électron est fixée à l'origine $\boldsymbol{\nu} = \mathbf{0}$.

sionnel pour $L = 1$, $L = 10^2$, et $L = 10^4$ bohr, respectivement. Nous notons que $\Gamma_{\mathbf{0},\boldsymbol{\nu}}$ est représenté par un gradient de couleur, du bleu (petit) au rouge (grand). Nous demandons au lecteur de prêter attention au fait qu'il existe des différences significatives dans l'échelle des différentes figures. En tenant compte de cela, nous voyons une fois de plus que pour les petits L, nous avons une $\Gamma_{\mathbf{0},\boldsymbol{\nu}}$ tandis que pour de grands L on observe que $\Gamma_{\mathbf{0},\boldsymbol{\nu}}$ est localisé au milieu du CSC cubique, qui est le point le plus éloigné de l'autre électron situé à l'origine.

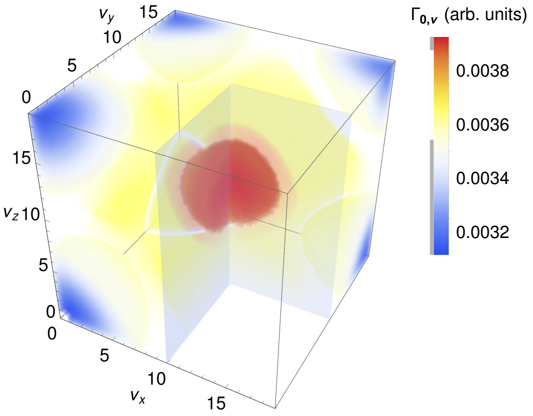

Figure 8.15: $\Gamma_{\mathbf{0},\boldsymbol{\nu}}$ en fonction de $\boldsymbol{\nu}$ pour deux électrons dans une supercellule de Clifford cubique à 3 dimensions avec un bord de longueur $L = 1$ bohr. La position d'un électron est fixée à l'origine $\boldsymbol{\nu} = \mathbf{0}$.

Après avoir validé l'approche et avoir pu observer clairement les localisations de Wigner, nous allons étendre notre approche à un nombre arbitraire d'électrons en une et deux dimensions. Puisque les calculs dans nos chapitres précédents étaient limités à deux électrons, nous pouvions résoudre l'équation de Schrödinger en utilisant la diagonalisation exacte. Pour de nombreux électrons, la diagonalisation exacte devient numériquement intraitable ; nous devons donc utiliser une approche qui soit à la fois précise mais aussi

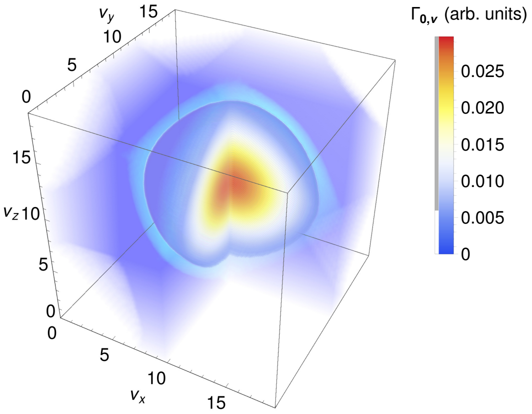

Figure 8.16: $\Gamma_{\mathbf{0},\boldsymbol{\nu}}$ en fonction de $\boldsymbol{\nu}$ pour deux électrons dans une supercellule de Clifford cubique à 3 dimensions avec un bord de longueur $L = 100$ bohr. La position d'un électron est fixée à l'origine $\boldsymbol{\nu} = \mathbf{0}$.

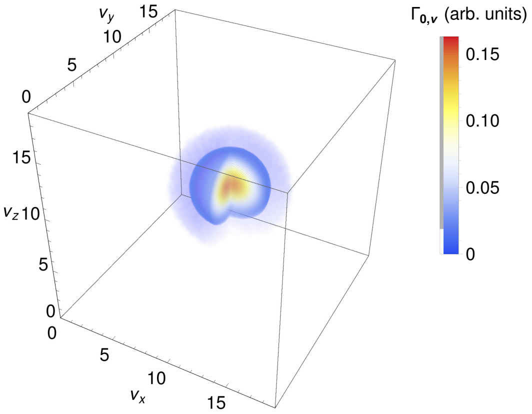

Figure 8.17: $\Gamma_{\mathbf{0},\boldsymbol{\nu}}$ en fonction de $\boldsymbol{\nu}$ pour deux électrons dans une supercellule de Clifford cubique à 3 dimensions avec un bord de longueur $L = 10000$ bohr. La position d'un électron est fixée à l'origine $\boldsymbol{\nu} = \mathbf{0}$.

numériquement efficace. Comme nous le démontrerons par la suite, nous avons constaté que la méthode Hartree-Fock restreinte à enveloppe ouverte (ROHF) est suffisante pour capturer avec précision la localisation des électrons. Enfin, comme les systèmes de Wigner à quelques électrons peuvent être considérés comme des fragments de cristaux de Wigner, nous les appellerons fragments de Wigner.

L'hamiltonien des fragments de Wigner que nous allons étudier est donné par

$$\hat{H} = -\frac{1}{2}\sum_{i=1}^{N}\nabla_i^2 - \sum_{i=1}^{N}\frac{q}{r_{iq}^{euc}} + \sum_{i=1}^{N}\sum_{j>i}^{N}\frac{1}{r_{\mu\nu}^{euc}} \tag{8.19}$$

Nous utiliserons un ensemble de base gaussien distribué pour effectuer nos calculs numériques et nous comparerons nos résultats pour les positions d'équilibre des électrons obtenus à une densité moyenne petite mais finie à ceux obtenus pour un CSC avec des charges ponctuelles classiques. Pour déterminer ces positions, nous minimiserons l'énergie de ces fragments de Wigner classiques en utilisant la méthode de Newton-Raphson [106]. L'énergie totale d'un CSC contenant N charges ponctuelles est donnée par

$$\begin{aligned} U(r_1, r_2, \ldots, r_N) =& \sum_{i>j}^{N}\frac{1}{r_{ij}^{euc}} = \\ =& \frac{\pi}{L\sum_{i>j}^{N}\sqrt{\sum_{x=1}^{d}\sin^2\left(r_{ij}(x)\frac{\pi}{L}\right)}} \end{aligned} \tag{8.20}$$

Nous utilisons une charge fractionnaire de $q = 0,01$ a.u. située à l'origine du système de coordonnées pour obtenir un fragment de Wigner épinglé. La taille du CSC est choisie pour être proportionnelle au nombre d'électrons et au nombre de dimensions du système. Nous utilisons 200 Bohr par électron et par dimension. Dans le cas des fragments de Wigner unidimensionnels, le nombre de fonctions de base gaussiennes est également proportionnel au nombre d'électrons du système. Nous utilisons 10 gaussiennes par électron. Dans le cas de fragments de Wigner bidimensionnels, nous fixons le nombre de gaussiens à 400, c'est-à-dire 20 gaussiens par dimension. Tous les calculs ont été effectués avec une version modifiée du progiciel Dalton [107]. En particulier, les intégrales de chevauchement, à un et deux électrons ont été modifiées pour les rendre compatibles avec les conditions limites périodiques de Clifford.

À faible densité, nous nous attendons à ce que la configuration de spin du fragment de Wigner ait peu d'effet sur la localisation des électrons. Par conséquent, nous nous concentrerons sur l'état de spin élevé, c'est-à-dire l'état de spin pour lequel S_z a sa valeur maximale, car, grâce au principe de Pauli, un seul déterminant de Slater sera suffisant pour décrire le système [108]. Cela nous permettra ensuite d'utiliser l'approche Hartree-Fock restreinte à coquille ouverte (ROHF), efficace sur le plan numérique, pour décrire précisément ce système.

Bien que nous nous intéressions principalement aux fragments de Wigner bidimensionnels, nous étudierons d'abord les systèmes unidimensionnels car cela nous permettra de comparer les résultats de la méthode ROHF à ceux obtenus en utilisant l'interaction de configuration complète (FCI) qui donne le résultat exact pour l'ensemble de base donné. A titre d'exemple, nous reportons dans la Fig. 8.18 la densité d'un corps dans un CSC unidimensionnel pour 5 électrons. Le profil de densité obtenu dans FCI montre clairement 5 pics distincts démontrant la localisation de Wigner. La Fig. 8.18 présente également la densité du même système mais calculée dans ROHF. Nous observons que ces résultats sont très similaires à ceux obtenus dans FCI. Bien

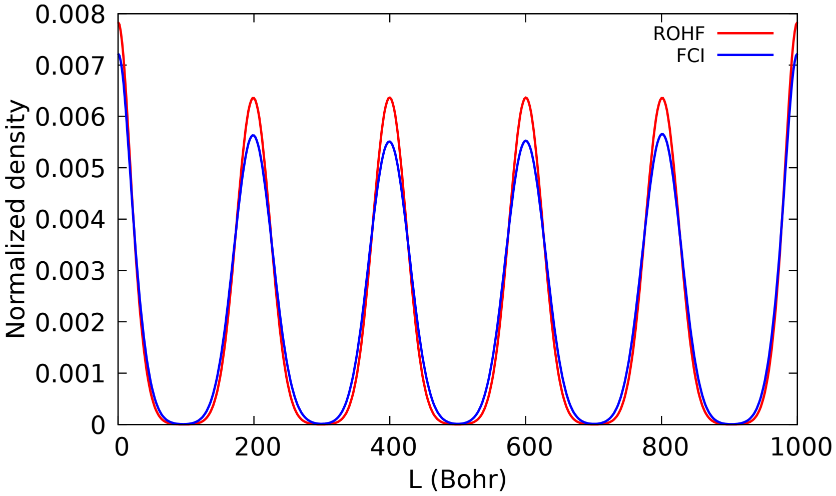

Figure 8.18: La densité de cinq électrons dans un CSC unidimensionnel. Bleu : FCI ; rouge : ROHF.

que ROHF surlocalise légèrement les électrons, les profils de densité de FCI et de ROHF sont équivalents. Nous avons obtenu des résultats similaires pour d'autres fragments de Wigner 1D [9]. Par conséquent, dans la suite, nous allons étudier les fragments de Wigner 2D dans leurs états de spin élevé au sein de ROHF.

Dans le panneau gauche de la Fig. 8.19, nous montrons la densité électronique d'un fragment de Wigner avec trois électrons. Nous observons que les électrons se localisent sur la diagonale du CSC. Le système 2D à trois électrons se comporte donc comme un système 1D de longueur $L = \sqrt{L_x^2 + L_y^2}$. Nous notons que la solution obtenue est dégénérée avec une autre solution dans laquelle les électrons se localisent sur l'autre diagonale du CSC. Dans la suite, pour des raisons de simplicité, nous éviterons de discuter des solutions dégénérées que nous avons obtenues puisque les profils de densité de toutes les solutions dégénérées sont équivalents. Dans le panneau de droite de la Fig. 8.19, nous montrons les positions de trois charges ponctuelles classiques correspondant à l'énergie minimale de ces charges dans le CSC. Comme prévu, nous observons que les positions des charges ponctuelles classiques correspondent aux positions des électrons. Nous avons effectué des calculs similaires pour les fragments de Wigner 2D jusqu'à 10 électrons.

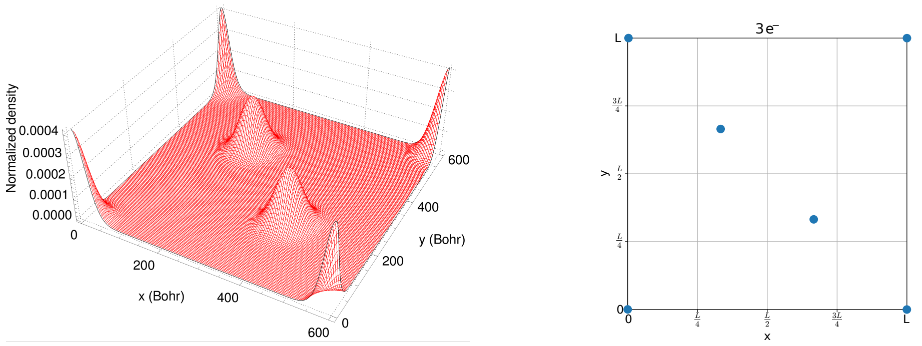

Figure 8.19: Panneau de gauche : La densité ROHF pour trois électrons confinés dans un CSC 2D. Panneau de droite : les positions d'équilibre classiques pour trois charges ponctuelles confinées dans un CSC 2D.

Le modèle de localisation le plus intéressant se produit pour un fragment de Wigner avec 8 électrons, comme on peut le vérifier dans le panneau de droite de la Fig. 8.20. Nous voyons que les électrons se localisent dans un réseau hexagonal déformé. Ce résultat est à nouveau confirmé par les positions des charges ponctuelles correspondant à leur énergie totale minimale. Le réseau hexagonal est la structure de réseau du cristal de Wigner 2D qui présente l'énergie la plus faible par rapport aux autres réseaux standard et, en particulier, au réseau carré. Dans notre cas, nous ne trouvons pas de réseau hexagonal parfait parce que nous avons fixé les longueurs des deux bords du CSC comme étant égales. Si, au contraire, nous choisissions que le rapport entre les deux bords soit égal à $\sqrt{3}/2$, nous nous attendons à trouver un réseau hexagonal parfait.

Suivant cette dernière hypothèse, nous avons effectué un calcul avec 12

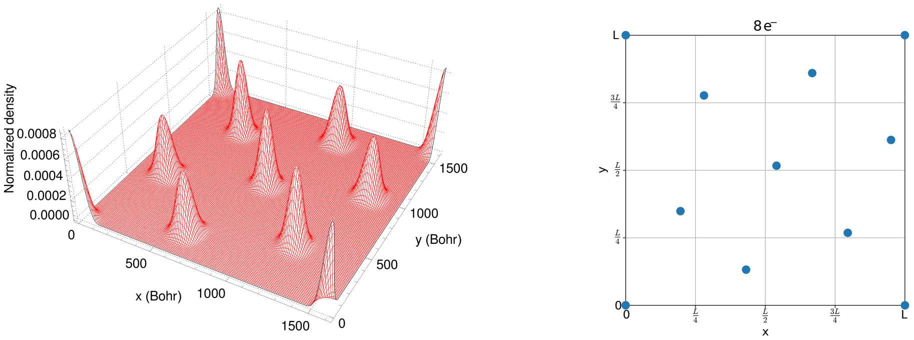

Figure 8.20: Panneau de gauche : La densité ROHF pour huit électrons confinés dans un CSC 2D. Panneau de droite : les positions d'équilibre classiques pour huit charges ponctuelles confinées dans un CSC 2D.

électrons confinés dans un CSC rectangulaire avec un rapport $\sqrt{3}/2 : 1$ des deux bords qui est compatible avec une structure hexagonale. Nous avons utilisé un ensemble de base constitué de 22 gaussiennes dans la direction x et 19 dans les directions y. La densité unique de ce fragment de Wigner se trouve sur la Fig. 8.21. Nous observons que les électrons forment un réseau hexagonal légèrement étiré, ce qui semble indiquer l'émergence de la structure du réseau hexagonal dans un gaz d'électrons bidimensionnel uniforme à faible densité. Des travaux sont en cours pour augmenter le nombre d'électrons dans les calculs afin d'essayer de trouver un réseau hexagonal parfait.

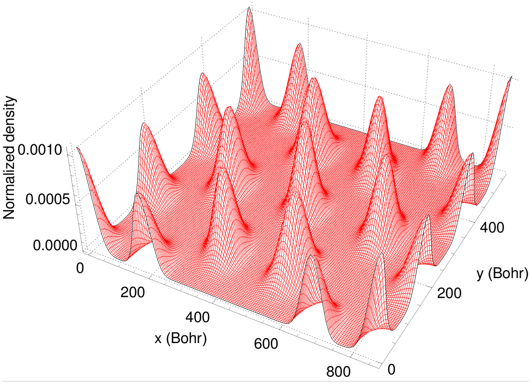

Figure 8.21: La densité ROHF pour douze électrons confinés dans un CSC rectangulaire.

Nous notons que pour les réseaux rectangulaires, l'expression de $r_{\mu\nu}^{euc}$ donnée dans l'Eq. (8.6) n'est pas valide puisque L_x est différent de L_y. Ainsi, une généralisation de l'Eq. (8.6) est donnée par

$$r_{\mu\nu}^{euc} = \sum_{i=1}^{d} \sqrt{\frac{L_i^2}{\pi^2} \sin^2\left(\frac{\pi r_{\mu\nu}(i)}{L_i}\right)}, \tag{8.21}$$

où i est la somme des composantes cartésiennes, L_i est la longueur du système dans la direction i et $r_{\mu\nu}(i)$ est défini dans l'équation 8.3.

Cette thèse présente une nouvelle approche pour traiter les électrons fortement corrélés. Cette approche repose sur deux idées principales. Premièrement, nous avons introduit l'utilisation des conditions limites de Clifford. La stratégie générale des conditions aux limites proposées consiste à transformer un grand fragment (une supercellule) d'un système périodique en un tore de Clifford, puis à redéfinir la distance entre deux points en prenant la distance euclidienne entre ces points dans l'espace d'encastrement du tore. Deuxièmement, nous avons décrit l'ensemble de base gaussien distribué qui consiste à placer des orbitales 1s régulièrement espacées avec un exposant orbital commun. Dans la suite, nous avons présenté les résultats. Le premier d'entre eux consiste en l'étude de deux électrons confinés dans un anneau. Nous avons vu qu'à haute densité, la fonction d'onde du système est similaire à celle d'un système à électrons libres. Cependant, en diminuant la densité, il y a un changement complet de la structure de la fonction d'onde. la structure de la fonction d'onde. Les électrons passent d'un état où ils sont essentiellement délocalisés, et bien décrits par un déterminant de Slater unique, à un état où ils sont localisés à des positions fixes dans l'espace. Nous avons obtenu un aperçu plus profond de la nature de la localisation des électrons en étudiant le tenseur de localisation et l'entropie des électrons. entropie des électrons. En effet, en diminuant la densité électronique, nous observons une croissance soudaine de l'entropie et une chute correspondante de l'étalement de position dans le régime de densité où la densité de l'électron est la plus élevée. de l'étalement de position dans le régime de densité où les électrons se localisent. La chute de l'étalement de position indique une mobilité réduite des électrons par rapport à la solution de Fermi-gaz. Ce comportement est une signature de la localisation de Wigner. L'augmentation de l'entropie électronique indique également que l'état de faible densité est beaucoup plus corrélé que l'état de Fermi-gaz, qui tend vers un déterminant unique (corrélation nulle) dans la limite des très hautes densités.

Nous avons présenté une approche précise et numériquement efficace pour étudier la localisation de Wigner dans des systèmes de différentes dimensions (1D, 2D, 3D). Ses principales caractéristiques sont : 1) l'application de conditions limites périodiques de Clifford avec une distance renormalisée pour décrire le potentiel de Coulomb et 2) l'utilisation de fonctions de base gaussiennes qui sont placées sur une grille régulière à l'intérieur d'une supercellule de Clifford. Nous avons validé notre méthode en comparant ses résultats à ceux obtenus dans le cadre d'un modèle semi-classique qui devient exact dans la limite de vanité de la densité. Enfin, en utilisant la matrice de densité réduite à deux corps, nous avons démontré que notre approche peut capturer avec précision la localisation de Wigner. Enfin, nous avons généralisé l'approche à un gaz d'électrons homogène avec plus de 2 électrons à de très faibles densités en 1 et 2 dimensions. Nous avons étudié plusieurs fragments de Wigner épinglés et avons clairement observé la localisation de Wigner à partir de la densité à un corps. Nous avons également observé l'émergence naturelle de l'empilement hexagonal comme la configuration la plus stable. De plus, nous avons validé notre méthode en comparant la position d'équilibre des électrons avec celles obtenues par une procédure de minimisation de l'énergie classique d'un fragment de Wigner.

Notre travail d'approche ouvre la voie à plusieurs développements futurs intéressants : (1) L'étude de fragments de Wigner tridimensionnels pour vérifier si la structure bcc émerge comme cela a été prédit. (2) La combinaison de notre approche de Clifford avec les méthodes de Monte Carlo quantique pour étudier les cristaux de Wigner. (3) L'extension de l'approche au traitement des solides. (4) Le développement d'une approche classique plus précise en utilisant des gradients analytiques et l'implémentation de gradients conjugués pour minimiser l'énergie nous permettra de traiter classiquement un plus grand nombre d'électrons et d'aborder le problème de Thomson sur un tore de Clifford.

Appendices

Appendix A

Translational symmetry of the symmetry adapted orbitals

A normalized 1-s Gaussian can be written as

$$g_{\mu}(\mathbf{r}-\mathbf{R}_{\mu}) = \left(\frac{2\alpha}{\pi}\right)^{\frac{3}{4}} e^{-\alpha|\mathbf{r}-\mathbf{R}_{\mu}|^2}, \tag{A.1}$$

Where $\mathbf{R}_{\mu}$ is the position of the center of the Gaussian. We consider m^d equidistant gaussian functions with the nearest-neighbor distance equal to δ and we define $V = L^d$ the size of our system, where $L = m\delta$ with m an integer. We define

$$\mathbf{M} = m\mathbf{n} \tag{A.2}$$

$$\mathbf{T} = L\mathbf{n} = \delta\mathbf{M}, \tag{A.3}$$

where

$$\mathbf{n} = \sum_{i=1}^{d} n_i \mathbf{e}_i, \tag{A.4}$$

in which n_i are integers and $\mathbf{e}_i$ are unit vectors. We have the following identity.

$$g_{\mu}(\mathbf{r}-\mathbf{R}_{\mu+\mathbf{M}}+\mathbf{T}) = g_{\mu}(\mathbf{r}-\mathbf{R}_{\mu}) \tag{A.5}$$

because $\mathbf{R}_{\mu+\mathbf{M}} = \mathbf{R}_{\mu} + \delta\mathbf{M} = \mathbf{R}_{\mu} + \mathbf{T}$.

The symmetry-adapted orbitals were defined in Eq. (3.24). We repeat the definition here for convenience,

$$\phi_{\mathbf{k}}(\mathbf{r}) = \frac{S_{\mathbf{k}}^{-1/2}}{m^{d/2}} \sum_{\boldsymbol{\mu}} e^{i\frac{2\pi}{m}\mathbf{k}\cdot\boldsymbol{\mu}} g(\mathbf{r} - \mathbf{R}_{\boldsymbol{\mu}}). \tag{A.6}$$

They respect the translational symmetry, i.e.,

$$\phi_{\mathbf{k}}(\mathbf{r} + \mathbf{T}) = \phi_{\mathbf{k}}(\mathbf{r}) \tag{A.7}$$

Proof:

$$\phi_{\mathbf{k}}(\mathbf{r} + \mathbf{T}) = \frac{S_{\mathbf{k}}^{-1/2}}{m^{d/2}} \sum_{\boldsymbol{\mu}} e^{i\frac{2\pi}{m}\mathbf{k}\cdot\boldsymbol{\mu}} g(\mathbf{r} - \mathbf{R}_{\boldsymbol{\mu}} + \mathbf{T}) \tag{A.8}$$

Introducing the change of variable $\boldsymbol{\nu} = \boldsymbol{\mu} - \mathbf{M}$ we obtain

$$\begin{aligned}
\phi_{\mathbf{k}}(\mathbf{r} + \mathbf{T}) &= \frac{S_{\mathbf{k}}^{-1/2}}{m^{d/2}} \sum_{\boldsymbol{\mu}} e^{i\frac{2\pi}{m}\mathbf{k}\cdot(\boldsymbol{\nu}+\mathbf{M})} g(\mathbf{r} - \mathbf{R}_{\boldsymbol{\nu}+\mathbf{M}} + \mathbf{T}) && \text{(A.9)} \\
&= \frac{S_{\mathbf{k}}^{-1/2}}{m^{d/2}} \sum_{\boldsymbol{\nu}} e^{i\frac{2\pi}{m}\mathbf{k}\cdot\boldsymbol{\nu}} g(\mathbf{r} - \mathbf{R}_{\boldsymbol{\nu}}) = \phi_{\mathbf{k}}(\mathbf{r}) && \text{(A.10)}
\end{aligned}$$

where we used Eq. (A.5) and the fact that $e^{i\frac{2\pi}{m}\mathbf{k}\cdot\mathbf{M}} = e^{i2\pi\mathbf{k}\cdot\mathbf{n}} = 0$.

Appendix B

One- and two-electron integrals in the symmetry adapted basis

---

B.1 one-electron Integrals

We assume to have the one-electron and two-electron integrals on the gaussian basis set,

$$g_{\boldsymbol{\mu}}(\mathbf{r}-\mathbf{R}_{\boldsymbol{\mu}}) = \left(\frac{2\alpha}{\pi}\right)^{\frac{3}{4}} e^{-\alpha|\mathbf{r}-\mathbf{R}_{\boldsymbol{\mu}}|^2}, \tag{B.1}$$

These orbitals are Normalized and non-orthogonal. The 1-e and 2-e integrals are to be transformed onto the symmetry basis set, 3.24

The Hamiltonian integrals over the gaussian basis set are $T_{\mu,\nu}$ and $< \mu, \nu|\rho, \sigma >$, while the overlap integrals are $S_{\mu,\nu}$. In order to obtain the transformed quantities, one should remind that, because of the symmetry properties of the local basis set, for the kinetic-energy matrix elements, we have:

$$T_{\boldsymbol{\mu},\boldsymbol{\nu}} \;=\; T_{\boldsymbol{\mu}+\boldsymbol{\delta},\boldsymbol{\nu}+\boldsymbol{\delta}} \tag{B.2}$$

$$T_{\boldsymbol{\mu},\boldsymbol{\nu}} \;=\; T_{\mathbf{M}-\boldsymbol{\mu},\mathbf{M}-\boldsymbol{\nu}} \tag{B.3}$$

These properties can be explained straightforwardly by looking at the distance between Gaussians $\boldsymbol{\mu}$ and $\boldsymbol{\nu}$,

$$r_{\boldsymbol{\mu},\boldsymbol{\nu}} = r_{-\boldsymbol{\mu},-\boldsymbol{\nu}} \tag{B.4}$$

$$r_{\boldsymbol{\mu},\boldsymbol{\nu}} = r_{\boldsymbol{\mu}+\boldsymbol{\delta},\boldsymbol{\nu}+\boldsymbol{\delta}} \tag{B.5}$$

where $\mathbf{M}$ is defined in Eq. (A.2). Let us now work out the one-electron integrals in the symmetry adapted basis. We have

$$\begin{aligned} T_{\mathbf{k},\mathbf{k}'} &= \langle\phi_{\mathbf{k}}| - \frac{1}{2}\nabla^2|\phi_{\mathbf{k}'}\rangle && \text{(B.6)}\\ &= \frac{1}{m^d}\sum_{\boldsymbol{\mu},\boldsymbol{\nu}} e^{-i\frac{2\pi}{m}[\mathbf{k}\cdot\boldsymbol{\mu}-\mathbf{k}'\cdot\boldsymbol{\nu}]}T_{\boldsymbol{\mu},\boldsymbol{\nu}} && \text{(B.7)} \end{aligned}$$

where $T_{\boldsymbol{\mu},\boldsymbol{\nu}}$ are the 1-electron integrals in the gaussian basis defined in Eq. (3.13). Making use of the property of $T_{\boldsymbol{\mu},\boldsymbol{\nu}}$ given in Eq. (B.2) and setting $\boldsymbol{\delta} = -\boldsymbol{\mu}$ we obtain

$$\begin{aligned} T_{\mathbf{k},\mathbf{k}'} &= \frac{1}{m^d}\sum_{\boldsymbol{\mu},\boldsymbol{\nu}} e^{-i\frac{2\pi}{m}[\mathbf{k}\cdot\boldsymbol{\mu}-\mathbf{k}'\cdot\boldsymbol{\nu}]}T_{\mathbf{0},\boldsymbol{\nu}-\boldsymbol{\mu}} && \text{(B.8)}\\ &= \frac{1}{m^d}\sum_{\boldsymbol{\mu},\boldsymbol{\nu}} e^{-i\frac{2\pi}{m}[(\mathbf{k}-\mathbf{k}')\cdot\boldsymbol{\mu}-\mathbf{k}'\cdot(\boldsymbol{\nu}-\boldsymbol{\mu})]}T_{\mathbf{0},\boldsymbol{\nu}-\boldsymbol{\mu}} && \text{(B.9)} \end{aligned}$$

Performing a change of variable $\boldsymbol{\nu}' = \boldsymbol{\nu} - \boldsymbol{\mu}$ we can rewrite the above equation according to

$$\begin{aligned} T_{\mathbf{k},\mathbf{k}'} &= \frac{1}{m^d}\sum_{\boldsymbol{\nu}} e^{-i\frac{2\pi}{m}(\mathbf{k}-\mathbf{k}')\cdot\boldsymbol{\nu}}\sum_{\boldsymbol{\nu}'} e^{i\frac{2\pi}{m}\mathbf{k}\cdot\boldsymbol{\nu}'}T_{\mathbf{0},\boldsymbol{\nu}'} && \text{(B.10)}\\ &= \delta_{\mathbf{k},\mathbf{k}'}\sum_{\boldsymbol{\nu}'} e^{i\frac{2\pi}{m}\mathbf{k}'\cdot\boldsymbol{\nu}'}T_{\mathbf{0},\boldsymbol{\nu}'} && \text{(B.11)} \end{aligned}$$

The right-hand side of the above equation is complex, but we can rewrite the above equation in terms of purely real quantities. Using the property given in Eq. (B.3), we obtain

$$T_{\mathbf{k},\mathbf{k}'} = \frac{\delta_{\mathbf{k},\mathbf{k}'}}{2} \sum_{\boldsymbol{\nu}'} e^{i\frac{2\pi}{m}\mathbf{k}'\cdot\boldsymbol{\nu}'} [T_{\mathbf{0},\boldsymbol{\nu}'} + T_{\mathbf{0},\mathbf{M}-\boldsymbol{\nu}'}] \tag{B.12}$$

By splitting the right-hand side of the above expression into the sum of two terms and performing a change of variable $\boldsymbol{\mu} = \mathbf{M} - \boldsymbol{\nu}'$ in the second term we arrive at

$$\begin{aligned} T_{\mathbf{k},\mathbf{k}'} &= \frac{\delta_{\mathbf{k},\mathbf{k}'}}{2} \sum_{\boldsymbol{\mu}} \left[e^{i\frac{2\pi}{m}\mathbf{k}'\cdot\boldsymbol{\mu}} + e^{i\frac{2\pi}{m}\mathbf{k}'\cdot(\mathbf{M}-\boldsymbol{\mu})} \right] T_{\mathbf{0},\boldsymbol{\mu}} && \text{(B.13)} \\ &= \delta_{\mathbf{k},\mathbf{k}'} \sum_{\boldsymbol{\mu}} \cos\left(\frac{2\pi}{m}\mathbf{k}'\cdot\boldsymbol{\mu}\right) T_{\mathbf{0},\boldsymbol{\mu}} && \text{(B.14)} \end{aligned}$$

Which is purely real. Similarly, we find that the overlap between symmetry-adapted orbitals is

$$S_{\mathbf{k},\mathbf{k}'} = \delta_{\mathbf{k},\mathbf{k}'} \sum_{\boldsymbol{\mu}} \cos\left(\frac{2\pi}{m}\mathbf{k}'\cdot\boldsymbol{\mu}\right) S_{\mathbf{0},\boldsymbol{\mu}} \tag{B.15}$$

B.2 Two-electron Integrals

The same properties discussed for the one-electron integrals can be made for the two-electron integrals, where we have the following symmetry relations,

$$\begin{aligned} \langle \boldsymbol{\mu}\boldsymbol{\nu}|\boldsymbol{\rho}\boldsymbol{\sigma}\rangle &= \langle \boldsymbol{\mu}+\boldsymbol{\delta}, \boldsymbol{\nu}+\boldsymbol{\delta}|\boldsymbol{\rho}+\boldsymbol{\delta}, \boldsymbol{\sigma}+\boldsymbol{\delta}\rangle && \text{(B.16)} \\ \langle \boldsymbol{\mu}\boldsymbol{\nu}|\boldsymbol{\rho}\boldsymbol{\sigma}\rangle &= \langle \mathbf{M}-\boldsymbol{\mu}, \mathbf{M}-\boldsymbol{\nu}|\mathbf{M}-\boldsymbol{\rho}, \mathbf{M}-\boldsymbol{\sigma}\rangle && \text{(B.17)} \end{aligned}$$

We can now use a similar strategy as the previous subsection for the two-electron integrals. They can be expressed in terms of the symmetry-adapted orbitals according to

$$\langle \mathbf{k}\mathbf{k}'|\mathbf{k}''\mathbf{k}'''\rangle = \frac{1}{m^{2d}} \sum_{\boldsymbol{\mu}\boldsymbol{\nu}\boldsymbol{\rho}\boldsymbol{\sigma}} e^{-i\frac{2\pi}{m}[\mathbf{k}\cdot\boldsymbol{\mu}+\mathbf{k}'\cdot\boldsymbol{\nu}-\mathbf{k}''\cdot\boldsymbol{\rho}-\mathbf{k}'''\cdot\boldsymbol{\sigma}]} \langle \boldsymbol{\mu}\boldsymbol{\nu}|\boldsymbol{\rho}\boldsymbol{\sigma}\rangle \tag{B.18}$$

Making use of the symmetry relation given in Eq. (B.16) and setting $\boldsymbol{\delta}$ as $-\boldsymbol{\mu}$ we can rewrite the above equation as

$$\langle \mathbf{k}\mathbf{k}'|\mathbf{k}''\mathbf{k}'''\rangle = \sum_{\boldsymbol{\mu}\boldsymbol{\nu}\boldsymbol{\rho}\boldsymbol{\sigma}} e^{-i\frac{2\pi}{m}[\mathbf{k}\cdot\boldsymbol{\mu}+\mathbf{k}'\cdot\boldsymbol{\nu}-\mathbf{k}''\cdot\boldsymbol{\rho}-\mathbf{k}'''\cdot\boldsymbol{\sigma}]} \langle \mathbf{0}, \boldsymbol{\nu}-\boldsymbol{\mu}|\boldsymbol{\rho}-\boldsymbol{\mu}, \boldsymbol{\sigma}-\boldsymbol{\mu}\rangle \tag{B.19}$$

$$= \frac{1}{m^{2d}} \sum_{\boldsymbol{\mu}} e^{-i\frac{2\pi}{m}[\mathbf{k}+\mathbf{k}'-\mathbf{k}''-\mathbf{k}''')\cdot\boldsymbol{\mu}]} \sum_{\boldsymbol{\nu}\boldsymbol{\rho}\boldsymbol{\sigma}} e^{-i\frac{2\pi}{m}\left(\mathbf{k}'\cdot(\boldsymbol{\nu}-\boldsymbol{\mu})-\mathbf{k}''\cdot(\boldsymbol{\rho}-\boldsymbol{\mu})-\mathbf{k}''\cdot(\boldsymbol{\sigma}-\boldsymbol{\mu})\right)}$$

$$\times \langle \mathbf{0}, \boldsymbol{\nu}-\boldsymbol{\mu}|\boldsymbol{\rho}-\boldsymbol{\mu}, \boldsymbol{\sigma}-\boldsymbol{\mu}\rangle \tag{B.20}$$

Performing the following changes of variables $\boldsymbol{\nu}' = \boldsymbol{\nu}-\boldsymbol{\mu}$, $\boldsymbol{\rho}' = \boldsymbol{\rho}-\boldsymbol{\mu}$ and $\boldsymbol{\sigma}' = \boldsymbol{\sigma}-\boldsymbol{\mu}$ we arrive at

$$\langle \mathbf{k}\mathbf{k}'|\mathbf{k}''\mathbf{k}'''\rangle = \frac{1}{m^{2d}} \sum_{\boldsymbol{\mu}} e^{-i\frac{2\pi}{m}[\mathbf{k}+\mathbf{k}'-\mathbf{k}''-\mathbf{k}''']\cdot\boldsymbol{\mu}} \sum_{\boldsymbol{\nu}'\boldsymbol{\rho}'\boldsymbol{\sigma}'} e^{-i\frac{2\pi}{m}(\mathbf{k}'\cdot\boldsymbol{\nu}'-\mathbf{k}''\cdot\boldsymbol{\rho}'-\mathbf{k}''\cdot\boldsymbol{\sigma}')}$$

$$\times \langle \mathbf{0}, \boldsymbol{\nu}'|\boldsymbol{\rho}', \boldsymbol{\sigma}'\rangle \tag{B.21}$$

$$= \frac{1}{m^{d}} \delta_{\mathbf{k}+\mathbf{k}'-\mathbf{k}''-\mathbf{k}''} \sum_{\boldsymbol{\nu}'\boldsymbol{\rho}'\boldsymbol{\sigma}'} e^{-i\frac{2\pi}{m}(\mathbf{k}'\cdot\boldsymbol{\nu}'-\mathbf{k}''\cdot\boldsymbol{\rho}'-\mathbf{k}''\cdot\boldsymbol{\sigma}')} \langle \mathbf{0}, \boldsymbol{\nu}'|\boldsymbol{\rho}', \boldsymbol{\sigma}'\rangle \tag{B.22}$$

Using Eq. (B.17) we can now rewrite the above expression in purely real quantities. We obtain

$$\langle \mathbf{k}\mathbf{k}'|\mathbf{k}''\mathbf{k}'''\rangle = \frac{1}{2m^{d}} \delta_{\mathbf{k}+\mathbf{k}'-\mathbf{k}''-\mathbf{k}''} \sum_{\boldsymbol{\nu}'\boldsymbol{\rho}'\boldsymbol{\sigma}'} e^{-i\frac{2\pi}{m}(\mathbf{k}'\cdot\boldsymbol{\nu}'-\mathbf{k}''\cdot\boldsymbol{\rho}'-\mathbf{k}''\cdot\boldsymbol{\sigma}')}$$

$$\times \left[\langle \mathbf{0}, \boldsymbol{\nu}'|\boldsymbol{\rho}', \boldsymbol{\sigma}'\rangle + \langle \mathbf{0}, \mathbf{M}-\boldsymbol{\nu}'|\mathbf{M}-\boldsymbol{\rho}', \mathbf{M}-\boldsymbol{\sigma}'\rangle\right] \tag{B.23}$$

Splitting the right-hand side of the above expression into the sum of two terms and performing the changes of variable $\boldsymbol{\nu} = \mathbf{M}-\boldsymbol{\nu}'$, $\boldsymbol{\rho} = \mathbf{M}-\boldsymbol{\rho}'$

and $\boldsymbol{\sigma} = \mathbf{M} - \boldsymbol{\sigma}'$ we arrive at the final expression for the 2-electron integrals expressed in the symmetry-adapted basis,

$$\langle \mathbf{k}\mathbf{k}' | \mathbf{k}''\mathbf{k}''' \rangle = \frac{1}{2m^d} \delta_{\mathbf{k}+\mathbf{k}'-\mathbf{k}''-\mathbf{k}''} \sum_{\boldsymbol{\nu}\boldsymbol{\rho}\boldsymbol{\sigma}} \left[e^{-i\frac{2\pi}{m}(\mathbf{k}'\cdot\boldsymbol{\nu}'-\mathbf{k}''\cdot\boldsymbol{\rho}'-\mathbf{k}''\cdot\boldsymbol{\sigma}')} \right. \tag{B.24}$$

$$\left. + \, e^{-i\frac{2\pi}{m}(\mathbf{k}'\cdot(\mathbf{M}-\boldsymbol{\nu})-\mathbf{k}''\cdot(\mathbf{M}-\boldsymbol{\rho})-\mathbf{k}''\cdot(\mathbf{M}-\boldsymbol{\sigma}))} \right] \langle \mathbf{0}, \boldsymbol{\nu} | \boldsymbol{\rho}, \boldsymbol{\sigma} \rangle \tag{B.25}$$

$$= \frac{1}{m^d} \delta_{\mathbf{k}+\mathbf{k}'-\mathbf{k}''-\mathbf{k}''} \sum_{\boldsymbol{\nu}\boldsymbol{\rho}\boldsymbol{\sigma}} \cos \left[\frac{2\pi}{m} \left(\mathbf{k}' \cdot \boldsymbol{\nu} - \mathbf{k}'' \cdot \boldsymbol{\rho} - \mathbf{k}'' \cdot \boldsymbol{\sigma} \right) \right] \langle \mathbf{0}, \boldsymbol{\nu} | \boldsymbol{\rho}, \boldsymbol{\sigma} \rangle \tag{B.26}$$

Which is purely real.

Bibliography

[1] E. Wigner. On the interaction of electrons in metals. *Phys. Rev.*, 46:1002–1011, Dec 1934. `doi:10.1103/PhysRev.46.1002`. (Cited on pages 1 and 89.)

[2] C. C. Grimes and G. Adams. Evidence for a liquid-to-crystal phase transition in a classical, two-dimensional sheet of electrons. *Phys. Rev. Lett.*, 42:795–798, Mar 1979. `doi:10.1103/PhysRevLett.42.795`. (Cited on pages 1 and 89.)

[3] I. Shapir, A. Hamo, S. Pecker, C. P. Moca, Ö. Legeza, G. Zarand, and S. Ilani. Imaging the electronic Wigner crystal in one dimension. *Science*, 364(6443):870–875, 2019. `doi:10.1126/science.aat0905`. (Cited on pages 1 and 89.)

[4] R. Egger, W. Häusler, C. H. Mak, and H. Grabert. Crossover from Fermi Liquid to Wigner Molecule Behavior in Quantum Dots. *Phys. Rev. Lett.*, 82:3320–3323, Apr 1999. `doi:10.1103/PhysRevLett.82.3320`. (Cited on pages 1 and 89.)

[5] Jerzy Cioslowski and Marcin Buchowiecki. Wigner molecules: Natural orbitals of strongly correlated two-electron harmonium. *J. Chem. Phys.*, 125(6):064105, 2006. `doi:10.1063/1.2222360`. (Cited on pages 1 and 89.)

[6] C. Ellenberger, T. Ihn, C. Yannouleas, U. Landman, K. Ensslin, D. Driscoll, and A. C. Gossard. Excitation spectrum of two correlated electrons in a lateral quantum dot with negligible zeeman splitting. *Phys. Rev. Lett.*, 96:126806, Mar 2006. URL: `https://link.aps.org/doi/10.1103/PhysRevLett.96.126806`, `doi:10.1103/PhysRevLett.96.126806`. (Cited on pages 1 and 89.)

[7] Constantine Yannouleas and Uzi Landman. Symmetry breaking and quantum correlations in finite systems: studies of quantum dots and ultracold bose gases and related nuclear and chemical methods. *Rep. Prog. Phys.*, 70(12):2067–2148, nov 2007. `doi:10.1088/0034-4885/70/12/r02`. (Cited on pages 1 and 89.)

[8] Jerzy Cioslowski and Krzysztof Strasburger. Harmonium atoms at weak confinements: The formation of the Wigner molecules. *J. Chem. Phys.*, 146(4):044308, 2017. `doi:10.1063/1.4974273`. (Cited on pages 1 and 89.)

[9] Alejandro Diaz-Marquez, Stefano Battaglia, Gian Luigi Bendazzoli, Stefano Evangelisti, Thierry Leininger, and J. A. Berger. Signatures of wigner localization in one-dimensional systems. *J. Chem. Phys.*, 148(12):124103, 2018. `doi:10.1063/1.5017118`. (Cited on pages 1, 2, 35, 39, 44, 46, 47, 51, 81, 89, 90 and 112.)

[10] Miguel Escobar Azor, Léa Brooke, Stefano Evangelisti, Thierry Leininger, Pierre-François Loos, Nicolas Suaud, and J A Berger. A Wigner molecule at extremely low densities: a numerically exact study. *SciPost Phys. Core*, 1(1):001, 2019. URL: `https://scipost.org/10.21468/SciPostPhysCore.1.1.001`, `doi:10.21468/SciPostPhysCore.1.1.001`. (Cited on pages 1, 71, 77 and 89.)

[11] S. Pecker, F. Kuemmeth, A. Secchi, M. Rontani, D.C. Ralph, P. L. McEuen, and S. Ilani. Observation and spectroscopy of a two-electron Wigner molecule in an ultraclean carbon nanotube. *Nat. Phys.*, 9(9):576–581, SEP 2013. `doi:10.1038/NPHYS2692`. (Cited on pages 1 and 89.)

[12] Fergus J. M. Rogers, Caleb J. Ball, and Pierre-François Loos. Symmetry-broken local-density approximation for one-dimensional systems. *Phys. Rev. B*, 93:235114, Jun 2016. URL: `https://link.aps.org/doi/10.1103/PhysRevB.93.235114`, `doi:10.1103/PhysRevB.93.235114`. (Cited on page 2.)

[13] Fergus J. M. Rogers and Pierre-François Loos. Excited-state wigner crystals. *The Journal of Chemical Physics*, 146(4):044114, 2017. `arXiv:https://doi.org/10.1063/1.4974839`, `doi:10.1063/1.4974839`. (Cited on page 2.)

[14] P. Hohenberg and W. Kohn. Inhomogeneous electron gas. *Phys. Rev.*, 136(3B):B864–B871, Nov 1964. `doi:10.1103/PhysRev.136.B864`. (Cited on page 2.)

[15] W. Kohn and L. J. Sham. Self-consistent equations including exchange and correlation effects. *Phys. Rev.*, 140(4A):A1133–A1138, Nov 1965. `doi:10.1103/PhysRev.140.A1133`. (Cited on page 2.)

[16] Michael Seidl. Strong-interaction limit of density-functional theory. *Phys. Rev. A*, 60:4387–4395, Dec 1999. `doi:10.1103/PhysRevA.60.4387`. (Cited on page 2.)

[17] Michael Seidl, John P. Perdew, and Mel Levy. Strictly correlated electrons in density-functional theory. *Phys. Rev. A*, 59:51–54, Jan 1999. `doi:10.1103/PhysRevA.59.51`. (Cited on page 2.)

[18] Francesc Malet and Paola Gori-Giorgi. Strong Correlation in Kohn-Sham Density Functional Theory. *Phys. Rev. Lett.*, 109:246402, Dec 2012. `doi:10.1103/PhysRevLett.109.246402`. (Cited on page 2.)

[19] Francesc Malet, André Mirtschink, Jonas C. Cremon, Stephanie M. Reimann, and Paola Gori-Giorgi. Kohn-sham density functional theory for quantum wires in arbitrary correlation regimes. *Phys. Rev. B*, 87:115146, Mar 2013. `doi:10.1103/PhysRevB.87.115146`. (Cited on page 2.)

[20] Christian B. Mendl, Francesc Malet, and Paola Gori-Giorgi. Wigner localization in quantum dots from kohn-sham density functional theory without symmetry breaking. *Phys. Rev. B*, 89:125106, Mar 2014. URL: `https://link.aps.org/doi/10.1103/PhysRevB.89.125106`, `doi:10.1103/PhysRevB.89.125106`. (Cited on page 2.)

[21] Nicolas Tavernier, Gian Luigi Bendazzoli, Véronique Brumas, Stefano Evangelisti, and J. A. Berger. Clifford boundary conditions: A simple direct-sum evaluation of madelung constants. *The Journal of Physical Chemistry Letters*, 11(0):7090–7095, 2020. `doi:10.1021/acs.jpclett.0c01684`. (Cited on pages 2, 7, 90 and 91.)

[22] Douglas Achan, Lou Massa, and Viraht Sahni. Wigner high-electron-correlation regime of nonuniform density systems: A quantal-density-functional-theory study. *Physical Review A*, 90(2):022502, 2014. (Cited on pages 3 and 90.)

[23] Paola Gori-Giorgi and Andreas Savin. Study of the discontinuity of the exchange-correlation potential in an exactly soluble case. *International Journal of Quantum Chemistry*, 109(11):2410–2415, 2009. (Cited on pages 3 and 90.)

[24] Wuming Zhu and SB Trickey. Exact density functionals for two-electron systems in an external magnetic field. *The Journal of chemical physics*, 125(9):094317, 2006. (Cited on pages 3 and 90.)

[25] M Pedersen Lohne, Gaute Hagen, M Hjorth-Jensen, S Kvaal, and F Pederiva. Ab initio computation of the energies of circular quantum dots. *Physical Review B*, 84(11):115302, 2011. (Cited on pages 3 and 90.)

[26] JL Lebowitz and Elliott H Lieb. Existence of thermodynamics for real matter with coulomb forces. *Physical Review Letters*, 22(13):631, 1969. (Cited on page 4.)

[27] T. Helgaker, P. Jørgensen, and J. Olsen. *Molecular Electronic-Structure Theory*. John Wiley & Sons, Ltd., 2000. (Cited on pages 7, 16 and 91.)

[28] A. Szabo and N. S. Ostlund. *Modern quantum chemistry*. McGraw-Hill, New York, 1989. (Cited on pages 7 and 91.)

[29] R. A. Schwartz. *Mostly Surfaces*. American Mathematical Society, 2011. (Cited on page 8.)

[30] Walter William Rouse Ball. *A short account of the history of mathematics*. Courier Corporation, 1960. (Cited on page 8.)

[31] Henri Poincaré. Poincaré's review of hilbert's "foundations of geometry.". *Bulletin of the American Mathematical Society*, 10(1):1–23, 1903. (Cited on page 9.)

[32] J. C. Slater and G. F. Koster. Simplified LCAO Method for the Periodic Potential Problem. *Phys. Rev.*, 94:1498–1524, Jun 1954. URL: `https://link.aps.org/doi/10.1103/PhysRev.94.1498`, `doi:10.1103/PhysRev.94.1498`. (Cited on page 14.)

[33] Jin Qian, Ethan J. Crumlin, and David Prendergast. Efficient basis sets for core-excited states motivated by slater's rules. *Phys. Chem. Chem. Phys.*, 24:2243–2250, 2022. URL: `http://dx.doi.org/10.1039/D1CP03931H`, `doi:10.1039/D1CP03931H`. (Cited on page 14.)

[34] M Coşkun and M Ertürk. Applicability of noninteger bessel type orbital basis sets: Numerical and analytical approaches, 2022. `doi:10.21203/rs.3.rs-2060524/v1`. (Cited on page 14.)

[35] Hong-Zhou Ye and Timothy C. Berkelbach. Correlation-Consistent Gaussian Basis Sets for Solids Made Simple. *Journal of Chemical Theory and Computation*, 18(3):1595–1606, 2022. PMID: 35192359. `arXiv:https://doi.org/10.1021/acs.jctc.1c01245`, `doi:10.1021/acs.jctc.1c01245`. (Cited on page 14.)

[36] John C Slater. Atomic shielding constants. *Physical Review*, 36(1):57, 1930. (Cited on page 14.)

[37] S Francis Boys. Electronic wave functions I. A general method of calculation for the stationary states of any molecular system. *Proceedings of the Royal Society of London. Series A. Mathematical and Physical Sciences*, 200(1063):542–554, 1950. (Cited on pages 14, 18 and 53.)

[38] Richard M Martin. *Electronic structure: basic theory and practical methods*. Cambridge university press, 2020. (Cited on page 14.)

[39] Philip E Hoggan, Marıa Belén Ruiz, and T Özdogan. Molecular integrals over slater-type orbitals. From pioneers to recent developments. *Quantum Frontiers ofAtoms and Molecules*, pages 64–90, 2011. (Cited on page 15.)

[40] James Emil Avery and John Scales Avery. Molecular integrals for exponential-type orbitals using hyperspherical harmonics. In *Advances in Quantum Chemistry*, volume 70, pages 265–324. Elsevier, 2015. (Cited on page 15.)

[41] G. te Velde, F. M. Bickelhaupt, E. J. Baerends, C. Fonseca Guerra, S. J. A. van Gisbergen, J. G. Snijders, and T. Ziegler. Chemistry with ADF. *J. Comput. Chem.*, 22(9):931–967, 2001. URL: `http://dx.doi.org/10.1002/jcc.1056`, `doi:10.1002/jcc.1056`. (Cited on page 15.)

[42] H. Bernhard Schlegel and Michael J. Frisch. Transformation between cartesian and pure spherical harmonic gaussians. *International Journal of Quantum Chemistry*, 54(2):83–87, 1995. URL: `https://onlinelibrary.wiley.com/doi/abs/10.1002/qua.560540202`, `arXiv:https://onlinelibrary.wiley.com/doi/pdf/10.1002/qua.560540202`, `doi:10.1002/qua.560540202`. (Cited on page 16.)

[43] J Grant Hill. Gaussian basis sets for molecular applications. *International Journal of Quantum Chemistry*, 113(1):21–34, 2013. (Cited on page 19.)

[44] Thom H. Dunning. Gaussian basis sets for use in correlated molecular calculations I. The atoms boron through neon and hydrogen. *The Journal of Chemical Physics*, 90(2):1007–1023, 1989. `arXiv:https://doi.org/10.1063/1.456153`, `doi:10.1063/1.456153`. (Cited on page 19.)

[45] Frank Jensen. Polarization consistent basis sets: Principles. *The Journal of Chemical Physics*, 115(20):9113–9125, 2001. `arXiv:https://doi.org/10.1063/1.1413524`, `doi:10.1063/1.1413524`. (Cited on page 19.)

[46] Jussi Lehtola, Pekka Manninen, Mikko Hakala, and Keijo Hämäläinen. Completeness-optimized basis sets: Application to ground-state electron momentum densities. *The Journal of Chemical Physics*, 137(10):104105, 2012. `arXiv:https://doi.org/10.1063/1.4749272`, `doi:10.1063/1.4749272`. (Cited on page 19.)

[47] Susi Lehtola, Pekka Manninen, Mikko Hakala, and Keijo Hämäläinen. Contraction of completeness-optimized basis sets: Application to ground-state electron momentum densities. *The Journal of Chemical Physics*, 138(4):044109, 2013. `arXiv:https://doi.org/10.1063/1.4788635`, `doi:10.1063/1.4788635`. (Cited on page 19.)

[48] Eduard Matito, Jacek Kobus, and Jacek Styszyński. Bond centred functions in relativistic and non-relativistic calculations for diatomics. *Chemical Physics*, 321(3):277–284, 2006. URL: `https://www.sciencedirect.com/science/article/pii/S0301010405003733`, `doi:10.1016/j.chemphys.2005.08.023`. (Cited on page 19.)

[49] Miroslav Melicherčík, Michal Pitoňák, Vladimír Kellö, Pavel Hobza, and Pavel Neogrády. Off-Center Gaussian Functions, an alternative atomic orbital basis set for accurate noncovalent interaction calculations of large systems. *Journal of Chemical Theory and Computation*, 9(12):5296–5304, 2013. PMID: 26592267. `arXiv:https://doi.org/10.1021/ct400692b`, `doi:10.1021/ct400692b`. (Cited on page 20.)

[50] Miroslav Melicherčík, Denisa Suchá, Pavel Neogrády, and Michal Pitoňák. Off-center Gaussian functions: Applications toward larger basis sets, post-second-order correlation treatment, and truncated virtual orbital space in investigations of non-covalent interactions. *International Journal of Quantum Chemistry*, 118(14):e25580, 2018. URL: `https://onlinelibrary.wiley.com/doi/abs/10.1002/qua.25580`, `arXiv:https://onlinelibrary.wiley.com/doi/pdf/10.1002/qua.25580`, `doi:10.1002/qua.25580`. (Cited on page 20.)

[51] Linda M Haines, John N Murrell, BJ Ralston, and DJ Woodnutt. Gaussian cell model for molecular orbitals. *Journal of the Chemical Society, Faraday Transactions 2: Molecular and Chemical Physics*, 70:1794–1800, 1974. (Cited on page 20.)

[52] B.J. Ralston and S. Wilson. Distributed basis sets of s-type Gaussian functions in molecular electronic structure calculations. The Gaussian cell model revisted. *Journal of Molecular Structure: THEOCHEM*, 341(1):115–121, 1995. URL: `https://www.sciencedirect.com/science/article/pii/016612809504204J`, `doi:10.1016/0166-1280(95)04204-J`. (Cited on page 20.)

[53] S. Wilson. Distributed basis sets of s-type Gaussian functions in molecular electronic structure calculations. Part 2. The Gaussian cell model. *Journal of Molecular Structure: THEOCHEM*, 357(1):37–48, 1995. URL: `https://www.sciencedirect.com/science/article/pii/0166128095042717`, `doi:10.1016/0166-1280(95)04271-7`. (Cited on page 20.)

[54] S. Wilson. Distributed basis sets of s-type Gaussian functions for molecular electronic structure calculations: Applications of the Gaussian cell model to one-electron polycentric linear molecular systems. *International Journal of Quantum Chemistry*, 60(1):47–57, 1996. URL: `https://onlinelibrary.wiley.com/doi/abs/10.1002/`, `doi:10.1002/(SICI)1097-461X(1996)60:1<47::AID-QUA5>3.0.CO;2-5`. (Cited on page 20.)

[55] Attila Szabo and Neil S Ostlund. *Modern quantum chemistry: introduction to advanced electronic structure theory*. Courier Corporation, 2012. (Cited on pages 22, 27, 55, 98 and 100.)

[56] Ali Tatar, Loïc Salles, Alexander Haslam, and Christoph Schwingshackl. *Comparison of Computational Generalized and Standard Eigenvalue Solutions of Rotating Systems*, pages 187–194. 01 2019. `doi:10.1007/978-3-319-74700-2_19`. (Cited on page 23.)

[57] E. Anderson, Z. Bai, J. Dongarra, A. Greenbaum, A. McKenney, J. Du Croz, S. Hammarling, J. Demmel, C. Bischof, and D. Sorensen. Lapack: A portable linear algebra library for high-performance computers. In *Proceedings of the 1990 ACM/IEEE Conference on Supercomputing*, Supercomputing '90, page 2–11, Washington, DC, USA, 1990. IEEE Computer Society Press. (Cited on page 24.)

[58] Ward Cheney and David R. Kincaid. *Linear Algebra: Theory and Applications*. Jones and Bartlett Publishers, Inc., USA, 1st edition, 2008. (Cited on page 24.)

[59] I. Mayer. On löwdin's method of symmetric orthogonalization. *International Journal of Quantum Chemistry*, 90(1):63–65, 2002. URL: `https://onlinelibrary.wiley.com/doi/abs/10.1002/qua.981`, `doi:10.1002/qua.981`. (Cited on page 24.)

[60] A. Ramesh Naidu and Vipin Srivastava. Löwdin's canonical orthogonalization: Getting round the restriction of linear independence. *International Journal of Quantum Chemistry*, 99(6):882–888, 2004. URL: `https://onlinelibrary.wiley.com/doi/abs/10.1002/qua.20136`, `doi:10.1002/qua.20136`. (Cited on page 24.)

[61] Léa Brooke, Alejandro Diaz-Marquez, Stefano Evangelisti, Thierry Leininger, Pierre-François Loos, Nicolas Suaud, and J. A. Berger. Distributed Gaussian orbitals for the description of electrons in an external potential. *J. Mol. Model.*, 24(8):216, Jul 2018. `doi:10.1007/s00894-018-3749-x`. (Cited on pages 24, 35 and 43.)

[62] Celestino Angeli, Gian Luigi Bendazzoli, Stefano Evangelisti, and J. A. Berger. The localization spread and polarizability of rings and periodic chains. *arXiv:2105.08174*, 2021. (Cited on pages 26, 54 and 99.)

[63] Peter M. W. Gill, Pierre-François Loos, and Davids Agboola. Basis functions for electronic structure calculations on spheres. *The Journal of Chemical Physics*, 141(24):244102, 2014. `arXiv:https://doi.org/10.1063/1.4903984`, `doi:10.1063/1.4903984`. (Cited on page 30.)

[64] Pierre-François Loos and Peter M. W. Gill. Exact wave functions of two-electron quantum rings. *Phys. Rev. Lett.*, 108:083002, Feb 2012. URL: `https://link.aps.org/doi/10.1103/PhysRevLett.108.083002`, `doi:10.1103/PhysRevLett.108.083002`. (Cited on pages 35 and 100.)

[65] Pierre-François Loos and Peter M. W. Gill. Uniform electron gases. i. electrons on a ring. *The Journal of Chemical Physics*, 138(16):164124, 2013. `arXiv:https://doi.org/10.1063/1.4802589`, `doi:10.1063/1.4802589`. (Cited on pages 35 and 100.)

[66] Pierre-François Loos, Caleb J. Ball, and Peter M. W. Gill. Uniform electron gases. ii. the generalized local density approximation in one dimension. *The Journal of Chemical Physics*, 140(18):18A524, 2014. `arXiv:https://doi.org/10.1063/1.4867910`, `doi:10.1063/1.4867910`. (Cited on pages 35 and 100.)

[67] Vincent Tognetti and Pierre-François Loos. Natural occupation numbers in two-electron quantum rings. *The Journal of Chemical Physics*, 144(5):054108, 2016. `arXiv:https://doi.org/10.1063/1.4940919`, `doi:10.1063/1.4940919`. (Cited on pages 35 and 100.)

[68] N. D. Drummond, Z. Radnai, J. R. Trail, M. D. Towler, and R. J. Needs. Diffusion quantum monte carlo study of three-dimensional wigner crystals. *Phys. Rev. B*, 69:085116, Feb 2004. URL: `https://link.aps.org/doi/10.1103/PhysRevB.69.085116`, `doi:10.1103/PhysRevB.69.085116`. (Cited on pages 38, 57, 71 and 77.)

[69] Raffaele Resta and Sandro Sorella. Electron localization in the insulating state. *Phys. Rev. Lett.*, 82:370–373, Jan 1999. URL: `https://link.aps.org/doi/10.1103/PhysRevLett.82.370`, `doi:10.1103/PhysRevLett.82.370`. (Cited on pages 39 and 102.)

[70] Claudia Sgiarovello, Maria Peressi, and Raffaele Resta. Electron localization in the insulating state: Application to crystalline semiconductors. *Phys. Rev. B*, 64:115202, Aug 2001. URL: `https://link.aps.`

org/doi/10.1103/PhysRevB.64.115202, doi:10.1103/PhysRevB.64.115202. (Cited on pages 39 and 102.)

[71] Raffaele Resta. Kohn's theory of the insulating state: A quantum-chemistry viewpoint. *The Journal of Chemical Physics*, 124(10):104104, 2006. arXiv:https://doi.org/10.1063/1.2176604, doi:10.1063/1.2176604. (Cited on pages 39 and 102.)

[72] Raffaele Resta. Electron localization in the quantum hall regime. *Phys. Rev. Lett.*, 95:196805, Nov 2005. doi:10.1103/PhysRevLett.95.196805. (Cited on pages 39 and 102.)

[73] Ivo Souza, Tim Wilkens, and Richard M. Martin. Polarization and localization in insulators: Generating function approach. *Phys. Rev. B*, 62:1666–1683, Jul 2000. doi:10.1103/PhysRevB.62.1666. (Cited on pages 39 and 102.)

[74] Walter Kohn. Theory of the insulating state. *Phys. Rev.*, 133:A171–A181, Jan 1964. URL: https://link.aps.org/doi/10.1103/PhysRev.133.A171, doi:10.1103/PhysRev.133.A171. (Cited on pages 39 and 102.)

[75] EK Kudinov. Difference between the insulating and conducting states. *Fizika Tvergodo Tela*, 33(8):2306–2315, 1991. (Cited on pages 39 and 102.)

[76] Valentina Vetere, Antonio Monari, Gian Luigi Bendazzoli, Stefano Evangelisti, and Beate Paulus. Full configuration interaction study of the metal-insulator transition in model systems: Li_N linear chains (N=2,4,6,8). *The Journal of Chemical Physics*, 128(2):024701, 2008. arXiv:https://doi.org/10.1063/1.2822286, doi:10.1063/1.2822286. (Cited on page 39.)

[77] Gian Luigi Bendazzoli, Stefano Evangelisti, and Antonio Monari. Full-configuration-interaction study of the metal-insulator transition in a model system: H_n linear chains n=4, 6,. . . , 16. *International Journal of Quantum Chemistry.* (Cited on page 39.)

[78] Emmanuel Giner, Gian Luigi Bendazzoli, Stefano Evangelisti, and Antonio Monari. Full-configuration-interaction study of the metal-insulator transition in model systems: Peierls dimerization in H_n rings and chains. *J. Chem. Phys.*, 138(7):074315, 2013. doi:10.1063/1.4792197. (Cited on page 39.)

[79] Antonio Monari, Gian Luigi Bendazzoli, and Stefano Evangelisti. The metal-insulator transition in dimerized Hückel chains. *J. Chem. Phys.*, 129(13):134104, 2008. doi:10.1063/1.2987702. (Cited on page 39.)

[80] Stefano Evangelisti, Gian Luigi Bendazzoli, and Antonio Monari. Electron localizability and polarizability in tight-binding graphene nanostructures. *Theor. Chem. Acc.*, 126(3):257–263, Jun 2010. doi:10.1007/s00214-009-0700-3. (Cited on page 39.)

[81] Gian Luigi Bendazzoli, Stefano Evangelisti, Antonio Monari, and Raffaele Resta. Kohn's localization in the insulating state: One-dimensional lattices, crystalline versus disordered. *J. Chem. Phys*, 133(6):064703, 2010. `doi:10.1063/1.3467877`. (Cited on page 39.)

[82] Gian Luigi Bendazzoli, Stefano Evangelisti, and Antonio Monari. Asymptotic analysis of the localization spread and polarizability of 1-d noninteracting electrons. *Int. J. Quantum Chem.*, 112(3):653–664, 2012. `doi:10.1002/qua.23036`. (Cited on page 39.)

[83] Muammar El Khatib, Oriana Brea, Edoardo Fertitta, Gian Luigi Bendazzoli, Stefano Evangelisti, Thierry Leininger, and Beate Paulus. Spin delocalization in hydrogen chains described with the spin-partitioned total position-spread tensor. *Theor. Chem. Acc.*, 134(3):29, Feb 2015. `doi:10.1007/s00214-015-1625-7`. (Cited on page 39.)

[84] Edoardo Fertitta, Muammar El Khatib, Gian Luigi Bendazzoli, Beate Paulus, Stefano Evangelisti, and Thierry Leininger. The spin-partitioned total position-spread tensor: An application to heisenberg spin chains. *J. Chem. Phys.*, 143(24):244308, 2015. `doi:10.1063/1.4936585`. (Cited on page 39.)

[85] Angel Martín Pendás, José Manuel Guevara-Vela, Daniel Menéndez Crespo, Aurora Costales, and Evelio Francisco. An unexpected bridge between chemical bonding indicators and electrical conductivity through the localization tensor. *Phys. Chem. Chem. Phys.*, 19:1790–1797, 2017. `doi:10.1039/C6CP07617C`. (Cited on page 39.)

[86] Sara Gil-Guerrero, Nicolás Ramos-Berdullas, Ángel Martín Pendás, Evelio Francisco, and Marcos Mandado. Anti-ohmic single molecule electron transport: is it feasible? *Nanoscale Adv.*, 1:1901–1913, 2019. `doi:10.1039/C8NA00384J`. (Cited on page 39.)

[87] K. J. H. Giesbertz and R. van Leeuwen. Natural occupation numbers: When do they vanish? *J. Chem. Phys.*, 139(10):104109, 2013. `doi:10.1063/1.4820419`. (Cited on pages 41, 71 and 102.)

[88] S. Di Sabatino, J. A. Berger, L. Reining, and P. Romaniello. Reduced density-matrix functional theory: Correlation and spectroscopy. *The Journal of Chemical Physics*, 143(2):024108, 2015. `arXiv:https://doi.org/10.1063/1.4926327`, `doi:10.1063/1.4926327`. (Cited on pages 41 and 102.)

[89] Paola Gori-Giorgi and Paul Ziesche. Momentum distribution of the uniform electron gas: Improved parametrization and exact limits of the cumulant expansion. *Phys. Rev. B*, 66:235116, Dec 2002. `doi:10.1103/PhysRevB.66.235116`. (Cited on pages 41 and 102.)

[90] Estefania Alves, Gian Luigi Bendazzoli, Stefano Evangelisti, and J. Arjan Berger. Accurate ground-state energies of Wigner crystals from a simple real-space approach. *Phys. Rev. B*, 103:245125,

Jun 2021. URL: `https://link.aps.org/doi/10.1103/PhysRevB.103.245125`, `doi:10.1103/PhysRevB.103.245125`. (Cited on pages 59 and 75.)

[91] Jerzy Cioslowski and Krzysztof Strasburger. Angular-momentum extrapolations to the complete basis set limit: Why and when they work. *J. Chem. Theory Comput.*, 17(6):3403–3413, 2021. PMID: 34003646. `doi:10.1021/acs.jctc.1c00202`. (Cited on page 62.)

[92] Léa Brooke, Alejandro Diaz-Marquez, Stefano Evangelisti, Thierry Leininger, Pierre-François Loos, Nicolas Suaud, and JA Berger. Distributed Gaussian orbitals for the description of electrons in an external potential. *J. Mol. Model.*, 24(8):1–10, 2018. (Cited on pages 62 and 80.)

[93] Pierre-François Loos and Peter M. W. Gill. Ground state of two electrons on a sphere. *Phys. Rev. A*, 79:062517, Jun 2009. URL: `https://link.aps.org/doi/10.1103/PhysRevA.79.062517`, `doi:10.1103/PhysRevA.79.062517`. (Cited on pages 65 and 66.)

[94] D. M. Ceperley and B. J. Alder. Ground state of the electron gas by a stochastic method. *Phys. Rev. Lett.*, 45:566–569, Aug 1980. URL: `https://link.aps.org/doi/10.1103/PhysRevLett.45.566`, `doi:10.1103/PhysRevLett.45.566`. (Cited on page 71.)

[95] B. Tanatar and D. M. Ceperley. Ground state of the two-dimensional electron gas. *Phys. Rev. B*, 39:5005–5016, Mar 1989. URL: `https://link.aps.org/doi/10.1103/PhysRevB.39.5005`, `doi:10.1103/PhysRevB.39.5005`. (Cited on page 71.)

[96] F. Rapisarda and G. Senatore. Diffusion Monte Carlo study of electrons in two-dimensional layers. *Aus. J. Phys.*, 49:161, 1996. (Cited on page 71.)

[97] N. D. Drummond and R. J. Needs. Phase diagram of the low-density two-dimensional homogeneous electron gas. *Phys. Rev. Lett.*, 102(12):126402, Mar 2009. `doi:10.1103/PhysRevLett.102.126402`. (Cited on page 71.)

[98] S. Di Sabatino, J A Berger, L. Reining, and P. Romaniello. Reduced density-matrix functional theory: Correlation and spectroscopy. *J. Chem. Phys.*, 143(2):024108, 2015. `doi:10.1063/1.4926327`. (Cited on page 71.)

[99] Per-Olov Löwdin and Harrison Shull. Natural orbitals in the quantum theory of two-electron systems. *Phys. Rev.*, 101:1730–1739, Mar 1956. URL: `https://link.aps.org/doi/10.1103/PhysRev.101.1730`, `doi:10.1103/PhysRev.101.1730`. (Cited on page 72.)

[100] Jerzy Cioslowski and Katarzyna Pernal. The ground state of harmonium. *J. Chem. Phys.*, 113(19):8434–8443, 2000. `arXiv:https://doi.org/10.1063/1.1318767`, `doi:10.1063/1.1318767`. (Cited on page 73.)

[101] Jerzy Cioslowski. Solitonic natural orbitals. *J. Chem. Phys.*, 148(13):134120, 2018. `doi:10.1063/1.5023281`. (Cited on page 73.)

[102] Jerzy Cioslowski. Off-diagonal derivative discontinuities in the reduced density matrices of electronic systems. *J. Chem. Phys.*, 153(15):154108, 2020. `arXiv:https://doi.org/10.1063/5.0023955`, `doi:10.1063/5.0023955`. (Cited on page 73.)

[103] Estefania Alves, Gian Luigi Bendazzoli, Stefano Evangelisti, and J. Arjan Berger. Accurate ground-state energies of Wigner crystals from a simple real-space approach. *Phys. Rev. B*, 103:245125, Jun 2021. URL: `https://link.aps.org/doi/10.1103/PhysRevB.103.245125`, `doi:10.1103/PhysRevB.103.245125`. (Cited on page 75.)

[104] C A Sholl. The calculation of electrostatic energies of metals by plane-wise summation. *Proceedings of the Physical Society*, 92(2):434, oct 1967. URL: `https://dx.doi.org/10.1088/0370-1328/92/2/321`, `doi:10.1088/0370-1328/92/2/321`. (Cited on page 75.)

[105] R. W. Hasse and V. V. Avilov. Structure and Madelung energy of spherical Coulomb crystals. *Phys. Rev. A*, 44:4506–4515, Oct 1991. URL: `https://link.aps.org/doi/10.1103/PhysRevA.44.4506`, `doi:10.1103/PhysRevA.44.4506`. (Cited on page 75.)

[106] Richard L Hilderbrandt. Application of Newton-Raphson optimization techniques in molecular mechanics calculations. *Computers & Chemistry*, 1(3):179–186, 1977. (Cited on pages 79 and 110.)

[107] K. Aidas, C. Angeli, K. L. Bak, V. Bakken, R. Bast, L. Boman, O. Christiansen, R. Cimiraglia, S. Coriani, P. Dahle, E. K. Dalskov, U. Ekström, T. Enevoldsen, J. J. Eriksen, P. Ettenhuber, B. Fernández, L. Ferrighi, H. Fliegl, L. Frediani, K. Hald, A. Halkier, C. Hättig, H. Heiberg, T. Helgaker, A. C. Hennum, H. Hettema, E. Hjertenæs, S. Høst, I.-M. Høyvik, M. F. Iozzi, B. Jansik, H. J. Aa. Jensen, D. Jonsson, P. Jørgensen, J. Kauczor, S. Kirpekar, T. Kjærgaard, W. Klopper, S. Knecht, R. Kobayashi, H. Koch, J. Kongsted, A. Krapp, K. Kristensen, A. Ligabue, O. B. Lutnæs, J. I. Melo, K. V. Mikkelsen, R. H. Myhre, C. Neiss, C. B. Nielsen, P. Norman, J. Olsen, J. M. H. Olsen, A. Osted, M. J. Packer, F. Pawlowski, T. B. Pedersen, P. F. Provasi, S. Reine, Z. Rinkevicius, T. A. Ruden, K. Ruud, V. Rybkin, P. Salek, C. C. M. Samson, A. Sánchez de Merás, T. Saue, S. P. A. Sauer, B. Schimmelpfennig, K. Sneskov, A. H. Steindal, K. O. Sylvester-Hvid, P. R. Taylor, A. M. Teale, E. I. Tellgren, D. P. Tew, A. J. Thorvaldsen, L. Thøgersen, O. Vahtras, M. A. Watson, D. J. D. Wilson, M. Ziolkowski, and H. Ågren. The Dalton quantum chemistry program system. *WIREs Computational Molecular Science*, 4(3):269–284, 2014. URL: `https://wires.onlinelibrary.wiley.com/doi/abs/10.1002/wcms.1172`, `arXiv:https://wires.onlinelibrary.wiley.com/doi/pdf/10.1002/wcms.1172`, `doi:10.1002/wcms.1172`. (Cited on pages 80 and 111.)

[108] Felix Bloch. Bemerkung zur elektronentheorie des ferromagnetismus und der elektrischen leitfähigkeit. *Zeitschrift für Physik*, 57(7):545–555, 1929. (Cited on pages 80 and 111.)